



Global analysis of linear flame instability

Chuhan Wang

► To cite this version:

Chuhan Wang. Global analysis of linear flame instability. Fluid mechanics [physics.class-ph]. Institut Polytechnique de Paris, 2022. English. NNT : 2022IPPAX013 . tel-03681922

HAL Id: tel-03681922

<https://theses.hal.science/tel-03681922>

Submitted on 30 May 2022

HAL is a multi-disciplinary open access archive for the deposit and dissemination of scientific research documents, whether they are published or not. The documents may come from teaching and research institutions in France or abroad, or from public or private research centers.

L'archive ouverte pluridisciplinaire **HAL**, est destinée au dépôt et à la diffusion de documents scientifiques de niveau recherche, publiés ou non, émanant des établissements d'enseignement et de recherche français ou étrangers, des laboratoires publics ou privés.



Global linear analysis of flame instability

Thèse de doctorat de l'Institut Polytechnique de Paris
préparée à l'École polytechnique

École doctorale n°626 École doctorale de l'Institut Polytechnique de Paris (EDIPP)
Spécialité de doctorat : Mécanique des fluides et des solides, acoustique

Thèse présentée et soutenue à Palaiseau, le 14 février 2022, par

CHUHAN WANG

Composition du Jury :

Denis Sipp Directeur de recherche, ONERA, DAAA	Président
Lutz Lesshafft Directeur de recherche, Ecole Polytechnique-CNRS, LadHyX	Directeur de thèse
Taraneh Sayadi Chargée de recherche, Sorbonne Université, DALEMBERT	Rapporteuse
Matthew Juniper Professor, University of Cambridge, Engineering Department	Rapporteur
Laurent Gicquel Senior researcher, CERFACS, Computational Fluid Dynamics Team	Examineur
Franck Nicoud Professeur, Université de Montpellier, IMAG	Examineur
Tim Lieuwen Professor, Georgia Institute of Technology, Aerospace Engineering Department	Examineur

Abstract (English)

The thesis aims to apply recent developments of methodology from the field of linear instability theory to the study of flame instability. The flame instability here refers to the unsteady oscillations in the reacting flow field. Eigenmode analysis for the description of self-sustained oscillations, and input-output analysis for the characterization of amplifier behaviour is implemented in a global framework, without parallel-flow assumption. The governing equations of reacting flow are linearized and resolved in the entire computational domain, including the linearized chemical reaction schemes. In this framework, the interplay between flow dynamics, chemical reaction and acoustics can be inherently accounted for and investigated in full detail. The thesis focuses on the linear dynamics of premixed laminar flames, mainly a slot flame that acts as an amplifier, and a bluff-body stabilised flame that acts as an oscillator.

The response to forcing of the slot flame with a two-step reaction scheme for methane combustion is investigated in the linear regime. The flame transfer function is computed from the linear model, in excellent agreement with reference nonlinear calculations. The energy gain between externally applied forcing and the global heat release response is computed, and peaks in the gain are related to intrinsic thermoacoustic modes. The receptivity of the flame to arbitrary flow forcing is characterised by the resulting amplitude of global heat release fluctuations. Resolvent analysis is used to identify optimal forcing structures and their associated flame response, leading to a discussion of the dominant mechanisms for the amplification of flow perturbations, which trigger flame oscillations. These seem to involve a resonance with intrinsic thermoacoustic instability modes.

Global linear stability of a laminar premixed flame anchored on a bluff body is investigated via modal analysis. Both nonlinear timestepping and stability analysis demonstrate that the reacting flow is significantly stabilized with respect to the non-reacting vortex shedding case, but the flame is again destabilised if the bluff body is heated more. By detailed decomposition of eigenmodes in the steady-state flow, the active flow region that drives instability is identified within the region where the base flow vorticity is largest in the wake shear region. The momentum equation is found to dominantly contribute to the temporal growth among all the conservation equations. These results quantitatively show that the global flame dynamics is controlled by hydrodynamic instability in the wake shear. The visible oscillations observed in the downstream flame front turn out to be passive. Mean flow analysis of an oscillating flame in the limit cycle accurately captures the shedding frequency.

Towards understanding the role of large-scale coherent structures in the instability of turbulent flames, a fundamental study about the effect of streaks on the instability of non-reacting incompressible jets is included. The presence of elongated streaks of high and low streamwise velocity in the shear layer of circular jets breaks the axisymmetry of their steady-state solution. If the streaks are considered to be part of the base flow, for the purpose of linear instability analysis, the instability eigenmodes are thus affected by

their presence. The resulting changes of growth rate and spatial shapes of eigenmodes, related to the shear instability in jets, are investigated for parallel base flows. Optimal streamwise vortices (“rolls”) with prescribed azimuthal periodicity are computed, such that the transient temporal growth of the streaks that they produce is maximal. Sinuous rolls and streaks are found to have a stabilising effect on the Kelvin-Helmholtz instability, whereas the varicose rolls and streaks have a destabilising effect. Absolute instability is not found to occur. The results show that the effects of rolls and streaks need to be taken into account for more precise modelling of jet instability, and their presence in turbulent flames is a potential orientation for future studies.

Abstract (Français)

Cette thèse vise à appliquer les développements récents de la méthodologie du domaine de la théorie de l'instabilité linéaire à l'étude de l'instabilité de la flamme. L'instabilité de la flamme ici dénote les oscillations dans un écoulement réactif. L'analyse des modes propres pour la description des oscillations auto-entretenues et l'analyse entrée-sortie pour la caractérisation du comportement des amplificateurs sont mises en œuvre dans un cadre global, sans évoquer à l'hypothèse d'écoulement parallèle. Les équations décrivant l'écoulement réactif sont linéarisées et résolues dans l'ensemble du domaine de calcul, y compris les schémas de réaction chimique linéarisés. Dans ce cadre, l'interaction entre la dynamique de l'écoulement, la réaction chimique et l'acoustique peut être intrinsèquement prise en compte et étudiée en détail. Cette thèse est centrée sur la dynamique linéaire des flammes laminaires prémélangées, comprenant principalement une flamme à fente qui se comporte en amplificateur, et une flamme stabilisée à corps bluff qui se comporte en oscillateur.

La réponse à un forçage de la flamme à fente avec un schéma de réaction en deux étapes pour la combustion du méthane est étudiée dans le régime linéaire. La fonction de transfert de flamme est calculée à partir du modèle linéaire, en excellent accord avec les calculs non linéaires de référence. Le gain d'énergie entre le forçage appliqué de l'extérieur et la réponse globale de dégagement de chaleur est calculé, et les pics de gain sont liés aux modes thermoacoustiques intrinsèques. La réceptivité de la flamme à un forçage arbitraire de l'écoulement est caractérisée par l'amplitude résultante des fluctuations globales de dégagement de chaleur. L'analyse de la résolvante est utilisée pour identifier les structures de forçage optimal et leur réponse de flamme associée, conduisant à une discussion des mécanismes dominants pour l'amplification des perturbations d'écoulement, qui déclenchent des oscillations de flamme. Ceux-ci semblent impliquer une résonance avec des modes d'instabilité thermoacoustique intrinsèques.

La stabilité linéaire globale d'une flamme laminaire prémélangée ancrée sur un cylindre est étudiée via une analyse modale. L'avancement temporel non linéaire et l'analyse de stabilité démontrent que l'écoulement réactif est fortement stabilisé par rapport au cas non réactif, mais la flamme est à nouveau déstabilisée si le cylindre est davantage chauffé. Par une décomposition détaillée des modes propres dans l'écoulement en régime stationnaire, la région active de l'écoulement qui entraîne l'instabilité est identifiée dans la région où la vorticit  de l'écoulement de base atteint son maximum, dans le sillage proche. L'équation de quantité de mouvement s'avère contribuer de manière dominante à la croissance temporelle parmi toutes les équations de conservation. Ces résultats montrent quantitativement que la dynamique globale de la flamme est ici contrôlée par l'instabilité hydrodynamique dans le cisaillement du sillage. Les oscillations visibles observées dans le front de flamme en aval s'avèrent être passives. L'analyse du champ moyen d'une flamme oscillante dans le cycle limite capture avec précision la fréquence d'oscillation, ce qui peut être considéré comme un cas de référence pour l'analyse modale sur l'écoulement moyen réactif avec le schéma de chimie linéarisé.

Afin de comprendre le rôle des structures cohérentes à grande échelle dans l'instabilité des flammes turbulentes, une étude fondamentale sur l'effet des stries sur l'instabilité des jets incompressibles non réactifs est proposée. La présence de stries allongées dans le sens de l'écoulement moyen, et localisées dans la couche de cisaillement des jets circulaires, brise l'axisymétrie de leur solution à l'état d'équilibre. Si les stries sont considérées comme faisant partie de l'écoulement de base, aux fins de l'analyse d'instabilité linéaire, les modes propres d'instabilité sont donc affectés par leur présence. Les changements résultants du taux de croissance et des formes spatiales des modes propres, liés à l'instabilité de cisaillement dans les jets, sont étudiés pour des écoulements de base parallèles. Des tourbillons optimaux dans le sens de l'écoulement ("rouleaux") avec une périodicité azimutale prescrite sont calculés, de telle sorte que la croissance temporelle transitoire des stries qu'ils produisent soit maximale. La présence de stries d'amplitude finie nécessite la formulation d'un problème aux valeurs propres dans un plan bidimensionnel. Les rouleaux et les stries sinueuses ont un effet stabilisant sur l'instabilité de Kelvin-Helmholtz, tandis que les rouleaux et les stries variqueuses ont un effet déstabilisant. Il n'y a pas d'instabilité absolue. Les résultats montrent que les effets des rouleaux et des stries doivent être pris en compte pour une modélisation plus précise de l'instabilité du jet. Leur présence dans les flammes turbulentes est une orientation potentielle pour de futures études.

Acknowledgements

Jusqu'à la fin de cette thèse, j'ai passé cinq ans en France dont deux à Lyon et trois à Paris. En premier lieu, je tiens à remercier ce pays magnifique et ses citoyens chaleureux de m'avoir accueilli pour mes études et mes recherches.

Foremost, I would like to express my sincere gratitude to my advisor Lutz Lesshafft. From quite a long time, I am convinced that the main objective of a thesis is to cultivate an independant researcher, and Lutz demonstrates by his own how to achieve this goal. I clearly remember our first conversation in the summer of 2017 when Lutz told me his linear analysis methods could *open a door* to flame instability studies. I am very lucky to be assigned to such a project during my thesis. Lutz dedicated a great amount of time in his advisor duty, giving his constructive ideas and critical assessments consecutively, represented by the email response from him very often received in the midnight and during the weekend. His pursuing of highest qualities in every work was very appreciated, charaterized by a considerable number of iterations before submitting a manuscript or a conference video. Lutz also made significant efforts in helping my career development, including building networks with a large variety of collaborators worldwide.

My sincere thanks goes to all those collaborators. I am highly indebted to Kilian Oberleithner and Thomas Ludwig Kaiser at TU Berlin for their huge contribution to the slot flame project. Kilian held keen interests at every stage of my research, giving his inspiring suggestions especially from the aspects of both hydrodynamic and combustion research. I am also grateful to Wolfgang Polifke, Max Meindl and Grégoire Varillon at TU Munich for their help in the code development and their involvement in the different projects. It is very pleasant to read those excellent papers on the linearized reactive flow (LRF) solver from Wolfgang and Max that really inspired this thesis. I would like to thank Peter Jordan and André Cavalieri for their contribution to the jet streak paper, and also to Peter for the organization of that excellent Euromech conference. Special thanks and good luck for my friends in the LadHyX office, Quentin, Can and Chris, for their efforts in various code development projects.

I would like to express my sincere gratitude to the two reviewers Taraneh Sayadi and Matthew Juniper for taking time to go through the manuscript. I would also like to give my best gratitude to the other members of my jury, including Laurent Gicquel and Franck Nicoud who have already given their insightful remarks during my midterm defense, and also to Denis Sipp and Tim Lieuwen. Special thanks to Laurent Gicquel who accepted my participation in the training at CERFACS, and also for answering my technical questions on AVBP.

I want to thank the researchers and staff in LadHyX led by Emmanuel for the comfortable and convenient working environment, and all the travel and technical supports. I would like to express my sincere respect and gratitude to Patrick for all his interests and encouragements during these three years. As I told Patrick, all what I have done throughout the thesis is simply extending the theories that he founded to a more complex flow

configuration. Special thanks go to Tom for sharing the office with me during 2.5 years, to Francesco and Benjamin for animating the students' network.

It is my privilege to thank my wife Mingshan, and my family for their long-distance but always long-time supporting, especially during this Covid crisis that makes the international travel very difficult. Thanks for Chengran, Zhihao and Yang, my friends in Paris for all the discussions and supports.

Contents

1	Introduction	1
1.1	Linear analysis	2
1.2	Flame instability	4
1.2.1	Thermoacoustic instability	4
1.2.2	Low-order network models	5
1.2.3	Flame transfer function	5
1.2.4	Intrinsic thermoacoustic instability	6
1.3	Linear analysis of flame instability	6
1.3.1	Analysis with linearized chemistry in the premixed flames	7
1.3.2	Purely hydrodynamic modes in flames	9
1.3.3	Global linear analysis in diffusion flames	10
1.4	Objectives	11
1.5	Thesis outline	11
2	Resolvent analysis of a slot flame	13
2.1	Strategies of forcing a flame	14
2.2	Test cases	15
2.2.1	Heated slit	16
2.2.2	Flame with one-step chemical scheme	16
2.3	Paper: Linear instability of a premixed slot flame	19
2.3.1	Introduction	19
2.3.2	Nonlinear simulation of a steady slot flame	22
2.3.3	Methods	23
2.3.4	The flame transfer function	26
2.3.5	Receptivity of global heat release rate fluctuations to arbitrary forcing	30
2.3.6	Resolvent analysis	31
2.3.7	Conclusions	36
2.4	Further discussions	39
2.4.1	Projection on the basis of resolvent modes	39
2.4.2	Sensitivity to numerical domain length	39
2.4.3	Choice of response norms	41
2.4.4	Eigenmodes of the flame	41
2.4.5	Orr-mechanism	41
2.4.6	Impact of flame attachment	42
3	Modal analysis of a bluff body stabilised flame	43
3.1	Introduction	44
3.2	Methods	47
3.2.1	Nonlinear governing equations	47

3.2.2	Calculation of base flow and mean flow	48
3.2.3	Global linear analysis	49
3.3	Non-reacting flow	49
3.4	Reacting flow: studies on the steady base state	51
3.4.1	Global modes in base flow	51
3.4.2	Wavemaker analysis	53
3.4.3	Influence of reaction on the base flow	55
3.5	Reacting flow: mean flow analysis	56
3.6	Conclusions	57
4	Modal analysis of a V-shaped flame	63
4.1	Motivation	64
4.2	Preliminary results	64
4.2.1	Case $Re = 200$	64
4.2.2	Case $Re = 5000$	67
4.3	Future plan	68
5	Towards coherent structures in jet flames: streaks in non-reacting jets	71
5.1	Context	72
5.1.1	Streaks in boundary-layer flames	72
5.1.2	Streaks as optimal perturbations in shear flows	73
5.1.3	Linear instability mechanisms in jets	74
5.2	Paper: The effect of streaks on the instability of jets	76
5.2.1	Introduction	76
5.2.2	Evolution of rolls and streaks in a parallel jet	77
5.2.3	Linear stability analysis	80
5.2.4	Conclusions	87
5.3	Further discussions	89
6	Conclusions and perspectives	93
6.1	Summary of the main contributions	94
6.2	Perspectives	96
6.2.1	Closed-loop control of the flame instability based on linearized governing equations	96
6.2.2	Role of chemistry model in linear analysis of turbulent flames	97
6.2.3	Impact of conjugate solid-fluid heat transfer on the flame stability	98
6.2.4	Nonlinear nonmodal stability analysis for flames	99
A	Linear analysis methodologies	101
A.1	Modal analysis	102
A.1.1	Direct and adjoint modes	102
A.1.2	Wavemaker analysis	103
A.1.3	Sensitivity to base flow modifications	104
A.2	Nonmodal analysis	105
A.2.1	Temporal approach: transient growth	105
A.2.2	Frequency approach: resolvent analysis	106

B Numerical methods	109
B.1 Description of different codes developed	110
B.2 Implementation of variational formulations in FENiCS	110
B.3 Newton solver	111
B.4 Timestepper	113
B.5 Linear analysis and eigenvalue solvers	113

CHAPTER 1

Introduction

Contents

1.1	Linear analysis	2
1.2	Flame instability	4
1.2.1	Thermoacoustic instability	4
1.2.2	Low-order network models	5
1.2.3	Flame transfer function	5
1.2.4	Intrinsic thermoacoustic instability	6
1.3	Linear analysis of flame instability	6
1.3.1	Analysis with linearized chemistry in the premixed flames	7
1.3.2	Purely hydrodynamic modes in flames	9
1.3.3	Global linear analysis in diffusion flames	10
1.4	Objectives	11
1.5	Thesis outline	11

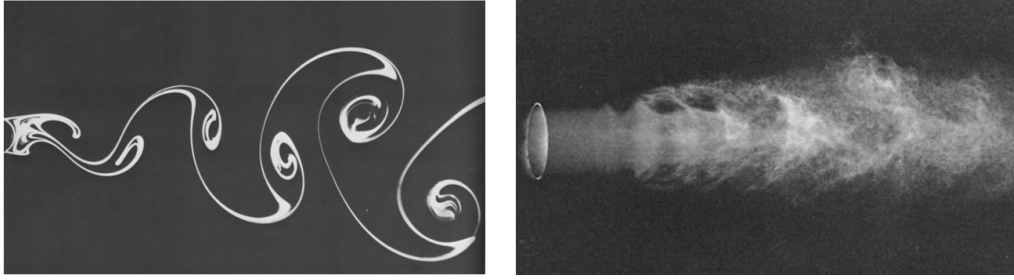


Figure 1.1: Examples of the oscillator- and amplifier-type flow. Left: Bénard-Kármán vortex street in a circular cylinder wake at Reynolds number $Re_D = 140$ (photograph by Sadatoshi Taneda taken from van Dyke 1989); right: response of an incompressible circular jet at Reynolds number $Re_D = 1.95 \times 10^4$ to an acoustic forcing of Strouhal number $St = 0.3$ (figure taken from Crow and Champagne 1971).

1.1 Linear analysis

Linear analysis provides standard mathematical tools applied to a large variety of flows. It allows to extract physical mechanisms that drive the unsteadiness. It can also be used to predict the flow behaviors and suggest strategies for flow control. In linear stability analysis, we aim at answering the question if an infinitesimal perturbation around the mean state grows or decays with time. Here the mean state refers to the time-averaged *mean flow*. A steady flow state, which does not need to be time-averaged, is called a *base flow*. The basic idea of linear analysis is to decompose an unsteady flow into a mean field and fluctuations around that mean. Those fluctuations have zero mean by definition. The dynamics of small-amplitude fluctuations are controlled by the linearized governing equations, of which the left-hand side is the time derivative of flow fluctuations, and the right-hand side is the Jacobian matrix of the nonlinear flow equations. By calculating the eigenmodes of the Jacobian matrix, we consider a flow as being unstable if it has at least one eigenvalue whose real part, the temporal growth rate, is positive. The approach described above is called *modal analysis*.

Modal analysis can be categorized, according to the hypothesis on the mean flow and fluctuations, into local analysis and global analysis. In *local* analysis, the mean flow is assumed to be parallel, in the sense that the spatial evolution of perturbations is much faster than that of the mean flow. That allows a detailed discussion of the flow instability at a streamwise location, classified into three categories: stable, convectively unstable and absolutely unstable (Huerre and Monkewitz 1990).

In *global* analysis, the mean flow is non-parallel, and the global mode is calculated in a two- or three-dimensional flow domain. The global instability is determined by the largest temporal growth rate among that of all the eigenmodes. If the largest temporal growth rate is positive, the flow is globally unstable and displays self-excited behavior. Such a flow can be described as an *oscillator*. The most well-known oscillator is certainly the wake instability of a circular cylinder, which sheds vortex streets at a supercritical Reynolds number, as shown in figure 1.1. In this case, the instability depends on the endogenous dynamics of the flow system itself, which has been well explored through global modal analysis (Noack and Eckelmann 1994; Theofilis 2003; Barkley 2006).

If the largest temporal growth rate is negative, the flow is globally stable: all perturbations will decay at long times, so that the flow returns to the equilibrium state within an infinite time horizon. However, the perturbations may experience short-time transient growth, so a finite time horizon is required to be introduced for a more general analysis. Such analysis of the transient growth is called *nonmodal analysis* (Schmid and Henningson

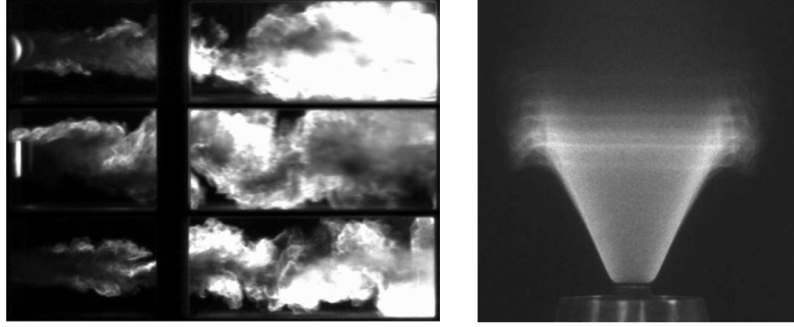


Figure 1.2: Examples of the oscillator- and amplifier-type flame. Left: bluff body stabilized flames at Reynolds number $Re_D = 4 \times 10^4$ (figure taken from Kiel et al. 2007). From top to bottom, the flame is anchored on a cylinder, a square and a V-gutter; right: V-shaped flame anchored on an annular chamber and acoustically forced (figure taken from Schuller 2003).

2001). External perturbations acting on a globally stable flow can experience short-time growth, for example, in the jet forced by acoustic waves as shown in figure 1.1. Small perturbations at the inlet induced by acoustic excitations experience growth as they are convected downstream, leading to a large flow response. The perturbations are amplified through the flow, so such a flow system is called an *amplifier*. The amplification of harmonic external perturbations is often investigated by means of *resolvent analysis*; this formalism can be applied to laminar as well as turbulent flow regimes, as demonstrated for jets (Garnaud et al. 2013b; Beneddine et al. 2016; Lesshafft et al. 2019), backward-facing step flow (Barbagallo et al. 2012) and channel flow (McKeon and Sharma 2010; Morra et al. 2019), among other configurations. In the resolvent framework, optimal forcing and associated flow response structures are identified in the frequency domain.

In this thesis, the phrase “global linear analysis” refers to both *modal* and *nonmodal* analysis of nonparallel flow fields. In fact, linear analysis is much more powerful than just telling if a flow is stable or unstable. It allows to examine the detailed physics of flow dynamics, for example, the optimal forcing identified by the resolvent analysis indicates the most efficient manner and region to force a flow with respect to a given norm. Other typical questions that can be answered by linear analysis include where the most stability-sensitive areas of the flow (Giannetti and Luchini 2007; Marquet et al. 2008) are located, which terms in the governing equations contributes the most to the stability (Marquet and Lesshafft 2015; Paladini et al. 2019), and how the stability changes with respect to a certain control parameter (Magri 2019; Skene and Schmid 2019). The appendix A “linear analysis methodologies” is dedicated to the presentation of the mathematical formulations to answer those questions.

While the flow has been characterized as oscillator and amplifier according to the origin of their instability behaviour, we wonder if we can extend those notions to flames, whose instability is one of the key subjects in combustion research (Poinsot 2017; Lieuwen 2021). Flame configurations of oscillator and amplifier highly related to their non-reacting counterparts can be found in figure 1.2: fuel air is ignited and stabilized on the cylinder and other bluff bodies, displaying self-excited vortex-street-like flame oscillations; a laminar V-shaped flame responds to the acoustic forcing, showing instantaneous unsteady motions of the flame front. As global linear analysis has already been demonstrated to be capable to examine the non-reacting flow dynamics, a straightforward idea is to apply it to the study of reacting flow, the flame dynamics.

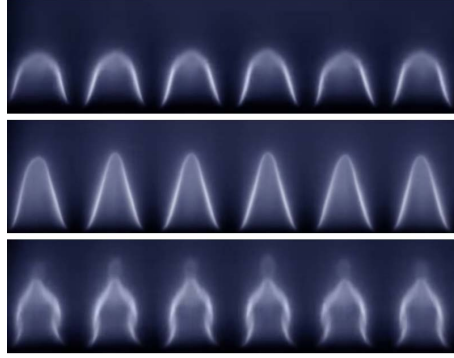


Figure 1.3: Snapshots of premixed laminar slot flames responding to a music. Video “Waka Waka Flame HD” uploaded on Youtube by Mejia 2014.

1.2 Flame instability

1.2.1 Thermoacoustic instability

Flames respond to acoustic waves, and flames generate acoustic waves. Unstable behavior of premixed flames anchored on slots and dancing with music from a loudspeaker is shown in figure 1.3. If we send sound waves to a flame from underneath through a loudspeaker, the flame response can be visualized by the strong oscillation of the flame front. The perturbed flame front generates heat release, resulting in new acoustic waves traveling away from the flame. When the flame is inside any enclosed volume such as a combustor, the acoustic waves reach the boundary and can be reflected backwards to the flame, leading to a new perturbation of the flame front. Thus, we have a two-way coupling of flame and acoustics. This coupling is a positive feedback loop that may grow in each cycle, leading to successively increasing amplitudes of flame oscillations, which is the standard description of the thermoacoustic instability.

The oscillations of the flame are visibly strong with respect to its size, already in this laminar flame susceptible to a music. In the industrial design of combustion systems, the flame instability is a much more serious issue. During the launch of space rockets, for example, the rocket rises vertically, and its tail flame is visibly stable. If the tail flame of the rocket is not stable, the thrust generated by the tail end of the rocket may make the rocket fly in all directions. Also, in an internal combustion engine, for instance, violent oscillations of the flame in the combustion chamber may not only cause the entire combustion chamber to oscillate, but also cause the material in the combustion chamber to undergo abrupt temperature changes, which may eventually lead to serious accidents. Thus, thermoacoustic plays a key role in the design of gas turbines and engines, and thousands of real experiments have to be carried out to make sure the system can operate without suffering from thermoacoustic instability. Recent policies to reduce carbon emissions have promoted the research on the combustion of clean energy such as hydrogen and ammonia, but the use of those clean energy seems to increase the challenges in the aspect of instability (Sánchez and Williams 2014; Kobayashi et al. 2019). The modelling and calculations of flame instability through Computational Fluid Dynamics (CFD) could give a first insight for a parametrization of the real experiments.

Using CFD tools, especially Large-Eddy Simulation (LES), simulations of the whole combustion chamber have been performed in laboratory-scale and industry-scale combustors (*e.g.*, Gicquel et al. 2012). One of the main problems that makes those calculations very expensive is the range of time and length scales, for example, the chemical reaction

is much faster than the flow time scales (Poinsot and Veynante 2005). Thermoacoustic instability usually takes place at low frequencies of a few hundreds of Hertz, giving rise to wavelengths of several meters or more. At the same time, the flame front wrinkling often has length scales that can be easily less than a millimeter. Although a lot of progress has been made in high-fidelity computational tools and methods (Gourdain et al. 2014; Van Oijen et al. 2016; Lourier et al. 2017), it can be understood that resolving all the length and time scales to predict the real combustors is still very challenging.

1.2.2 Low-order network models

Another widely-used method to study the flame instability is to use low-order network models. These models characterize the combustion systems as the conjunction of elements, such as the plenum, the premixed duct, and the combustion chamber. The acoustic waves are typically modelled as being both linear and low dimensional. The linearity is justified by the fact that in most of cases, the acoustic pressure amplitude in limit cycles is below 10% of the mean pressure (Paschereit et al. 2002). The acoustic waves travel in both directions in a connected network, and the connection between different elements can be modelled by the conservations laws. The interaction between the flame and the acoustics is often modelled by a semi-empirical approach: the acoustic field produced by the flame can be modelled according to the linearized Rankine–Hugoniot jump conditions (Chu 1953), and the heat release produced by the acoustic waves forcing the flame is characterized by the flame transfer function (FTF) in the linear regime, or the flame describing function (FDF) in the weakly nonlinear regime (Han et al. 2015). Network models have been used to explain a large range of fundamental problems in thermoacoustic instability (Juniper and Sujith 2018; Sogaro et al. 2019; Orchini et al. 2020), yet the treatment of the model is too simplified for the acoustics, because the mean flow effect, the specific geometry and boundary conditions of the system cannot be all taken into account.

1.2.3 Flame transfer function

A key question in the modeling of thermoacoustic instability is how the flame responds to the acoustic waves. The heat release is usually taken as the scalar to model the global response, because the heat release takes place all along the flame front. In order to measure the unsteady flame response to an upstream forcing, the flame transfer function at an angular velocity ω is defined as

$$F(\omega) = \frac{\bar{u}_{\text{ref}} \dot{\bar{\Omega}}'_T}{\dot{\bar{\Omega}}_T u'_{\text{ref}}}, \quad (1.1)$$

where $\dot{\bar{\Omega}}_T$ is the global heat release rate and u_{ref} is the velocity at a reference upstream position, for example, at the upstream inlet. The mean flow component is represented with a bar and the fluctuation component is represented with a prime. In other words, the FTF models the global heat release fluctuation as a function of an upstream velocity perturbation. This relation is normalized by their meanflow counterpart. The analytical solutions of the FTF can be obtained in some simple configurations through the G-equations that describe the flame front movement (Schuller 2003). For more practical cases, the FTF can be obtained empirically via system identification methods based on time-series of forcing and response data, from both experiments and numerical simulations (Polifke 2014). Classically, we force a flame with a harmonic signal and we measure the resulting global heat release. Such a strategy is data-driven, which may be regarded as a *black-box* method.

However, to model a linear system, there is also the *white-box* method that is completely based on the physics. We have the Navier-Stokes equations to describe the flow dynamics,

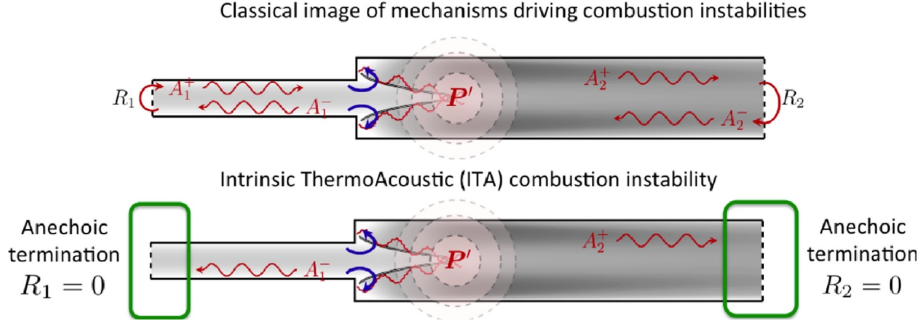


Figure 1.4: Classical and intrinsic thermoacoustic (ITA) mode (figure taken from Poinso 2017).

so it is enough to take the Jacobian of the nonlinear flow equations to establish the linear system. Such a *white-box* method based on the linearized governing equations around the mean state is the approach that we apply throughout this thesis to understand the flame dynamics, including calculating the FTF, and of course, using standard stability analysis tools on that Jacobian matrix, to study the flame instability.

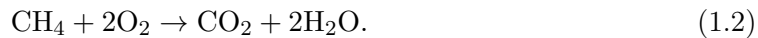
1.2.4 Intrinsic thermoacoustic instability

It is expected that the thermoacoustic mode can be captured by calculating the global eigenmodes of the flame via the linearized flow equations. However, capturing the classical thermoacoustic mode may be too ambitious, because we would run into the same problem of very different length scales in the combustion chamber, as it is the case in CFD. Instead, the so-called intrinsic thermoacoustic (ITA) instability represents a very interesting scenario to be considered (Hoeijmakers et al. 2014; Emmert et al. 2015). The acoustic waves generated from the flame tip can travel *upstream* to the injector exit, where they modulate the velocity again convected downstream to the flame, as illustrated in figure 1.4 (Poinso 2017). This closes a positive feedback that happens only in the upstream region of a flame. The ITA modes can happen in an anechoic environment, independent of acoustic chamber mode. Direct numerical simulation (DNS) has been carried out to study the ITA instability (Courtine et al. 2015). The computational domain applied is not required to include the whole combustion chamber, and the cost for linear analysis is relatively affordable.

The frequency of ITA modes can be predicted from the phase of FTF by the π criterion, which is deduced from a network model: the ITA modes may occur at the frequencies where the phase of FTF is equal to an odd multiple of π (Hoeijmakers et al. 2014). That criterion is complemented by a critical gain value at those frequencies (Courtine et al. 2015). We will revisit the π criterion in the configuration of an amplifier-type flame.

1.3 Linear analysis of flame instability

Global linear analysis has been used both in premixed flames and diffusion flames. An important challenge therein is the linearization of the chemical reaction scheme, which is exponential and dependent on many variables in the mean flow. Consider a simple one-step methane-air reaction scheme with four species



Here, “one-step” refers to a single reaction. A chemical progress rate Q has to be modelled, which is proportional to the chemical heat release in the conservation equation of energy, and to the consumption and production rate of species in the conservation equation of

species mass fraction. The chemical progress rate is commonly modelled by the Arrhenius law. For the reaction in (1.2), it can be written in the form

$$\mathcal{Q} = A\rho^{a+b} \frac{Y_{\text{O}_2}^a Y_{\text{CH}_4}^b}{W_{\text{O}_2}^a W_{\text{CH}_4}^b} \exp\left(-\frac{T_a}{T}\right) \quad (1.3)$$

where the flow variables ρ , T and Y_k are density, temperature and mass fraction of species k , respectively. The constants A , T_a , a and b are model coefficients. The constant T_a is called the activation temperature, that determines the onset temperature of reaction. If we linearize the chemical progress rate \mathcal{Q} around a mean flow, we obtain its fluctuation

$$\mathcal{Q}' = \bar{\mathcal{Q}} \left((a+b) \frac{\rho'}{\bar{\rho}} + \frac{T_a T'}{\bar{T}} + a \frac{Y'_{\text{O}_2}}{\bar{Y}_{\text{O}_2}} + b \frac{Y'_{\text{CH}_4}}{\bar{Y}_{\text{CH}_4}} \right). \quad (1.4)$$

The involvement of a linearized chemical scheme in a similar form as (1.4) is the distinguished difficulty with respect to linear analysis in the non-reacting flow. The fluctuation of progress rate \mathcal{Q}' is often concentrated in the flame front where the mean flow variables have very large gradients, so the flame front has to be resolved with high resolution. Also, the reaction of (1.3) already takes the simplest form. High-fidelity calculations of flame dynamics use chemical schemes with many more reactions and species, for instance, a detailed chemical scheme to model natural gas combustion can be comprised of 325 reactions and 53 species, including NO formation and reburn chemistry (CERFACS 2017).

Most of previous linear analysis of flames do not include chemistry in the linear governing equations or use one-step chemistry. Recently Meindl et al. 2021 linearized a two-step methane-air reaction scheme including 6 species, in which one of the reactions is reversible. The calculation results are quantitatively in agreement with reference results. In this thesis, both one-step and two-step chemical schemes are linearized and implemented in the code that we use.

In steady premixed laminar flames, the chemical reactions are numerically feasible to be linearized around the steady base flow. A very detailed review of work in such a configuration is given in §1.3.1. Linear analysis without chemical scheme in flames are given in §1.3.2. Studies on diffusion flames are briefly given in §1.3.3.

1.3.1 Analysis with linearized chemistry in the premixed flames

Studying the dynamics of the premixed laminar flame via global linear analysis has been carried out mainly from two series of research.

The first series of work is from Polifke and co-workers, of which the objective is to introduce a new approach that can accurately calculate the FTFs and thermoacoustic modes. The thermoacoustic network-model (TNM), the linearized Navier-Stokes equations (LNSE) and the linearized reactive flow equations (LRF) are used to calculate the FTFs and the global eigenmodes of a premixed slot flame (Avdonin et al. 2019). The LNSE uses the incompressible Navier-Stokes equations without taking into account any chemical reaction. It takes only the velocity as inputs from the steady base state. The LRF contains all the linearized equations for the simulation of a reacting flow, normally including the conservation equations of momentum, mass, energy and mass fraction of species. The chemical reactions, usually modelled through the Arrhenius law, are involved in the conservation equation of energy as the chemical heat release, and in the species equation as the reaction progress rate. The FTF of slot flames with adiabatic and isothermal wall conditions were calculated via the LRF solver, in very good agreement with the CFD results. The global modes at the frequency where the ITA modes are expected to appear were calculated using four models: TNM, LNSE, LRF and a hybrid model combining LNSE with the FTF

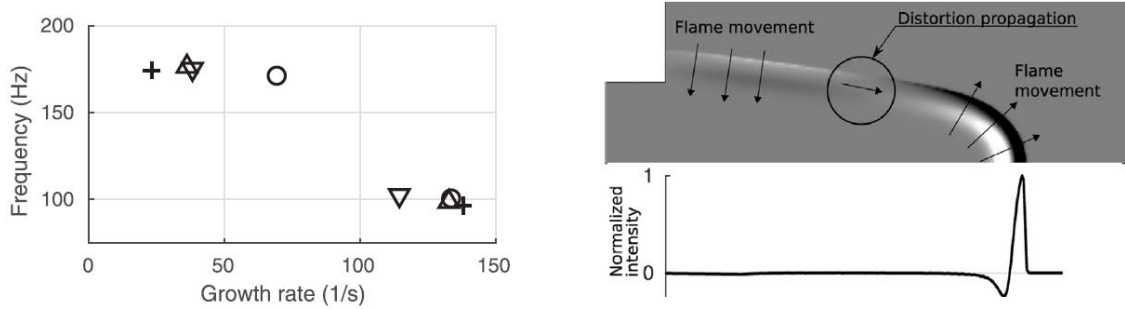


Figure 1.5: Unstable eigenmodes identified in a slot flame (figures taken from Avdonin et al. 2019). Left: eigenspectra of the adiabatic flame (≈ 170 Hz) and the isothermal flame (≈ 100 Hz) calculated via LRF (+), hybrid LNSE+FTF (Δ), LNSE (∇) and TNM (\circ). Right: real part of the heat release.

(LNSE+FTF) obtained by the LRF. The eigenvalues are presented on the left of figure 1.5 (Avdonin et al. 2019). The temporal growth rates of eigenvalues obtained by four methods are very different especially for the adiabatic flame configuration. The heat release rate fluctuations are shown on the right of figure 1.5. With the LRF approach, the flow-flame was locally resolved, suggestive of a distortion of the flame front induced at the flame root. The entropy wave generated by acoustically forced premixed slot flames, including a freely propagating 1D flame and a 2D slot flame was calculated, via the LNSE+FTF and LRF approach (Meindl et al. 2021). For the LRF approach, a two-step chemistry model was linearized. The LNSE+FTF generates spurious entropy waves where the FTF is taken as a lumped element that only outputs a global heat release fluctuation rate. In contrast, the results of FTF and entropy wave generation obtained through the linearized solver are in quantitative agreement with CFD results. The LRF solver was also used to study the interaction between inertial waves and flames (Albayrak et al. 2018). Inertial waves have non-zero axial and radial components, which bring the flame out of kinematic balance and thereby cause changes in flame shape and heat release. The flame front was found to be modulated mainly from axial and radial velocity fluctuations associated with the inertial waves.

The second series is from Blanchard 2015 who investigated the input-output mechanism of an M-shaped flame. The objective of their work is to develop new methods to calculate and understand the response of an M-shaped flame to small flow oscillations. The FTF calculated through the linear solver is qualitatively validated with respect to the experiment, showing a peak at the same frequency. The flame response to an acoustic forcing as a volume source term was then calculated. The phase speeds of heat release and vorticity fluctuations were found to be strongly correlated, as shown in figure 1.6 (Blanchard et al. 2015). The optimal means of noise generation by the flame front was then studied. In detail, a physics-based norm for compressible flows (Chu 1965) that includes all the flow variables was used to define the energy norm of forcing. The forcing region was chosen inside the inflow channel, because the authors aimed at understanding how the perturbations convected from the injector affects the acoustic response of the flame. The pressure fluctuation was chosen as the norm for optimization either in the full field or along a spherical surface. The optimal forcing and the associated flame response structures are shown in figure 1.7 (Blanchard 2015). The authors indicated that the forcing structures are suggestive of the Orr mechanism in boundary layers (Monokrousos et al. 2010). The flame response is characterized by strong oscillations at the flame tip. Such a linear analysis was extended to the swirling M-shaped flame by Skene and Schmid 2019. The authors studied the influence of the base-flow swirl on the optimal frequency response. The decrease of

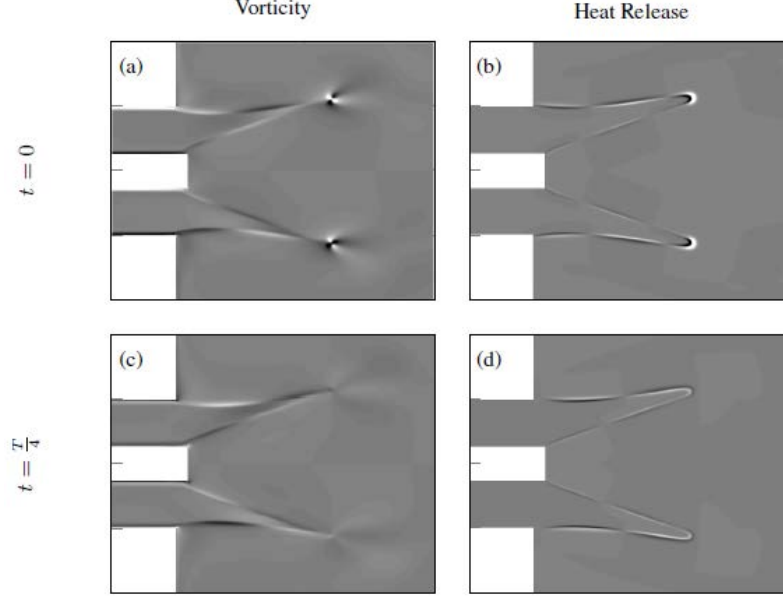


Figure 1.6: Response of vorticity and heat release fluctuations of the M-flame to a linear harmonic volume forcing. The flame response at two different instants $t = 0$ and $t = \frac{T}{4}$ of a periodic cycle T is shown (figure taken from Blanchard et al. 2015).

response gain due to swirl can be qualitatively captured by an adjoint-based sensitivity analysis at low azimuthal wavenumbers. That series of work on the M-shaped flame by Blanchard 2015 is an excellent example study of amplifier-type flames with the linearized governing equations, which inspires our present study.

1.3.2 Purely hydrodynamic modes in flames

Another category of analysis, mainly employed for turbulent flames, does not involve chemical reaction in the linearized governing equations. The incompressible flow equations or at most, flow equations under the low-Mach-number assumption including the conservation of momentum, mass and energy are used, taking the velocity and density in the mean flow as inputs. Such analysis, which was recently denoted as the passive flame approach (Casel et al. 2022), allows to capture the purely hydrodynamic modes and coherent structures in turbulent flames. Indeed, those hydrodynamic modes and structures naturally exist in the turbulent flames, and they have been used to stabilize the flame either in the context of the bluff-body- or swirl-stabilized flames (Chen et al. 1990; Poinso 2017).

The effect of reactant density ratio on the instability of bluff body flames was investigated by calculating the hydrodynamic modes (Emerson et al. 2012; Emerson and Lieuwen 2015; Suresha et al. 2016; Emerson et al. 2016). At different preheated reactant temperatures, the authors conducted local stability analysis on the experimental data of velocity and density profiles of turbulent mean flow. The results show that the flame is convectively unstable at high flame density ratio between the unburnt and burnt gas. At low density ratio, the flame becomes absolutely unstable. These results on the mean flow profile are consistent with the experimental observations. The direct and adjoint modes obtained from the local analysis were used to reconstruct the global mode shapes, consistent with the conditionally averaged velocity fields from experiments at limit cycle.

Aiming at investigating the role of precessing vortex core (PVC) dynamics in combustion instability, Oberleithner *et al.* performed modal analysis on experimental data of turbulent flames in a swirl combustor (Oberleithner et al. 2015a,b). A solver based on

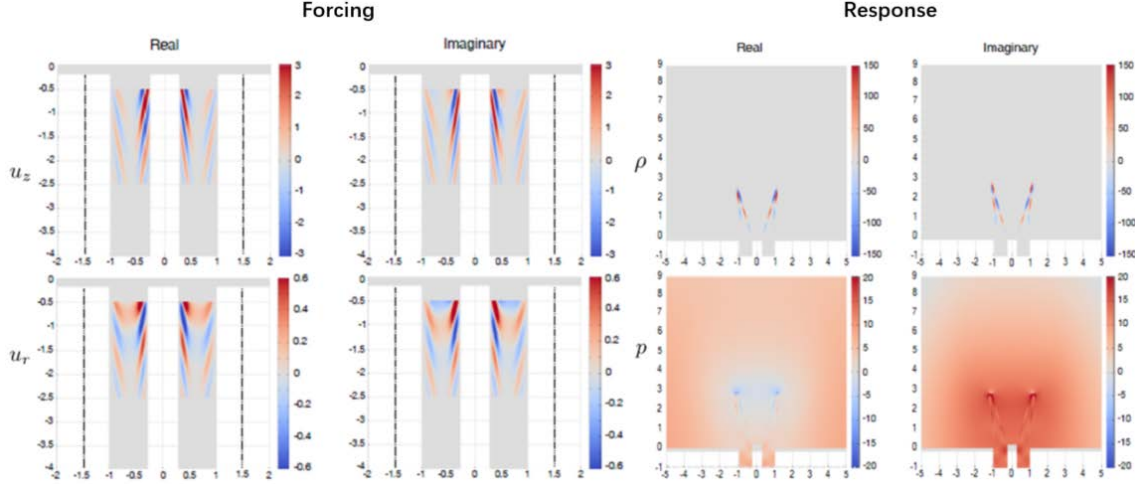


Figure 1.7: Optimal forcing and response structures in a M-shaped flame obtained by the resolvent analysis (figures taken from Blanchard 2015). The region of optimal forcing identified is inside the inflow channels.

the linearized incompressible Navier-Stokes equations with an eddy-viscosity model was applied. The predicted frequency of the instability mode was found to be in excellent agreement with the oscillation frequency measured in the experiment. The resolvent analysis on the turbulent mean flow via the passive flame approach was carried out to estimate the coherent structures in jet flames (Kaiser et al. 2019a; Casel et al. 2022). At low frequencies, the resolvent analysis produces coherent structures consistent with the results of spectral proper orthogonal decomposition (Picard and Delville 2000) from experimental data. However, at high frequencies, the results are less consistent because the effect of reaction was not considered in the passive flame approach.

The papers summarized above indicate that the linearized chemistry is more commonly used to study laminar flames, but rarely for turbulent flames. It seems to be a dilemma that towards studying the more complex turbulent flames, the linearization of chemical reactions around the mean flow may not work well. In this thesis, as the starting point of developing a new code, we pursue the analysis of laminar flames with linearized chemistry, which is expected to be extended to turbulent flames in the future.

1.3.3 Global linear analysis in diffusion flames

Global linear analysis has also been carried out in lifted non-premixed jet flames (Nichols and Schmid 2008; Qadri et al. 2015, 2021). The governing equations did not include the equations of species transport with consumption or production rates due to chemical reaction. Instead the authors used the transport equation of a mixing scalar varying from 0 to 1 that represents the reaction progress. The buoyancy-induced flickering of a diffusion jet flame was investigated via the global modal analysis based on a formulation with infinitely fast reaction rate (Moreno-Boza et al. 2016). Recently, the frequency response of a reacting jet in cross flow was investigated through identifying the optimal forcing and response structures (Sayadi and Schmid 2021). The presence of reaction significantly changes the dominant frequency and the optimal forcing structures, with respect to the non-reacting jet in cross flow.

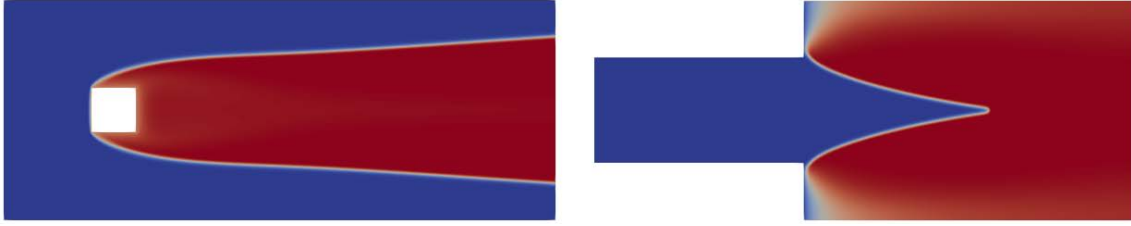


Figure 1.8: Two main configurations investigated in this thesis. Left: a bluff-body stabilized flame, acting as an oscillator; right: a slot flame, acting as an amplifier. The base flow temperature fields are shown.

1.4 Objectives

This thesis aims to apply recent developments of methodology from the field of linear instability theory to the study of combustion instability.

The flame instability that we study here refers to the unsteady oscillations in the reacting flow field. It does not refer to a specific type of flame instability or mechanism, such as the Darrieus-Landau and thermodiffusive instability, or the quenching and blow-off mechanisms. However, these mechanisms, if present in the linear regime, are already taken into account through linearization of the complete flow field. The resonance effect due to the chamber mode associated with the classical thermoacoustic instability is not studied due to the very large extent of the computational domain that would be required to resolve an acoustic wavelength.

The premixed laminar flame dynamics is quantitatively assessed via the global linear tools, in the sense that the governing equations are resolved in the entire computational domain in two spatial dimensions. The compressible Navier-Stokes equations for the reacting flow are implemented, including one-step and two-step chemical reaction models for the methane-air reaction. The interplay between flow dynamics, chemical reaction and acoustics can be inherently accounted for and investigated in full detail. A novel code based on the finite-element method is developed to carry out linear analysis on the base and mean states of the flame.

Linear analysis has already been extensively used to study shear flow instability, either in the context of the self-sustained oscillator, or the amplifier driven by external perturbations. Hence, we extend those notions to the flame, by studying an oscillator-type flame and an amplifier-type flame. The configurations chosen are a bluff-body stabilized flame acting as an oscillator, and a slot flame acting as an amplifier, as shown in figure 1.8. In the case of the bluff-body stabilized flame, the global modes of base and mean states are calculated to predict the transition and capture the frequency of oscillation. A wavemaker analysis is carried out to identify the active flow region that drives the flame oscillations. In the case of the slot flame, an input-output formalism is used to characterize the response of the flame to external forcing. The optimal forcing structures that leads to the maximal flame response are identified by means of resolvent analysis. The results obtained from linear calculations are validated against the reference nonlinear calculations, such as the frequency of the oscillator and the FTF of the amplifier.

1.5 Thesis outline

In §2, a laminar premixed slot flame that acts as an amplifier to external perturbations is investigated via the nonmodal input-output analysis. The base flow of the flame is calculated through a two-step chemical scheme via the standard flame code AVBP developed

by CERFACS (Schonfeld and Rudgyard 1999). The FTF is calculated with our linear code to be compared against that obtained with AVBP. An energy gain associating the forcing and response is defined to characterize the input-output mechanism of the flame. The receptivity of global heat release rate fluctuations to arbitrary forcing structures is defined. The optimal forcing and their associated flame response at different frequencies are calculated by resolvent analysis, which reveals the most “dangerous” structures that lead to the maximal flame response.

In §3, a laminar premixed bluff-body stabilized flame that acts as an oscillator under a certain range of wall temperatures of the bluff body is investigated via global analysis. A Newton solver to calculate the steady base flow and a nonlinear timestepper to calculate the unsteady flow are developed. The bifurcation of the flame with respect to the bluff body wall temperature is studied by calculating the temporal growth of steady base states. A wavemaker analysis based on the decomposition of contributions to the eigenvalue is performed to unveil the dominant mechanism of flow instability. The modal analysis is performed on the time-averaged mean flow to predict the frequency of oscillation.

In §4, the preliminary results of an ongoing study of a V-shaped flame stabilized on an annular injector is presented. The global modes of the flame are calculated in a geometry where the intrinsic thermoacoustic instability mode is expected to occur.

In §5, a side project of this thesis is presented about the effect of streaks on the instability of non-reacting incompressible jets. Large-scale coherent structures like streaks are present in boundary-layer flames (Miller et al. 2017, 2018; Ren et al. 2022), and recently the presence of streaks has been observed in jets as well (Nogueira et al. 2019). Thus, it is expected that streaks may be present as well in jet flames and other turbulent flames. Towards studying the coherent structures in turbulent flames, we begin with a fundamental study about the impact of streaks on the non-reacting jet instability. Optimal perturbations in a cross-section of the jet are considered as the rolls and streaks. Local stability analysis is then performed on the perturbed round jets.

In §6, the main contributions of this thesis are summarized, followed by four perspectives for future studies.

In the appendix A, the mathematical formulations of all the linear tools used in this thesis is presented. The definitions of direct and adjoint modes are given first, followed by the wavemaker and base flow sensitivity analysis based on the direct and adjoint modes. Nonmodal analysis formulated in temporal and frequency domain is then presented.

In the appendix B, a description of codes developed during this thesis is presented. The main functions in the code used for the bluff body stabilized flame are described with some tips for convergence in calculations.

CHAPTER 2

Resolvent analysis of a slot flame

The instability of a two-dimensional slot flame that acts an amplifier of external perturbations is investigated. A paper accepted to be published in *Combustion and Flame* is presented (Wang et al. 2022a), following the study context and two test cases for code development.

Contents

2.1	Strategies of forcing a flame	14
2.2	Test cases	15
2.2.1	Heated slit	16
2.2.2	Flame with one-step chemical scheme	16
2.3	Paper: Linear instability of a premixed slot flame	19
2.3.1	Introduction	19
2.3.2	Nonlinear simulation of a steady slot flame	22
2.3.3	Methods	23
2.3.4	The flame transfer function	26
2.3.5	Receptivity of global heat release rate fluctuations to arbitrary forcing	30
2.3.6	Resolvent analysis	31
2.3.7	Conclusions	36
2.4	Further discussions	39
2.4.1	Projection on the basis of resolvent modes	39
2.4.2	Sensitivity to numerical domain length	39
2.4.3	Choice of response norms	41
2.4.4	Eigenmodes of the flame	41
2.4.5	Orr-mechanism	41
2.4.6	Impact of flame attachment	42

2.1 Strategies of forcing a flame

In this chapter, we consider the response to forcing of a slot flame. The flame response here refers to the fluctuations of the flow quantities around the steady base flow induced by an external forcing. In real experiments, the forcing of a flame is often realized by the acoustic waves consisting of a single frequency or a band of frequencies emitted from a loudspeaker. In numerical simulations, there are generally three methods to force the flame.

The first method is to impose a fluctuating velocity profile at the inlet. In nonlinear simulations, this can be achieved by a fluctuating profile of very small amplitude superposed on the base flow. The frequency of the fluctuating signal can be harmonic or broad-band. If it is harmonic, the FTF is required to be computed on each frequency. If it is broad-band, the FTF over a certain range of frequency can be obtained with a system identification approach (Polifke et al. 2001a). In the linear setting, it is sufficient to impose a non-homogeneous Dirichlet boundary condition on the fluctuating inlet velocity, and then solve the corresponding system of a given frequency. We use this method in §2.2 and §2.3.4 to test the linear solver.

The second method is to impose an acoustic excitation of ingoing characteristic waves at the upstream boundary (Kaess et al. 2008; Silva et al. 2017). The amplitude of ingoing characteristic waves is f , which results in an outgoing wave of amplitude g produced by the flame response and the acoustic scattering. To this end, an ingoing-outgoing amplitude gain can be defined as

$$H(\omega) = \frac{\hat{g}}{\hat{f}}, \quad (2.1)$$

where ω is an angular velocity and \hat{g} , \hat{f} are the Fourier transforms of forcing f and response g . In both work of Kaess et al. 2008; Silva et al. 2017, the peaks in the defined gain were found to be uncorrelated with the peaks in the flame transfer functions. Furthermore, in Silva et al. 2017, one of the peaks was found to be associated with an intrinsic thermoacoustic feedback. Previous analysis suggests that the fundamental ITA mode may occur at a frequency where the phase of FTF passes $-\pi$ (Hoeijmakers et al. 2014; Emmert et al. 2015; Courtine et al. 2015), which is called the π -criterion of the ITA mode. The fundamental peak in $H(\omega)$ approximately occurs at the frequency where the ITA is predicted to arise according to the π -criterion. It was also tested that this peak is insensitive to the domain length, independent of the chamber mode. In this chapter, we have a very similar observation for the peaks of a defined input-output gain, but we use a source term as forcing, presented as the third strategy in the next paragraph.

The third method is to add a source term in the governing equations. Blanchard et al. 2015 applied this method to calculate the impulse response of a M-shaped flame by adding a spatial-dependant source term in each conservation equation. The source term is uniform in the radial direction, situated in the upstream channel with an amplitude of Gaussian distribution in the streamwise direction. The calculation was conducted in the frequency domain, so the source term can be understood as a harmonic forcing term driving the dynamics in the set of linearized equations. In the studies of non-reacting shear flows, adding a source term in the linearized equations is a routine concept often addressed as volume forcing to emphasize that forcing is spatially distributed, contrary to boundary forcing (Garnaud et al. 2013b). This concept has been widely used to model the localized forcing generated by a control device inside the flow region (Barbagallo et al. 2009, 2012), and to model the Reynolds stress in turbulent shear flows by means of resolvent analysis (McKeon and Sharma 2010; Beneddine et al. 2016; Lesshafft et al. 2019). An input-output gain relating a chosen norm of forcing and response is often introduced to quantify the

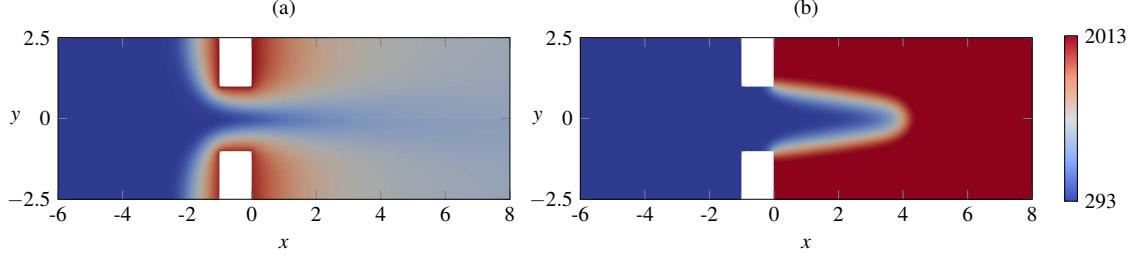


Figure 2.1: Base flow temperature field (unit Kelvin) of validation cases: (a) heated slit; (b) flame with one-step reaction. The units of width and length are centimeters.

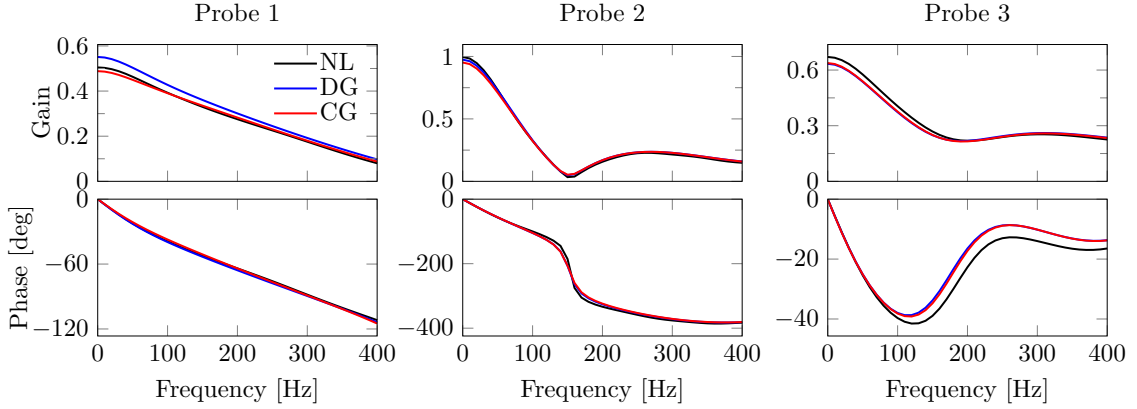


Figure 2.2: Point-to-point transfer function $\gamma(\mathbf{x}) = \rho(\mathbf{x})$ in the heated slit case. The probe positions are chosen at (2,0), (6,0) and (4,1) accordingly with the computational domain in figure 2.1(a).

amplification effect of the flow and the efficiency of the prescribed forcing.

2.2 Test cases

The present section consists of two validation cases provided by Max Meindl and Wolfgang Polifke from TU Munich that helped the development of our linear code. We use the first method of forcing, with a non-homogeneous Dirichlet boundary condition for inflow velocity. We measure the defined transfer functions against the reference calculations.

The code developed at TU Munich (Avdonin et al. 2019; Meindl et al. 2021) uses the Discontinuous Galerkin (DG) method for spatial discretisation, whereas our linearized solver developed for this slot flame uses the Continuous Galerkin (CG) method. This allows a code-to-code validation on the same base state. Two steady bases states of the same geometry simulated by OpenFOAM are used to test our CG linearized solver, with respect to the result from the DG solver, and nonlinear (NL) simulations.

The geometry of the calculation domain consists of a premixing chamber (5cm×5cm) and a combustion chamber (8cm×5cm) connected by a narrow slit (1cm×2cm). In the first case, the wall around the slit is heated, but there is no chemical reaction. In the second case, the flame is ignited. The geometry and the temperature field associated with both cases are presented in figure 2.1.

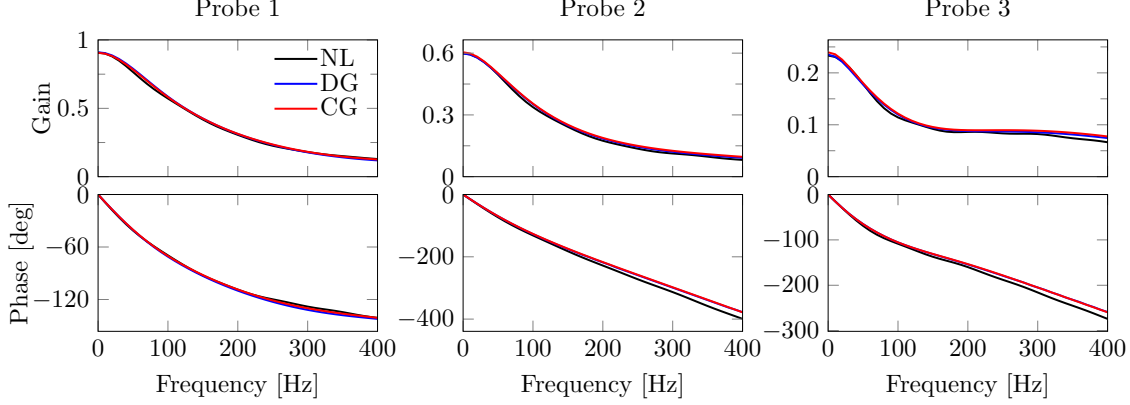


Figure 2.3: Point-to-point transfer function $\gamma(\mathbf{x}) = \rho(\mathbf{x})$ in the heated slit case. The probes are chosen at the same positions as figure 2.2.

2.2.1 Heated slit

The first validation case serves as a validation of the solver when only momentum, continuity, and enthalpy equations are included. There is neither transport of species nor chemical reaction. It consists of a flow passing through a heated slit with neither chemical heat release nor inner heat source. The Reynolds number at the inlet is 20. The hot wall around the slit is set to isothermal condition with its temperature equal to 2 000 K.

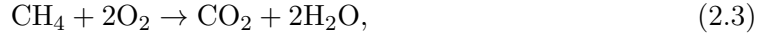
We force the flow system with a non-homogeneous Dirichlet boundary condition \mathbf{u}'_{ref} on the streamwise velocity fluctuations at the inlet. The volume forcing is set to zero. In this case, there is no chemical heat release. Thus, we define a point-to-point transfer function $F(\omega, \mathbf{x})$ that associates a flow variable $\gamma(\mathbf{x})$ inside the computational domain at a position \mathbf{x} with the reference forcing \mathbf{u}'_{ref} imposed at the inlet, in the form

$$F(\omega, \mathbf{x}) = \frac{\gamma'(\mathbf{x})}{\bar{\gamma}(\mathbf{x})} \frac{\bar{\mathbf{u}}_{ref}}{\mathbf{u}'_{ref}}. \quad (2.2)$$

We choose $\gamma(\mathbf{x}) = \mathbf{u}(\mathbf{x})$ and $\gamma(\mathbf{x}) = \rho(\mathbf{x})$, and calculate the transfer function at three positions inside the downstream chamber. The results are presented in figure 2.2 for $\gamma(\mathbf{x}) = \mathbf{u}(\mathbf{x})$, and in figure 2.3 for $\gamma(\mathbf{x}) = \rho(\mathbf{x})$. These results show excellent agreement of our CG solver with respect to the reference DG and NL calculations.

2.2.2 Flame with one-step chemical scheme

The second validation case is a premixed air-methane flame with a one-step chemical scheme (Avdonin et al. 2019). The detailed parameters can be found therein. The thermal boundary condition for the slit is adiabatic. The temperature field of the base flow is presented in figure 2.1(b). The chemical model used is a one-step global reaction scheme



where the progress rate \mathcal{Q} is modelled by the Arrhenius law

$$\mathcal{Q} = A \rho^{a+b} \frac{Y_{\text{O}_2}^a Y_{\text{CH}_4}^b}{W_{\text{O}_2}^a W_{\text{CH}_4}^b} \exp\left(-\frac{T_a}{T}\right), \quad (2.4)$$

with A , T_a , a and b model parameters, W_{O_2} and W_{CH_4} molecular mass of O_2 and CH_4 . The perturbation of progress rate \mathcal{Q}' writes

$$\mathcal{Q}' = \bar{\mathcal{Q}}((a+b)\frac{\rho'}{\bar{\rho}} + \frac{T_a T'}{\bar{T}^2} + a\frac{Y'_{\text{O}_2}}{\bar{Y}_{\text{O}_2}} + b\frac{Y'_{\text{CH}_4}}{\bar{Y}_{\text{CH}_4}}). \quad (2.5)$$

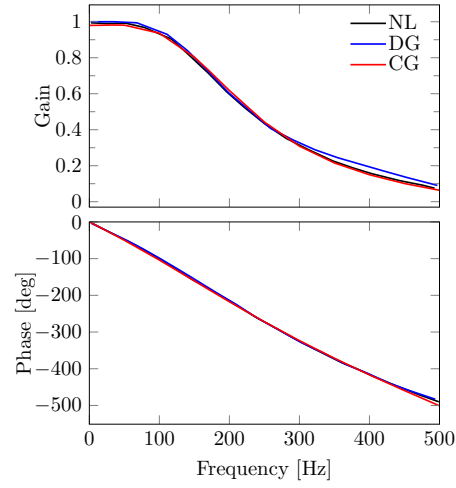


Figure 2.4: Flame transfer function for the case of one-step chemical scheme

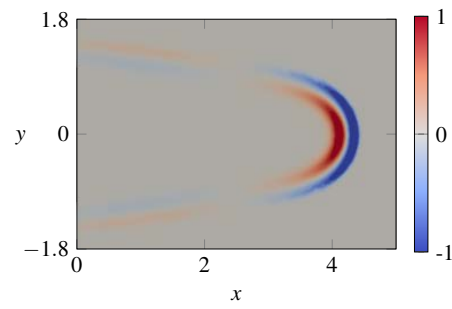


Figure 2.5: Real part of the fluctuating heat release rate. Values normalised by the maximum value of real part. The units of width and length are centimeters.

Following the same formulation as Avdonin et al. 2019, we only have the transport equation of Y'_{CH_4} in the linear system, because the fuel air is a lean mixture with equivalence ratio equal to 0.8. The fluctuation Y'_{O_2} is represented as $Y'_{\text{O}_2} = \frac{2W_{\text{O}_2}}{W_{\text{CH}_4}} Y'_{\text{CH}_4}$. The steady base state \bar{Y}_{O_2} is directly exported from OpenFOAM. The fluctuation of reaction rate for CH_4 and chemical heat release write $\dot{\omega}'_{\text{CH}_4} = -W_{\text{CH}_4} \mathcal{Q}'$ and $\dot{\omega}'_T = -\Delta h_f^\circ \mathcal{Q}'$.

An accurate match of FTF is found against reference calculations, as presented in figure 2.4. The structure of heat release fluctuation is presented in 2.5, in good agreement with figure 4 in Avdonin et al. 2019. Note that to test the influence of compressibility, we use a fully compressible formulation with $p = R_s \rho T$ as the state equation and we also use a low-Mach-number formulation with $p_0 = R_s \rho T$ as the state equation. Both solvers give very close results of FTF with respect to each other, which would be visibly the same line if plotted in figure 2.4. It seems that the compressibility does not play an important role in the FTF results.

The linear code developed has been validated through the calculation of transfer functions against OpenFOAM. In the following paper (Wang et al. 2022a), we study the forcing response of a slot flame calculated by AVBP.

2.3 Paper: Linear instability of a premixed slot flame

Linear instability of a premixed slot flame: flame transfer function and resolvent analysis

Chuhan Wang¹, Thomas Ludwig Kaiser², Max Meindl³, Kilian Oberleithner²,
Wolfgang Polifke³, Lutz Lesshafft¹

¹Laboratoire d’Hydrodynamique, CNRS / Ecole Polytechnique / Institut
Polytechnique de Paris, Palaiseau, France

²Laboratory for Flow Instabilities and Dynamics, Technische Universität Berlin,
Berlin, Germany

³Technical University of Munich, Munich, Germany

Submitted 13 September 2021, revised 22 December 2021; accepted 21 January
2022

Abstract

The response to forcing of a 2D laminar premixed slot flame is investigated by means of linear analysis, based on the compressible flow equations with a two-step reaction scheme for methane combustion. The flame transfer function (FTF) is computed from this linear model, in excellent agreement with reference nonlinear calculations. The input-output gain between externally applied forcing and the global heat release rate response is computed, and peaks in the gain are related to intrinsic thermoacoustic (ITA) modes. The receptivity of the flame to arbitrary flow forcing is characterised by the resulting amplitude of global heat release rate fluctuations. Linear resolvent analysis is used to identify optimal forcing structures and their associated flame response, leading to a discussion of the dominant mechanisms for the amplification of flow perturbations, which trigger flame oscillations. These seem to involve a resonance with ITA instability modes.

Keywords— combustion instability, linear instability, premixed laminar flame, flame transfer function; resolvent analysis, intrinsic thermoacoustic mode

2.3.1 Introduction

Flames are known to show unstable behaviour across nearly all technically relevant parameter regimes and configurations. Such unstable flame dynamics pose a major problem in the design of combustion systems, because they limit performance, reduce lifetime, and restrict operating conditions. In the most traditional sense, instability denotes the potential of a flame, or any flow, to develop self-sustained large-amplitude oscillations, which usually can be characterised by a temporally growing eigenmode of the linearised system of governing equations. In a larger sense, instability analysis is not limited to the description of growing eigenmodes and the ensuing “oscillator behaviour”; it can also be used to characterise the potential of a flow to *amplify* perturbations in response to external forcing (“amplifier behaviour”, see Huerre and Monkewitz 1990). These two approaches are often referred to as “modal” versus “non-modal” analysis in the literature. In the

present study, we aim to characterise the non-modal amplifier behaviour of a slot flame configuration, which does not exhibit modal instability. The mechanisms that contribute to modal or non-modal instability dynamics may be intrinsic to the flame and its supporting flow field (Matalon 2007), or they may involve an acoustic resonance between the flame and its surrounding chamber (Lieuwen 2003). Chamber resonance effects, which underpin the classical thermoacoustic instability, are not investigated in this paper.

Flame instability has been approached in weakly and fully nonlinear frameworks (Noiray et al. 2008; Juniper and Sujith 2018), but linear analysis still plays an important role in fundamental studies and industrial applications, such as sensitivity analysis, optimisation and control (Magri 2019). The linear flame transfer function (FTF), which relates fluctuations of the global heat release rate to local fluctuations of the velocity in a chosen measurement point, is widely used for the modelling of the flame response to acoustic forcing. Classically, the flame transfer function is obtained from experiments or numerical simulations via empirical system identification methods based on time-series of forcing and response data. This strategy is data-driven, and represents a *black-box* approach (Polifke 2014). We advocate here an alternative strategy, based on the linear flow equations, which may be described as a *white-box* method. To this end, we linearize the governing equations and calculate the Jacobian matrix around a steady base flow state, which is obtained as a fixed point of the nonlinear system of equations. The resulting linear system governs the dynamics of small-amplitude fluctuations, and it can be accessed with a large variety of linear tools for a physics-based analysis. Note that our objective is not to create analytical models of the FTF, as one might do for instance by using a G-equation (Schuller et al. 2003a). The single hypothesis that we employ here is that we work with fluctuations of small amplitudes in the linear limit. The complete set of linearized governing equations and the information of each flow variable in the base flow is preserved.

This method allows efficient calculation of the FTF, because no time-stepping is required. A pioneering attempt in this direction was made by Kampen et al. 2007 to reduce the computational burden of FTF calculations by use of a “linear coefficient method”, based on the response of flow variables to small-amplitude perturbations. The response of global heat release rate to the fluctuation of inlet equivalence ratio was investigated for a turbulent swirling flame. The response obtained via the linear coefficient method was reported to be in good agreement with reference calculation results. Nevertheless, this method does not include some essential characteristics of the flame dynamics, such as the effect of equivalence ratio fluctuations on the flame front movement. The approach used in the present study fully encompasses those effects.

Another important feature is that the white-box method gives spontaneously a *multi-input, multi-output* (MIMO) system. While the classical flame transfer function is represented as a *single-input, single-output* (SISO) system associating the heat release rate with velocity disturbances, one may also want to explore other physical quantities in flames. A MIMO formulation is required if one wants to, for instance, compute the flame responses to incoming fluctuations of the mixture composition (Sattelmayer 2003; Cho and Lieuwen 2005; Dowling and Mahmoudi 2015; Steinbacher et al. 2018; Yang et al. 2020), or represent acoustic scattering (Åbom and Bodén 1988; Polifke et al. 2001b). MIMO systems can in principle be identified with black-box methods, but special technical considerations are necessary, for instance so as to ensure statistical independence among different signal channels (Polifke 2014; Föller and Polifke 2012). A linear approach, as presented in this study, inherently preserves the causal coupling between all signals, and all mappings can be extracted from one linear system.

The applicability of linear analysis to flame dynamics has already been demonstrated in several recent studies, for premixed as well as diffusion flames. Throughout this paper,

the linear analysis is carried out in a *global* setting, i.e. on a spatially developing base flow, in contrast to *local* analysis which is based on the assumption of a streamwise-invariant base flow. For reacting flows, local analysis has indeed been successfully applied in reacting bluff-body wakes that can be regarded as being weakly non-parallel (Emerson et al. 2016). This assumption however does not hold for most flames, so we use global analysis where the word “global” means that the variations in the base flow are resolved both in the streamwise and in the cross-stream direction. A brief state-of-the-art survey is given for such studies on premixed flames. The reader may want to refer to Qadri et al. 2015; Nichols and Schmid 2008; Moreno-Boza et al. 2016; Qadri et al. 2021; Sayadi and Schmid 2021 for work on diffusion flames.

Investigating the role of precessing vortex core (PVC) dynamics in combustion instability, Oberleithner et al. 2015a,b performed modal analysis on experimental data of turbulent flames in a swirl combustor. A solver based on the linearized incompressible Navier-Stokes equations with an eddy-viscosity model was applied. The predicted frequency of the instability mode was found to be in excellent agreement with the oscillation frequency measured in the experiment. For other linear calculations with regard to the PVC, the reader may refer to (Tammisola and Juniper 2016; Stöhr et al. 2018).

Blanchard et al. 2015 developed a linear solver based on the compressible Navier-Stokes equations with a one-step chemistry scheme. The FTF of a steady M-shaped premixed laminar flame was calculated. The frequencies with maximum and minimum FTF gain were correctly retrieved, with respect to experimental measurements, but discrepancies in the gain values remained, presumably due to the simplicity of the chemistry model. By performing non-modal analysis, the authors characterized the physical interactions that give rise to pressure wave generation in the flame front (Blanchard et al. 2016). This study was recently extended to swirling M-flames by Skene and Schmid 2019.

Recent work on premixed laminar flames, by Polifke and coworkers (Avdonin et al. 2019; Albayrak et al. 2018; Meindl et al. 2021), is highly relevant to the present study. The objective of Avdonin et al. 2019 was to introduce a new approach that can accurately predict FTFs and thermoacoustic modes. The linearized reactive flow approach (LRF) that contains the set of equations of a reacting flow, was used to calculate the FTF, quantitatively validated against results obtained by nonlinear timestepping. The global eigenmodes were then calculated with the LRF solver. Due to the limitation of the computational domain, the thermoacoustic mode associated with the combustion chamber could not be captured. Instead, another scenario of acoustic feedback taking place within the flame was identified. Such a scenario independent of the chamber mode is known as the intrinsic thermoacoustic instability (ITA) mode (Hoeijmakers et al. 2014; Courtine et al. 2015; Emmert et al. 2015). Global eigenmodes were found at the frequencies where the ITA modes are expected to occur. The unstable eigenmode structures showed a distortion of the flame front induced at the flame root. Entropy waves generated by acoustically forced premixed slot flames, including a freely propagating 1D flame and a 2D slot flame, were calculated (Meindl et al. 2021), via the LRF approach and a hybrid approach that combined the linearized incompressible Navier-Stokes equations and the FTF (LNSE+FTF approach). The LNSE+FTF approach generated spurious entropy waves, whereas the entropy waves as well as the FTF obtained through the LRF are in quantitative agreement with reference results. The LRF solver was also used to study the interaction between inertial waves and flames (Albayrak et al. 2018). The inertial waves have non-zero axial and radial components, which bring the flame out of kinematic balance and thereby cause changes in flame shape and heat release. The flame front was found to be modulated mainly by axial and radial velocity fluctuations associated with inertial waves.

In closely related fields, global linear analysis has been widely applied with great success

in shear flows where instability dynamics lead to an amplification of external perturbations (Schmid and Henningson 2001). Such dynamics are commonly investigated by means of *resolvent analysis*; this formalism can be applied to laminar as well as turbulent flow regimes, as demonstrated for jets (Garnaud et al. 2013b; Beneddine et al. 2016; Lesshafft et al. 2019), backward-facing step flow (Barbagallo et al. 2012) and channel flow (McKeon and Sharma 2010; Morra et al. 2019), among other configurations. In the resolvent framework, optimal forcing and associated flow response structures are identified in the frequency domain to quantitatively analyse the amplification of flow perturbations. In recent years, resolvent analysis has been applied also to the configuration of turbulent flames. Kaiser et al. 2019a showed that the method is able to model the hydrodynamic response of a swirled flame to acoustic perturbations. Casel et al. 2022 further demonstrated the capabilities of the resolvent analysis to model the dominant coherent hydrodynamic structures in a fully turbulent Bunsen flame. Note however, that these two studies do not account for coherent fluctuations of heat release rate, which restricts these analyses to purely hydrodynamic mechanisms.

In the present work, we construct a linear reacting flow model, on which we base a discussion of the physical mechanisms that lead to selective amplification of certain frequencies in the flame. Linear analysis of multi-physics dynamics in a laminar slot flame obtained from nonlinear simulation is presented, where two spatial dimensions are resolved. In the framework of resolvent analysis, we identify the precise flow forcing that elicits maximally energetic flame oscillations. Specifically, one of the configurations that we are interested in is the flame response to perturbations of fuel equivalence ratio. The resolvent analysis can shed light on the most “dangerous” structures that lead to the maximal flame response, which can inform a detailed discussion of the physical mechanisms of perturbation amplification. Our linear model accounts for the non-parallelism of the flow field, for chemical reaction, and for the coupling of acoustic and vortical perturbations. Reactions are modelled by a two-step chemical scheme.

The paper is organized as follows. In Section 2.3.2, the steady flame configuration is presented, which is used as a base flow in the following linear analysis. In Section 2.3.3, the nonlinear governing equations are documented, including details of the chemical scheme, and the linearized system is introduced. The FTF is calculated in Section 2.3.4 with boundary forcing, which serves as a validation of our linear system with respect to that obtained from nonlinear timestepping. To quantify the efficiency of the flame actuation in the FTF scenario, an input-output analysis is then introduced. In Section 2.3.5, the influence of arbitrary forcing on the global heat release rate is characterized via a receptivity analysis. Finally, resolvent analysis is conducted in Section 2.3.6 with optimisation norms of different physical quantities. Conclusions and perspectives are given in Section 2.3.7.

2.3.2 Nonlinear simulation of a steady slot flame

We perform a time-discrete, fully nonlinear laminar direct numerical simulation of a two-dimensional perfectly premixed slot flame. The time stepping is performed using the AVBP code developed by CERFACS (Schonfeld and Rudgyard 1999), which solves the governing equations using the cell-vertex method. The two step Taylor-Galerkin method (TTGC) (Colin and Rudgyard 2000) is applied for the discretization of the advective term, which, for the triangular grid, is third-order accurate in space and time. For the diffusive fluxes an adaptation of the finite-element Galerkin method to the cell-vertex method is applied (Colin et al. 2003). The reaction chemistry is modelled by the BFER scheme (Franzelli et al. 2012). The model accounts for six transported species and two reactions. The reactions are based on an Arrhenius term with pre-exponential correction factors,

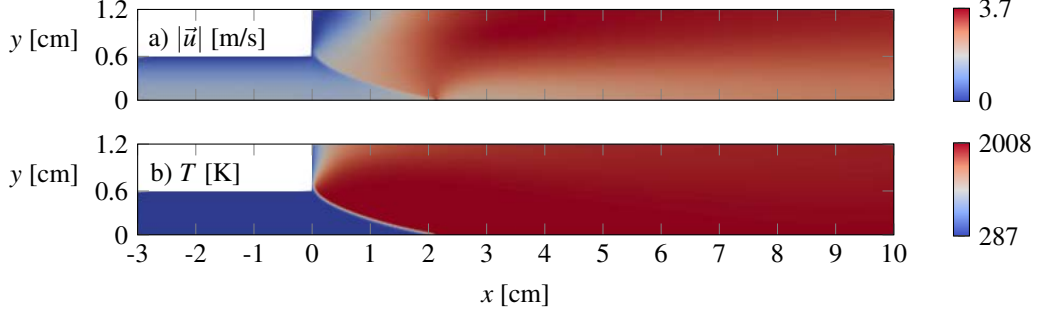


Figure 2.6: Steady base flow state, obtained from nonlinear simulation with AVBP: a) velocity magnitude; b) temperature. The numerical domain resolves half of the flame, with a symmetry condition at the center line ($y = 0$).

which assure correct laminar flame speeds over a large range of fresh gas temperatures, pressures and equivalence ratios.

The flow domain is 10 cm long and 2.4 cm wide, including an inflow channel of length 3 cm and width $H = 1.2$ cm. A symmetry condition along the centerline $y = 0$ allows us to restrict the calculations to the half-domain, shown in figure 2.6. The inflow conditions for bulk speed, temperature and equivalence ratio are chosen as

$$U = 1 \frac{\text{m}}{\text{s}}, T_0 = 287\text{K}, \phi = 0.8. \quad (2.6)$$

This results in an inflow Reynolds number $\text{Re} = \rho_0 U H / \mu_0 = 728$, where ρ_0 and μ_0 denote the density and the dynamic viscosity at the inflow, respectively.

At the inlet and at the outlet, Navier-Stokes characteristic boundary conditions (NSCBC) are applied (Poinsot and Lele 1992). An acoustically hard inlet condition is used at the inlet, where a parabolic velocity profile is prescribed. An acoustically soft outlet condition lets acoustic waves exit the domain with minimal reflection. The no-slip wall boundaries at $(x < 0, y = 0.6 \text{ cm})$ and $(x = 0, y > 0.6 \text{ cm})$ are isothermal, where the temperature is equal to the one of the unburnt gas, T_0 . In addition to the symmetry boundary condition at the center plane of the flame, a second symmetry condition is applied at the upper boundary ($y = 1.2 \text{ cm}$).

2.3.3 Methods

2.3.3.1 Nonlinear governing equations

The compressible reactive flow equations, which are to be linearized around the base state for the following analysis, are formulated in terms of conservative variables $(\rho, \rho u, \rho v, \rho h, \rho Y_k)$ in Cartesian coordinates (x, y) , where (u, v) are the streamwise and cross-stream velocity components, ρ is the density, h is the sensible enthalpy and Y_k is the mass fraction of species k . Following the notation of Avdonin et al. 2019, these equations are given as

$$\frac{\partial \rho}{\partial t} = -\frac{\partial}{\partial x_j}(\rho u_j), \quad (2.7)$$

$$\frac{\partial \rho u_i}{\partial t} = -\frac{\partial}{\partial x_j}(\rho u_i u_j) - \frac{\partial p}{\partial x_i} + \frac{\partial \tau_{ij}}{\partial x_j}, \quad (2.8)$$

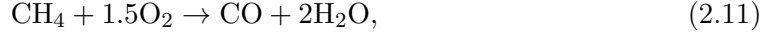
$$\frac{\partial \rho Y_k}{\partial t} = -\frac{\partial}{\partial x_j}(\rho u_j Y_k) - \frac{\partial J_j}{\partial x_j} + \dot{\omega}_k, \quad (2.9)$$

$$\frac{\partial}{\partial t}(\rho h - p) = -\frac{\partial}{\partial x_j}(\rho u_j h) - \frac{\partial q_j}{\partial x_j} + \dot{\omega}_T, \quad (2.10)$$

closed with the equation of state for an ideal gas $p = R_s \rho T$, where p is the pressure, T is the temperature, and R_s is the specific gas constant. The molecular stress tensor is given by $\tau_{ij} = -\frac{2\mu}{3} \frac{\partial u_k}{\partial x_k} \delta_{ij} + \mu \left(\frac{\partial u_i}{\partial x_j} + \frac{\partial u_j}{\partial x_i} \right)$. The molecular viscosity μ is modelled by a power law $\mu = c_1 (T/T_{\text{ref}})^b$, with tabulated constants c_1 , T_{ref} and b . The flux of species transport and heat transfer are modelled as $J_j = -D_k \frac{\partial Y_k}{\partial x_j}$ and $q_j = -\alpha \frac{\partial h}{\partial x_j}$, respectively. The transport coefficients are related by a Schmidt number $\text{Sc}_k = \frac{\mu}{D_k}$ for species k and a Prandtl number $\text{Pr} = \frac{\mu}{\alpha}$. Constant values $\text{Sc}_k = 0.7$ and $\text{Pr} = 0.7$ are chosen for the lean methane-air mixture, as prescribed in the BFER chemical scheme. For a mixture of N species, the aggregate sensible enthalpy is defined as $h = \sum_{k=1}^N h_k Y_k$, where the sensible enthalpy of species k is defined as $h_k = \int_{T_0}^T C_{p,k} dT$. The sensible enthalpy h_k and the heat capacity $C_{p,k}$ are linearly interpolated from JANAF tables through the same method as in AVBP.

The reaction rate $\dot{\omega}_k$ of species k , and the heat release rate due to combustion $\dot{\omega}_T$, are modelled by the two-step BFER chemistry scheme, based on the Arrhenius law. The reaction rate $\dot{\omega}_k$ for a chemistry scheme of overall M reactions is defined by $\dot{\omega}_k = W_k \sum_{j=1}^M \nu_{kj} \mathcal{Q}_j$, where W_k is the molecular mass of species k , ν_{kj} is the molar stoichiometric coefficient of species k in reaction j , and \mathcal{Q}_j is the progress rate of reaction j . The heat release rate is defined by $\dot{\omega}_T = -\sum_{j=1}^M \Delta h_{f,j}^o \mathcal{Q}_j$, where $\Delta h_{f,j}^o$ denotes the standard enthalpy of reaction corresponding to reaction j .

The BFER chemical scheme involves six species (CH_4 , O_2 , CO_2 , CO , H_2O , N_2) and two reactions,



The second reaction describing the equilibrium between CO and CO_2 is reversible. The progress rates \mathcal{Q}_1 and \mathcal{Q}_2 are given by

$$\mathcal{Q}_1 = \kappa_{f,1} [X_{\text{CH}_4}]^{n_{1,\text{CH}_4}} [X_{\text{O}_2}]^{n_{1,\text{O}_2}}, \quad (2.13)$$

$$\mathcal{Q}_2 = \kappa_{f,2} [X_{\text{CO}}]^{n_{2,\text{CO}}} [X_{\text{O}_2}]^{n_{2,\text{O}_2}} - \kappa_{r,2} [X_{\text{CO}_2}]^{n_{2,\text{CO}_2}}, \quad (2.14)$$

where $[X_k]$ is the molar concentration of species k defined by $[X_k] = \rho \frac{Y_k}{W_k}$. The forward reaction rate constant for reaction j is modelled by the Arrhenius law

$$\kappa_{f,j} = A_j f_j(\phi) T^{\beta_j} \exp\left(-\frac{T_{a,j}}{T}\right), \quad (2.15)$$

where f_j is a correction function with respect to equivalence ratio ϕ . The backward rate constant is linked to the forward rate via an equilibrium constant K as

$$\kappa_{r,2} = \frac{\kappa_{f,2}}{K}. \quad (2.16)$$

Values for the model constants A_j , $T_{a,j}$, β_j and n_j are taken from the BFER tables (Franzelli et al. 2012). In the study of Meindl et al. 2021, a different two-step chemical scheme (2S_CH4_CM2) was used, and the coefficients in the reaction model are not the same. In both studies, the equivalence ratio is 0.8, so both reaction models should be suitable to produce the correct flame properties (CERFACS 2017).

2.3.3.2 Linear analysis

The dynamics of small-amplitude fluctuations around a steady flow state are governed by linear equations. In what follows, we decompose the state variables $\mathbf{q} = (u, v, \rho, p, Y_k)$ into a base flow component $\bar{\mathbf{q}}$ and a fluctuation component \mathbf{q}' . This decomposition is introduced into Eqs. (2.7)-(2.10), and the terms are arranged into the form

$$\frac{\partial B\mathbf{q}'}{\partial t} - A\mathbf{q}' = P\mathbf{f}', \quad (2.17)$$

following the linearized governing equations (2.31-2.34) given in the Appendix (of this paper). All terms linear in \mathbf{q}' are on the left-hand side in Eq. (2.17), whereas all terms nonlinear in \mathbf{q}' are replaced by the vector \mathbf{f}' , which is interpreted as a forcing input into the linear system (McKeon and Sharma 2010; Beneddine et al. 2016). More specifically, for the following analysis, the vector \mathbf{f}' contains all non-zero forcing components, and the matrix P adds zero elements as required for the dimension of the linear system. P is therefore a rectangular matrix with only 0 and 1 as elements. The forcing vector \mathbf{f}' , in addition to the intrinsic forcing by nonlinear terms, may also represent external forcing that is applied at the domain boundaries. In this work, we consider forcing on streamwise velocity f_u , transverse velocity f_v , and fuel concentration f_{CH_4} . In the following, we will consider time-harmonic forcing $\mathbf{f}' = \hat{\mathbf{f}}e^{i\omega t}$ at frequency $\frac{\omega}{2\pi}$, and its associated time-harmonic response $\mathbf{q}' = \hat{\mathbf{q}}e^{i\omega t}$. This leads to a relation between $\hat{\mathbf{q}}$ and $\hat{\mathbf{f}}$ in the frequency domain

$$(i\omega B - A)\hat{\mathbf{q}} = P\hat{\mathbf{f}}. \quad (2.18)$$

In what follows, we use the flame Strouhal number $St = \frac{\omega H}{4\pi S_L}$ as a non-dimensional frequency (Blanchard et al. 2015), where the laminar burning velocity S_L is 0.29 m/s and the slot half-width $H/2$ is 0.6 cm.

The cumbersome linearization of the governing equations (2.7)-(2.10) is performed, as far as possible, by use of the symbolic calculus functionality provided by the Unified Form Language (UFL, see Alnæs et al. 2014). However, a few terms, like for example the sensible enthalpy interpolated from JANAF tables, require linearization by hand. We reduce the number of linearized species equations from six to four by transporting only CH_4 , O_2 , CO_2 and CO , and regarding H_2O and N_2 as passive scalars. More details about the linearization process are documented in the Appendix. It is important to keep in mind that Eqs. (2.7-2.10), from which our linear system is derived, are not strictly identical to those solved in the AVBP code, although we strived to stay close to this reference.

At the inlet and the outlet of the numerical domain, stress-free boundary conditions are imposed. These are a standard choice in finite element formulations for open boundaries (see for instance Garnaud et al. 2013b), generally found to have a weak influence on the dynamics in the domain interior. It has been checked that the numerical domain length has a negligible effect on the results of FTF, therefore the upstream and downstream boundary conditions can be considered to be appropriately transparent. At the inlet, the fluctuations of density and mass fraction of each species are set to zero. The fluctuations of velocity and density are set to zero along the wall. Cross-stream velocity fluctuations are set to zero at the centerline and at the upper boundary, consistent with the symmetry conditions used in AVBP.

The linear system and all analysis tools are implemented in Python, making strong use of the FEniCS framework. The continuous Galerkin method is used to discretize the partial differential equations on unstructured meshes, with finite elements of quadratic order.

The mesh used in the AVBP computations contains 450,358 cells, which is not easily affordable for matrix operations in the linear analysis. The base flow is therefore interpo-

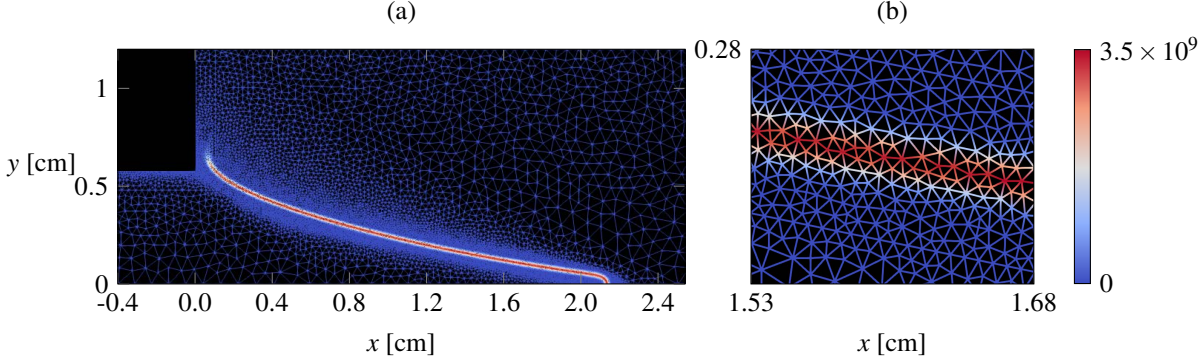


Figure 2.7: A portion of the standard mesh that is used throughout this study. Colors represent the base flow heat release rate $\dot{\omega}_T$ [J/m³/s] in order to visualize the flame front position.

lated on a less refined mesh of 19,278 elements for linear calculations, shown in Fig. 2.7. High spatial resolution is maintained in the reaction region and near walls.

2.3.4 The flame transfer function

2.3.4.1 Validation of the linear solver versus AVBP

For validation purposes, the flame transfer function (FTF) is computed with our linear solver, and compared to reference results obtained with AVBP. Such a validation strategy has already been used in Blanchard et al. 2015 against the experimental data, and in Avdonin et al. 2019; Albayrak et al. 2018; Meindl et al. 2021 quantitatively against the nonlinear timestepping results. The FTF is defined as

$$F(\omega) = \frac{\bar{u}_{\text{ref}} \dot{\Omega}'_T}{\dot{\bar{\Omega}}_T u'_{\text{ref}}}, \quad (2.19)$$

relating normalized fluctuations of the global heat release rate to those of a reference velocity. These two quantities are defined as $\dot{\bar{\Omega}}_T = \iint \dot{\omega}_T dx dy$, integrated over the entire computational domain, and u_{ref} the vertically averaged inflow velocity. As before, overbars denote base flow quantities, and primes denote fluctuations.

To obtain the reference FTF based on the AVBP simulations, the Wiener-Hopf inversion, a method of system identification, is performed. Instead of determining the FTF based on harmonic forcing frequency by frequency, the Wiener-Hopf inversion allows to apply a broad-band forcing, which also results in broad-band fluctuations in the heat release rate. The FTF is then determined in the post processing based on a statistical evaluation of the velocity fluctuations and the resulting heat release rate fluctuations. For more details on the method, the reader is kindly referred to Polifke et al. 2001a; Föller and Polifke 2012. The amplitude of perturbation velocity is chosen as 1% of the mean inflow velocity, such that the flow response can be considered to be in the linear regime. Modulus and phase of the FTF are shown in Fig. 2.8, and the harmonic flame response structures obtained from AVBP are visualized in the upper half of Fig. 2.9(a-h).

Corresponding calculations with our linear solver involve the solution of a matrix-vector problem, given by Eq. (2.18), for a given frequency. Consistent with the nonlinear simulation, the volume forcing $\hat{\mathbf{f}}$ is set to zero in these calculations, and the system is forced instead by a non-homogeneous Dirichlet boundary condition on the streamwise velocity fluctuations $\hat{\mathbf{u}}$ at the inflow. A typical calculation for one frequency value requires about 6 minutes on a single core (Intel i7-8700K, 3.70GHz), which is significantly cheaper than

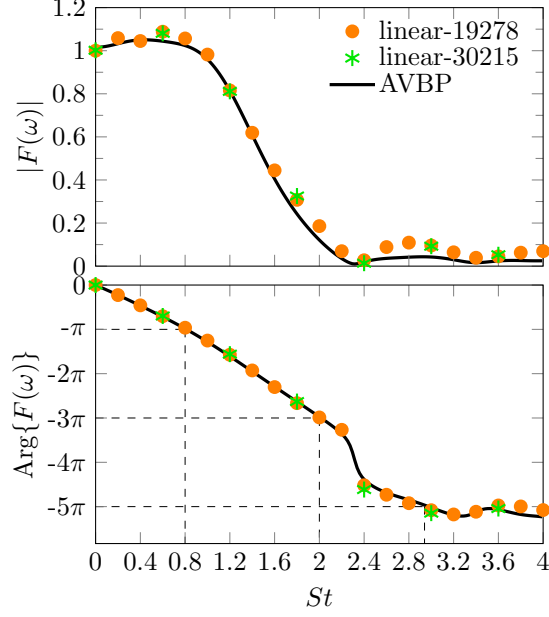


Figure 2.8: Flame transfer function: result obtained from AVBP by nonlinear timestepping with broad-band inflow boundary forcing, alongside results obtained from the linear solver through harmonic inflow boundary forcing with meshes of 19278 and 30215 elements. The auxiliary lines mark the phases at odd multiples of π associated with intrinsic thermoacoustic instability.

a corresponding AVBP run. Note that in AVBP for such a single harmonic calculation, the nonlinear timestepping over one period requires between 500 and 1000 CPU hours, depending on the frequency.

The FTFs obtained with both methods are compared in Fig. 2.8, and it is found that the linear solver accurately reproduces the AVBP results. Convergence of the linear calculations with respect to spatial resolution is confirmed by comparing the results from two different meshes. The coarser mesh, composed of 19278 triangular elements as shown in Fig. 2.7, will be used throughout this study. For further validation, snapshots of the linear flow response to harmonic inflow forcing at $St = 0.8$ are compared in Fig. 2.9 to the nonlinear simulation results, for several fluctuation quantities, and excellent agreement is observed.

2.3.4.2 Input-output gain

There are generally three ways to force fluctuations in a flame in numerical simulations. The first method is to prescribe an inflow velocity fluctuation, as has been done in the previous section. The second method is to specify an incoming acoustic wave through a characteristic boundary condition (Kaess et al. 2008; Silva et al. 2017). The third method is to introduce a source term in the governing equations, as is done in Blanchard et al. 2015. Any of these methods will induce a response of the flame. The FTF relates the global heat release rate fluctuation to an upstream velocity fluctuation, both of which are part of the flow response to the externally applied forcing. The FTF does not, however, relate the system response to the forcing input, as shown in Fig. 2.10.

We are interested in the question, how strongly the flame reacts to external forcing input of a given type and frequency. To this end, the forcing (input) and the response (output) must be measured by appropriate norms. For instance, previous flame studies (Kaess et al. 2008; Silva et al. 2017) identified the ratio of incoming (input) and outgoing

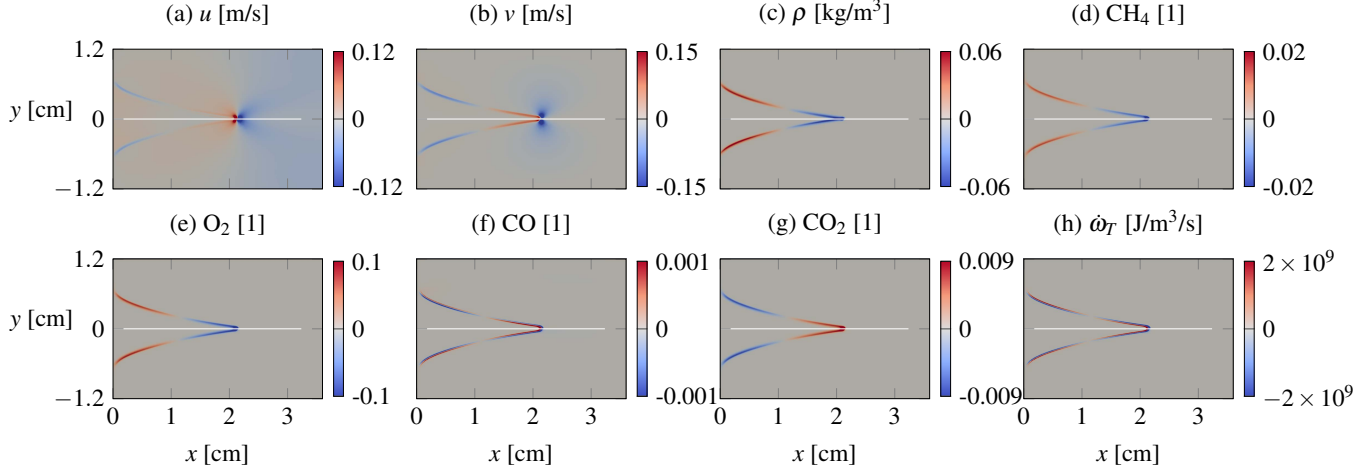


Figure 2.9: Response to inflow velocity forcing at $St = 0.8$. Upper half: nonlinear (AVBP); lower half: linear.

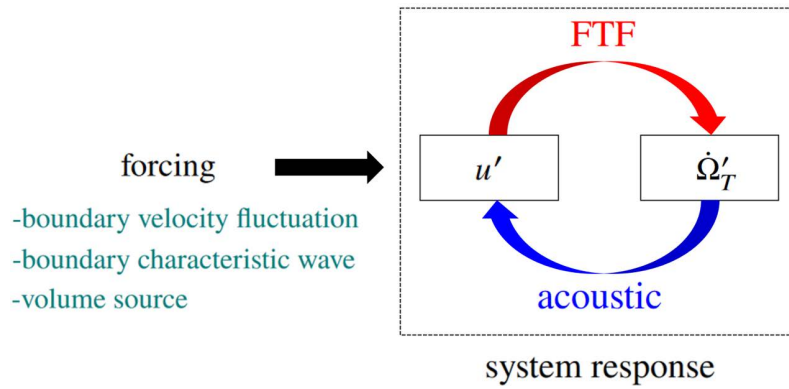


Figure 2.10: Illustration of the input/forcing and output/response. The FTF is established inside the response field.

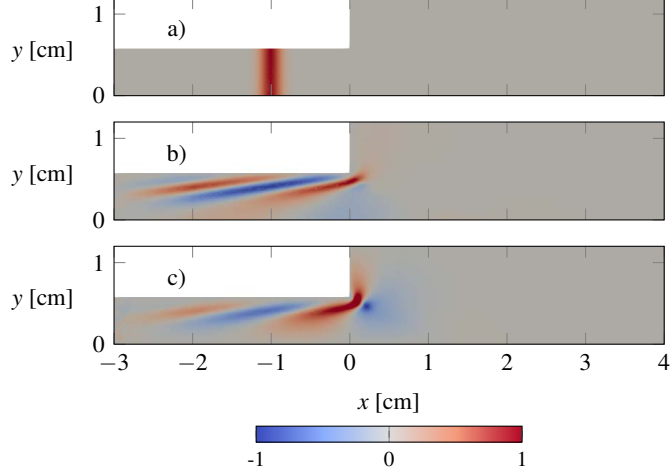


Figure 2.11: (a) flat Gaussian forcing \hat{f}_G with $x_c = -1$ cm and $w = 0.2$ cm on \hat{f}_u . b) receptivity field \hat{r} on \hat{r}_u . c) receptivity field \hat{r} on \hat{r}_v . The receptivity is calculated at $St = 0.8$. All the fields are normalised with their maximum value.

(output) acoustic wave amplitudes at the inflow boundary. It was found that the peaks of this amplitude gain do not coincide with those of the FTF gain.

We consider an external input in the form of volume forces f_u and f_v , as defined in Section 2.3.3.2, measured by their standard 2-norm,

$$\|\hat{\mathbf{f}}\|^2 = \iint_{\Omega} (|\hat{f}_u|^2 + |\hat{f}_v|^2) dx dy. \quad (2.20)$$

The flame response, as an output, is measured by the global heat release rate fluctuation $\hat{\Omega}_T$, consistent with the FTF definition. The *input-output gain* is then defined as

$$\sigma^2 = \frac{\hat{\Omega}_T^2}{\|\hat{\mathbf{f}}\|^2}. \quad (2.21)$$

We first design a volume force term that should allow us to reproduce the FTF. A Gaussian distribution in x , independent of y , is prescribed for the streamwise force component,

$$\hat{f}_G(x, y) = \exp \left[-\frac{(x - x_c)^2}{w^2} \right], \quad (2.22)$$

as is shown in Fig. 2.11a. The flame response is obtained as the solution of the linear system in Eq. (2.18), for two different center positions x_c and distribution widths w . A homogeneous Neumann condition on u at the inflow permits a non-zero volume flux across the boundary in the flow response. The FTF is evaluated according to the definition of Eq. (2.19) (u_{ref} still is the vertically averaged inflow velocity). The results are in excellent agreement with the FTF obtained by boundary forcing at inlet, as shown in Fig. 2.12. This demonstrates the equivalence between the designed volume forcing and the boundary forcing. The parameters x_c and w of the Gauss distribution have no influence on the FTF results.

The input-output gain σ^2 achieved by this forcing is shown, as a function of Strouhal number, as a blue line in Fig. 2.13. The gain is highest at low Strouhal numbers, with a peak at $St = 0.8$. At the lowest value in our computations, $St = 3 \times 10^{-5}$, the gain is $\sigma^2 = 1.2 \times 10^4$; note that, contrary to the FTF, the definition in Eq. 2.21 does not lead to an expected input-output gain value of unity at zero Strouhal number.

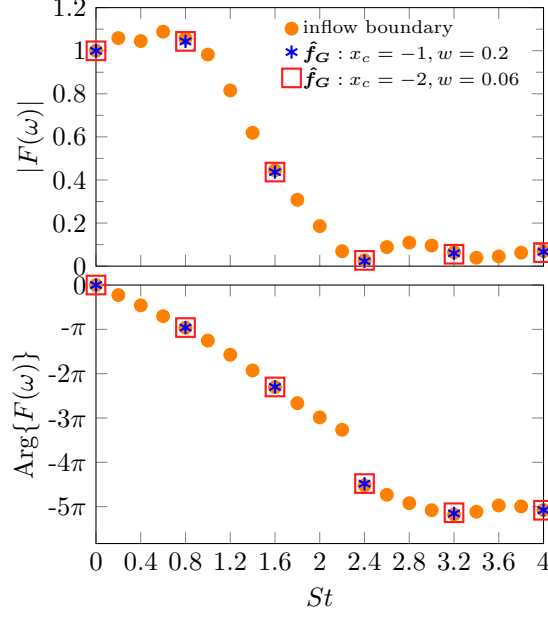


Figure 2.12: FTF obtained through inflow boundary forcing (same as linear-19278 in Fig. 2.8) and through volume forcing \hat{f}_G with $(x_c = -1, w = 0.2)$ and $(x_c = -2, w = 0.06)$. The units of x_c and w are centimeters.

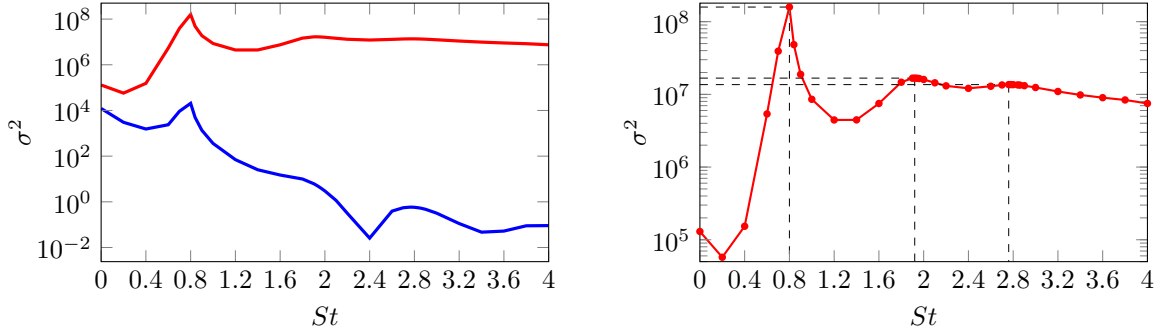


Figure 2.13: Input-output gain σ^2 over frequency, for Gaussian forcing \hat{f}_G (blue line) and for optimal forcing \hat{f}_{opt} (red line). Only \hat{f}_{opt} is shown on the right. The auxiliary lines mark the local maximums of σ^2 .

2.3.5 Receptivity of global heat release rate fluctuations to arbitrary forcing

The input-output gain, as defined in Section 2.3.4.2 for a prescribed volume forcing, can be conveniently evaluated for arbitrary spatial distributions $\hat{\mathbf{f}}$ through the introduction of the flame *receptivity*, as will be shown in this section.

We first define the *resolvent* operator $\mathbf{R}(\omega)$ by inverting the linear system of Eq. (2.18),

$$\hat{\mathbf{q}} = \mathbf{R}(\omega) \mathbf{P} \hat{\mathbf{f}}, \quad \mathbf{R}(\omega) = (i\omega \mathbf{B} - \mathbf{A})^{-1}. \quad (2.23)$$

Note that this inversion is well defined, except in the singular case when ω is an eigenvalue of the system.

The integrated global heat release rate fluctuation, associated with the flame response $\hat{\mathbf{q}}$, is then given by

$$\hat{\Omega}_T = \iint \hat{\omega}_T dx dy = \mathbf{m}_{\Omega}^H \hat{\mathbf{q}}, \quad (2.24)$$

where the vector \mathbf{m}_Ω is constructed from the mesh quadrature coefficients of the volume integral, and from the linearization of local heat release rate according to Eq. (2.39) in the Appendix (of this paper) together with all the linearized progress rates in Eqs. (2.35-2.37). The superscript H denotes the transpose conjugate. With Eqs. (2.23) and (2.24), we find that the global heat release rate fluctuation (a complex scalar) in response to an arbitrary forcing $\hat{\mathbf{f}}$ (a complex vector) is obtained from a scalar product,

$$\hat{\Omega}_T = \mathbf{m}_\Omega^{\text{H}} \mathbf{R} \mathbf{P} \hat{\mathbf{f}} = \mathbf{r}^{\text{H}} \mathbf{M} \hat{\mathbf{f}}. \quad (2.25)$$

We define $\mathbf{r} = \mathbf{M}^{-1} \mathbf{P}^{\text{H}} \mathbf{R}^{\text{H}} \mathbf{m}_\Omega$ as the *receptivity* vector. Note that the receptivity vector depends on the prescribed Strouhal number, as inherited from the resolvent operator, but this dependence is not written in the following for ease of notation. The symmetric matrix \mathbf{M} represents the mesh quadrature for a scalar product $\langle \mathbf{a}, \mathbf{b} \rangle_M = \mathbf{a}^{\text{H}} \mathbf{M} \mathbf{b}$, where \mathbf{a} and \mathbf{b} are complex-valued vectors.

As the global heat release rate amplitude $\hat{\Omega}_T$, in response to any forcing input $\hat{\mathbf{f}}$, is given by the projection of $\hat{\mathbf{f}}$ onto the receptivity \mathbf{r} , any forcing component $\hat{\mathbf{f}}_\perp$ that is perpendicular to \mathbf{r} , $\mathbf{r}^{\text{H}} \mathbf{M} \hat{\mathbf{f}}_\perp = 0$, does not lead to fluctuations of the global heat release rate. Therefore, the maximum input-output gain in the sense of Eq. (2.20) is achieved by forcing that is proportional to \mathbf{r} , $\hat{\mathbf{f}}_{\text{opt}} = \alpha \mathbf{r}$ with $\alpha \in \mathbb{C}$. The gain for this optimal forcing is found to be

$$\sigma_{\text{max}}^2 = \frac{(\mathbf{r}^{\text{H}} \mathbf{M} \alpha \mathbf{r})^2}{(\alpha \mathbf{r})^{\text{H}} \mathbf{M} \alpha \mathbf{r}} = \mathbf{r}^{\text{H}} \mathbf{M} \mathbf{r}, \quad (2.26)$$

the squared norm of the receptivity vector.

In the following application of this receptivity formalism, for a consistent comparison with the FTF calculations in Section 2.3.4, we consider a forcing of the momentum equations, $\hat{\mathbf{f}} = (\hat{f}_u, \hat{f}_v)^{\text{T}}$. For numerical reasons, we allow forcing only in the domain interior, imposing $\hat{\mathbf{f}} = 0$ on all boundaries. The resulting receptivity fields \mathbf{r} (real parts of the x - and y -components) are presented in Fig. 2.11(b,c). It is found that the global heat release rate is receptive to wavy perturbations in the inflow duct, and that the receptivity is particularly high near the flame foot.

The *optimal* input-output gain $\|\mathbf{r}\|^2$ is plotted over frequency in Fig. 2.13 (red line), alongside the gain curve obtained for the non-optimal forcing used in the FTF computations (blue line). A resonance peak can be identified at $St = 0.8$ in the optimal gain.

We hypothesise that this resonance peak is related to an acoustic feedback mechanism, of the intrinsic thermoacoustic (ITA) type: according to Hoeijmakers et al. 2014, 2016, ITA modes may arise when the FTF phase is equal to an odd multiple of π . The frequencies at which this criterion is fulfilled are identified as $St = 0.8$, $St = 2.0$ and $St = 2.94$ from Fig. 2.8. The optimal gain peak at $St = 0.8$ in Fig. 2.13 is therefore fully consistent with the π -criterion. It appears that this peak marks a resonance of the forcing with slightly stable ITA modes of the flame. Two local maxima with smaller amplitudes can also be identified in the optimal gain curve at $St = 1.92$ and $St = 2.76$, which are close to the other two predicted ITA Strouhal numbers.

2.3.6 Resolvent analysis

In Section 4, we used the input-output form of the linear system to define a gain between the norm of a prescribed forcing and the amplitude of the integrated heat release rate in the associated flame response. The result was a relation between an input scalar (the forcing amplitude) and an output scalar (the global heat release rate amplitude). In Section 5, the resolvent operator has been introduced, and it was used to characterize the effect of

arbitrary flow forcing on the integrated heat release rate. The mapping between an input field (the spatially distributed forcing) and an output scalar (the global heat release rate amplitude) involved an inner product of the forcing with the receptivity vector. In this section, a singular value decomposition of the resolvent operator is performed, in order to identify *spatially distributed* oscillation structures in the flame that maximize the response for a given input energy, as introduced in the next paragraph. This will result in a hierarchy of input fields (spatially distributed forcing structures) paired with their associated output fields (spatially distributed response structures) that is particularly useful for reduced-order modelling, and for a discussion of dominant amplification mechanisms in the flame dynamics.

2.3.6.1 Formalism

We set out with the question, which spatial distribution of forcing input $\hat{\mathbf{f}}$ leads to the strongest linear flow response $\hat{\mathbf{q}}$. Norms must be defined,

$$\|\hat{\mathbf{f}}\|^2 = \hat{\mathbf{f}}^H \mathbf{M}_f \hat{\mathbf{f}}, \quad \|\hat{\mathbf{q}}\|^2 = \hat{\mathbf{q}}^H \mathbf{M}_q \hat{\mathbf{q}} \quad (2.27)$$

where \mathbf{M}_f and \mathbf{M}_q are symmetric matrices that contain weight coefficients. Eq. (2.20) represents one special choice for such a norm definition. The matrix \mathbf{M}_f is positive-definite, with dimensions corresponding to the forcing vector $\hat{\mathbf{f}}$. The dimensions of matrix \mathbf{M}_q correspond to that of the response vector $\hat{\mathbf{q}}$, i.e. the total number of degrees of freedom contained in the discretized flow response. Matrix \mathbf{M}_q may be positive semi-definite, in cases where not all flow variables or not the entire flow domain are included in the definition of $\|\hat{\mathbf{q}}\|^2$. In such cases, $\|\hat{\mathbf{q}}\|$ represents a seminorm, which is a valid choice for the resolvent formalism (Garnaud et al. 2013b). The gain between the squared norms of a given forcing and its associated response is found to take the form of a Rayleigh quotient,

$$\sigma^2 = \frac{\|\hat{\mathbf{q}}\|^2}{\|\hat{\mathbf{f}}\|^2} = \frac{\hat{\mathbf{f}}^H \mathbf{P}^H \mathbf{R}^H \mathbf{M}_q \mathbf{R} \mathbf{P} \hat{\mathbf{f}}}{\hat{\mathbf{f}}^H \mathbf{M}_f \hat{\mathbf{f}}}, \quad (2.28)$$

which can be transformed into the generalized eigenvalue problem

$$\mathbf{P}^H \mathbf{R}^H \mathbf{M}_q \mathbf{R} \mathbf{P} \hat{\mathbf{f}} = \sigma^2 \mathbf{M}_f \hat{\mathbf{f}}. \quad (2.29)$$

The operator $\mathbf{P}^H \mathbf{R}^H \mathbf{M}_q \mathbf{R} \mathbf{P}$ is Hermitian, therefore its eigenvectors $\hat{\mathbf{f}}_i$ form an orthogonal set, in the inner-product space defined with the matrix \mathbf{M}_f , and all eigenvalues σ_i^2 are real positive. Let these eigenvalues be numbered in descending order, such that $\sigma_i^2 > \sigma_{i+1}^2$. The *optimal gain* of the forced linear system is then given by σ_1^2 , and it is achieved by the optimal forcing distribution given by the leading eigenvector $\hat{\mathbf{f}}_1$. The associated optimal flow response is named $\hat{\mathbf{q}}_1$. The ensemble of these eigenvalues, forcing and response structures are often called the *resolvent modes* in the recent literature (Schmidt et al. 2018; Towne et al. 2018; Lesshafft et al. 2019). Mathematically, they represent the singular modes of a modified resolvent operator, from which the original resolvent \mathbf{R} can be fully retrieved if all modes are known (see Eq. 11 in Lesshafft et al. 2019), or reduced-order approximations can be constructed from a limited number of dominant modes (Beneddine et al. 2016).

Analogous to the forcing modes $\hat{\mathbf{f}}_i$, the response modes $\hat{\mathbf{q}}_i$ are orthogonal among one another with respect to the inner product matrix \mathbf{M}_q (Schmidt et al. 2018; Towne et al. 2018; Lesshafft et al. 2019), which provides a straightforward interpretation of the role of these modes for the flame dynamics. By construction, the flow is most receptive to the optimal forcing $\hat{\mathbf{f}}_1$, which provokes a response with norm $\|\hat{\mathbf{q}}_1\| = \sigma_1 \|\hat{\mathbf{f}}_1\|$. Within the forcing subspace that is orthogonal to $\hat{\mathbf{f}}_1$, the optimal way to force the flow is with the

Table 2.1: Gain definitions for resolvent analysis.

	norm A	norm B
forcing	$\iint_D (\hat{f}_u ^2 + \hat{f}_v ^2) dx dy$	$\iint_D \hat{f}_{\text{CH}_4} ^2 dx dy$
response	$\iint_D \hat{\omega}_T ^2 dx dy$	$\iint_D \hat{\omega}_T ^2 dx dy$

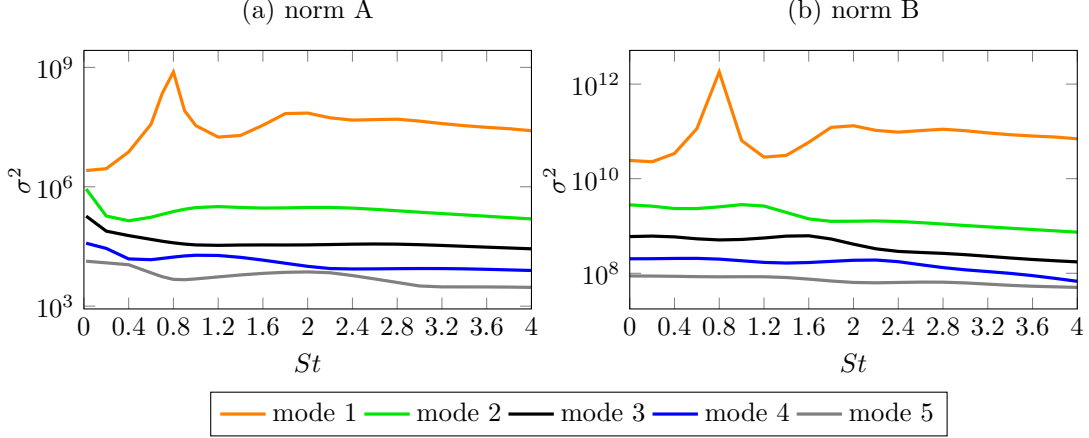


Figure 2.14: Gain versus Strouhal number of the five leading resolvent modes.

spatial structure given by $\hat{\mathbf{f}}_2$, and so forth. If one assumes that all forcing modes are present at equal amplitude in the nonlinear terms (represented by $\hat{\mathbf{f}}$ in Eq. (2.18)), then the corresponding response modes will be found with amplitudes proportional to their gain value, dominated by the optimal mode $\hat{\mathbf{q}}_1$.

For the resolvent analysis, the root-mean-square (rms) amplitude of heat release rate fluctuations is chosen as the (semi-)norm of the flow response, as this provides a meaningful measure of flame unsteadiness. Moreover, it allows to identify a set of optimal and suboptimal modes. Conversely, the global heat release rate takes the form of a rank-1 norm, so it does not allow to obtain more than one mode. Two different definitions are tried for the forcing norm, given in Table 2.1: in the case of norm A, forcing is applied on the right-hand side of the momentum equations, with components \hat{f}_u and \hat{f}_v ; in the case of norm B, the forcing acts on the fuel concentration. In both cases, a standard L2-norm (rms amplitude) of the applied forcing is used.

The eigenvalue problem (Eq. 2.29) is solved using the implicitly restarted Arnoldi method from the ARPACK library. For any given frequency, the resolvent modes with the five highest gain values ($\sigma_1, \dots, \sigma_5$) are computed, with a relative accuracy of 10^{-12} .

2.3.6.2 Dominant dynamics in the forced flame

Gain values σ^2 of the five leading resolvent modes are plotted as functions of frequency in Fig. 2.14 for norms A and B. Overall, it is found that the optimal mode (mode 1) experiences a significantly higher amplification than all subsequent modes, and it can therefore be expected that the optimal response structures will dominate the flame response to arbitrary forcing input. A peak in the optimal gain curve is observed at around $St = 0.8$, suggestive of a resonance mechanism. Following the discussion in Section 2.3.5, we suspect a slightly damped ITA instability mode to exist near this frequency.

The forcing and response structures of mode 1 and mode 2 at $St = 0.8$ are presented in

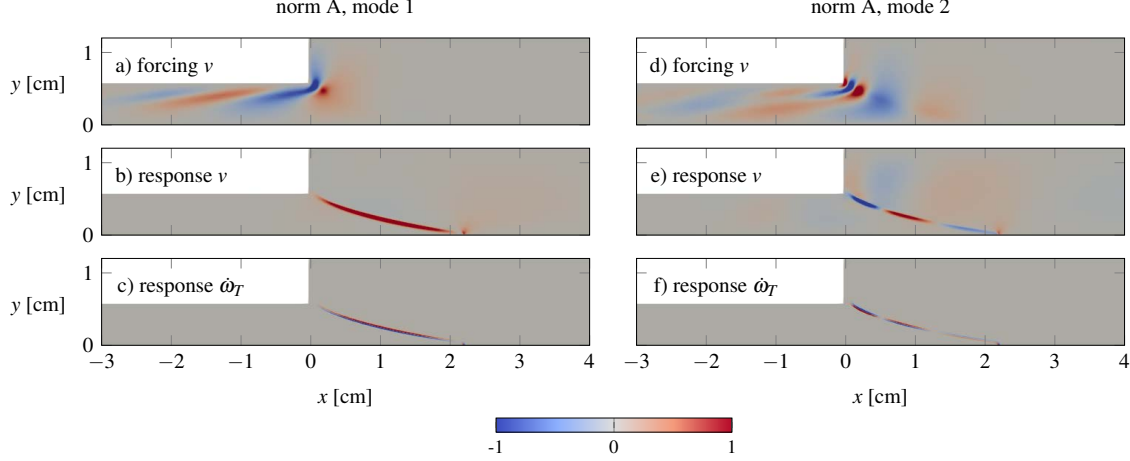


Figure 2.15: Forcing and response structures (real parts) of the two leading resolvent modes at $St = 0.8$, obtained with norm A. All the fields are normalised with their maximum value.

Fig. 2.15 for norm A, and in Fig. 2.16 for norm B. All fields are normalized here with their amplitude maximum for the sake of visualization. Turning first to the optimal resolvent mode obtained for norm A, Fig. 2.15b shows that the response is characterized by strong fluctuations of the transverse velocity v in the flame front. Negative values (blue) denote an inward displacement of the front, positive values (red) denote an outward displacement, consistent with the heat release rate fluctuations in Fig. 2.15c. Note that the real part of \hat{q} merely corresponds to a snapshot of the time-dependent perturbation $\hat{q} \exp(i\omega t)$. When animated in time, the perturbations in the flame front are downstream-travelling waves. The red spot in Fig. 2.15b that emanates from the flame tip is caused by strong fluctuations of thermal expansion, related to heat release rate, in this location.

The response in Figs. 2.15b,c is generated by a forcing input in the form of tilted downstream-travelling waves in the inflow duct, shown in Fig. 2.15a (transverse component). These low-level velocity perturbations are convected by the base flow towards the flame front. The optimality of the tilted forcing structures stems from the fact that perturbations near the centerline are convected faster than those near the wall; the optimal forcing is indeed organized in such a way that it generates velocity fluctuations that reach the flame front with just the right phase, so that they contribute constructively to the travelling wave perturbation of the front position.

An important feature of the flow response in Figs. 2.15b,c is that half a perturbation wavelength extends from the flame foot to the flame tip. This observation is again consistent with the interpretation that the gain peak at $St = 0.8$ arises from a resonance of a stable ITA mode. As evoked at the end of Section 2.3.5, the established criterion for the lowest-frequency ITA mode is an FTF phase lag of π (Hoeijmakers et al. 2014, 2016). This phase lag is related to a time lag τ via the angular frequency, $\omega\tau = \pi$. For the particular case of a slot flame, according to Steinbacher et al. 2019, the time lag τ is given by the propagation time of a downstream-travelling wave along the flame length L_f with convective phase speed c_{ph} . It follows that the wavelength λ of flame front displacement in an ITA mode is related to the flame length as

$$\frac{L_f}{c_{ph}} = \frac{\pi}{\omega} \quad \Rightarrow \quad L_f = \frac{\lambda}{2}. \quad (2.30)$$

By construction, both the response and the forcing fields of mode 2 must be orthogonal to their counterparts of mode 1. In Figs. 2.15e,f, it is seen that the orthogonality in the

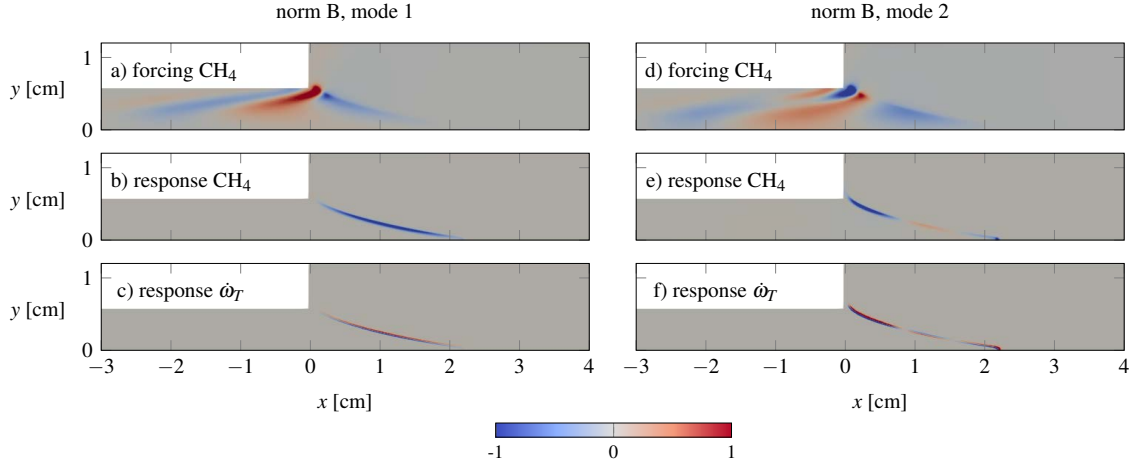


Figure 2.16: Forcing and response structures (real parts) of the two leading resolvent modes at $St = 0.8$, obtained with norm B. All the fields are normalised with their maximum value.

response is underpinned by fitting one additional perturbation wavelength between the flame foot and the tip. As the propagation speed of perturbations along the flame front is imparted by the base flow, and therefore the same for modes 1 and 2, such a response structure can only be achieved by forcing the upstream and downstream parts of the flame front with opposed phase. This phase opposition, between tilted forcing structures near the wall and those near the centerline in the inflow duct, can quite clearly be discerned in Fig. 2.15d. The forcing in this “suboptimal” mode 2 is largely destructive, and, as a consequence, much less efficient than the one of mode 1. Subsequent modes 3, 4 and 5, not shown here, extend the hierarchy of multiple wavelengths along the flame front, and corresponding finer-scale forcing structures inside the duct.

Resolvent modes obtained for the forcing of fuel fluctuations (norm B) are shown in Fig. 2.16, and it can immediately be seen that they contain very similar dynamics as those described for norm A. Tilted fluctuation patterns in the incoming stream are convected by the sheared base flow in such a way that they contribute constructively to one half propagating perturbation wavelength along the flame front in the case of mode 1 (Fig. 2.16a,b,c), whereas they act partially destructively to create one and a half wavelengths in the case of mode 2 (Fig. 2.16d,e,f). Comparison of fluctuations in the CH_4 concentration and in the heat release rate shows that the flame position is shifted outwards in leaner regions, and inwards in richer regions.

It is only at $St = 0.8$ that we find the particular feature of half a wavelength extending along the flame front in the optimal response, linked to the first ITA mode. More generally, the wavelength of perturbations in the flame front continuously decreases with the increase of frequency. The response fields of CH_4 (mode 1, norm B) at $St = 2.0$ and $St = 2.94$ are presented in Fig. 2.17. The snapshot of these responses structures are taken at the moment that a half wavelength of negative (blue) values reaches the flame tip, consistent with the snapshot at $St = 0.8$ in Fig. 2.16b. At these higher frequencies, the perturbation wavelengths are gradually shortened, causing more wave nodes along the front. Consistent with the above discussion of the phase lag between flame foot and flame tip, the particular Strouhal numbers in Fig. 2.17 give rise to 1.5 and 2.5 wavelengths along the flame front.

In conclusion, every forcing that is applied to the linear flame model, for example in the form of nonlinearities in the actual flow, can be projected onto the basis of resolvent modes, which are orthogonal at any given frequency. Due to the strong dominance of the optimal mode gain, seen in Fig. 2.14, the flame response at each frequency is expected to

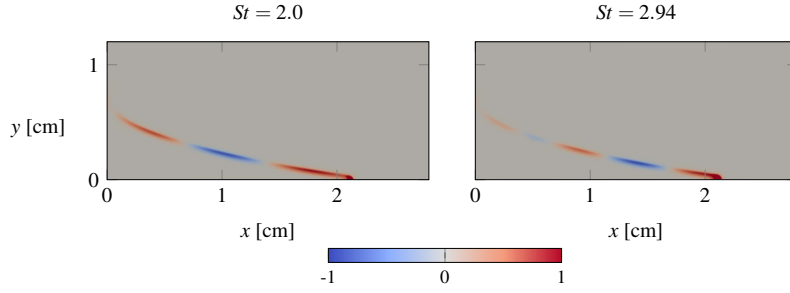


Figure 2.17: Response structures (real parts) of CH₄ at $St = 2.0$ and $St = 2.94$ in mode 1, obtained with norm B. All the fields are normalised with their maximum value.

contain the optimal response as a prevalent structure. In the present configuration, which does not include acoustic chamber resonance, the most amplified frequency of $St = 0.8$ is expected to dominate the spectrum of a stochastically driven flame.

In the present study, isothermal wall conditions are prescribed. However, flame dynamics are known to strongly depend on the wall boundary conditions (Mejia et al. 2015). Resolvent analysis may help characterise the flame response to excitations under different wall boundary conditions, which is a potential direction for future studies.

Linear resolvent analysis, as performed here in order to describe amplification mechanisms in a *laminar* flame configuration, has been shown to provide valid predictions of coherent *turbulent* dynamics in non-reacting shear flows (Beneddine et al. 2016; Semeraro et al. 2016; Schmidt et al. 2018; Towne et al. 2018; Lesshafft et al. 2019; Morra et al. 2019). It is hoped that it will prove similarly useful for the analysis of turbulent flames.

2.3.7 Conclusions

The linear instability dynamics of a premixed slot flame have been investigated, based on the compressible flow equations with a two-step reaction model. As a validation, the linear system of equations was first shown to accurately reproduce the FTF, as obtained from nonlinear timestepping with the AVBP code, at a small fraction of the computational cost.

The linear solver was then used to characterise an input-output gain associated with the FTF, by relating the forcing energy input to the amplitude of the resulting global heat release rate fluctuations. It was demonstrated that upstream flow forcing is energetically particularly efficient at one precise frequency, suggestive of a resonance mechanism. This information could not be obtained from the FTF itself, because the FTF does not include acoustic feedback.

A specific shape of upstream velocity fluctuations is assumed in the FTF computations. Relaxing this restriction, a *receptivity* formalism was introduced, which allows to highlight the flow regions where forcing is particularly efficient in generating global heat release rate fluctuations. The receptivity field depends on the forcing frequency, and it represents itself the optimal spatial distribution of forcing input. A simple projection of any given forcing structure onto the receptivity field yields the modulus and phase of generated global heat release rate fluctuations, in the linear limit of small amplitudes. The optimal gain value, when plotted over frequency, exhibits peaks that coincide with the frequency values predicted by the π -criterion for intrinsic thermoacoustic (ITA) modes (Hoeijmakers et al. 2014, 2016). It appears that the gain peaks found in the receptivity analysis are underpinned by a resonance with stable ITA modes.

Finally, a full resolvent analysis was performed, which yields for each frequency a hierarchy of orthogonal forcing structures, and their associated orthogonal flow response

structures, ranked by their input-output gain. This gain was defined in this analysis as the ratio of rms heat release rate fluctuations over rms forcing input, where the forcing was allowed to act either on the flow velocity (“norm A”) or on the fuel mass fraction (“norm B”). Both types of forcing were found to be most efficient at $St = 0.8$, which is again explained as a resonance with a stable ITA mode. The optimal mode, in both norms, is significantly more efficient than all others, and it contains alone the ITA resonance peaks. A discussion of the obtained forcing/response structures highlighted the importance of constructive interaction of upstream perturbations to support a travelling-wave displacement of the flame front. Due to the shear in the base flow inside the inflow duct, the optimal forcing takes the shape of tilted waves; therefore it will be such structures in the incoming perturbations (velocity or fuel mass fraction) that elicit the strongest flame oscillations. Due to the strong separation between the optimal gain curve and all suboptimal ones, it is expected that the optimal response structures will dominate the flame response to stochastic forcing, with particularly high amplitude at the ITA resonance frequency of $St = 0.8$.

Appendix: linearized equations

The linearized governing equations and their underlying assumptions are presented here. Linearization of Eqs. (2.7-2.10) yields

$$\frac{\partial \rho'}{\partial t} = -\bar{\rho} \frac{\partial u'_j}{\partial x_j} - \bar{u}_j \frac{\partial \rho'}{\partial x_j} - \rho' \frac{\partial \bar{u}_j}{\partial x_j} - u'_j \frac{\partial \bar{\rho}}{\partial x_j}, \quad (2.31)$$

$$\bar{\rho} \frac{\partial u'_i}{\partial t} = -\bar{\rho} \bar{u}_j \frac{\partial u'_i}{\partial x_j} - (\bar{\rho} u'_j + \rho' \bar{u}_j) \frac{\partial \bar{u}_i}{\partial x_j} - \frac{\partial p'}{\partial x_i} + \frac{\partial \tau'_{ij}}{\partial x_j}, \quad (2.32)$$

$$\bar{\rho} \frac{\partial Y'_k}{\partial t} = -\bar{\rho} \bar{u}_j \frac{\partial Y'_k}{\partial x_j} - (\bar{\rho} u'_j + \rho' \bar{u}_j) \frac{\partial \bar{Y}_k}{\partial x_j} + \frac{\partial}{\partial x_j} \left(\bar{D}_k \frac{\partial Y'_k}{\partial x_j} + D'_k \frac{\partial \bar{Y}_k}{\partial x_j} \right) + \dot{\omega}'_k. \quad (2.33)$$

$$\bar{\rho} \frac{\partial}{\partial t} \left(h' - \frac{p'}{\bar{\rho}} \right) = -\bar{\rho} \bar{u}_j \frac{\partial h'}{\partial x_j} - (\bar{\rho} u'_j + \rho' \bar{u}_j) \frac{\partial \bar{h}}{\partial x_j} + \frac{\partial}{\partial x_j} \left(\bar{\alpha} \frac{\partial h'}{\partial x_j} + \alpha' \frac{\partial \bar{h}}{\partial x_j} \right) + \dot{\omega}'_T. \quad (2.34)$$

The linearization of ideal gas law gives $\frac{T'}{T} = -\frac{\rho'}{\bar{\rho}} + \frac{p'}{\bar{p}}$. The fluctuation of sensible enthalpy given as $h' = \bar{c}_p T' + \sum_k Y'_k \bar{c}_{p,k}$ in (Meindl et al. 2021) is simplified to $h' = \bar{c}_p T'$. The contribution of $\sum_k Y'_k \bar{c}_{p,k}$ is neglected, because $\bar{c}_{p,k}$ has similar values for all species k and $\sum_k Y'_k = 0$. The latter allows us to remove the species transport equation tracking H_2O , because $Y'_{\text{H}_2\text{O}}$ then becomes a passive scalar, only involved in its own transport equation but not in the enthalpy equation. We have checked that involving or not the transport equation of H_2O has negligible effect on the calculation of FTF. Knowing that N_2 is another passive scalar that does not react, we finally reduce to four species transport equations tracking CH_4 , O_2 , CO_2 and CO .

The fluctuation of molecular viscosity writes $\mu' = b \bar{\mu} \frac{T'}{T}$. As constant Schmidt and Prandtl numbers are assumed, the fluctuation of other transport coefficients writes $D'_k = \frac{\mu'}{\bar{\mu}} \bar{D}_k$ and $\alpha' = \frac{\mu'}{\bar{\mu}} \bar{\alpha}$. The fluctuation of molecular stress tensor writes $\tau'_{ij} = -\frac{2\bar{\mu}}{3} \frac{\partial u'_k}{\partial x_k} \delta_{ij} + \mu' \left(\frac{\partial \bar{u}_i}{\partial x_j} + \frac{\partial \bar{u}_j}{\partial x_i} \right)$.

The perturbation of progress rate \mathcal{Q}'_1 writes

$$\mathcal{Q}'_1 = \bar{\mathcal{Q}}_1 \left((n_{1,\text{CH}_4} + n_{1,\text{O}_2}) \frac{\rho'}{\bar{\rho}} + \frac{T_{a,1} T'}{\bar{T}^2} + n_{1,\text{O}_2} \frac{Y'_{\text{O}_2}}{\bar{Y}_{\text{O}_2}} + n_{1,\text{CH}_4} \frac{Y'_{\text{CH}_4}}{\bar{Y}_{\text{CH}_4}} \right). \quad (2.35)$$

If we denote the progress rate of second reaction as $\mathcal{Q}_2 = \mathcal{Q}_{f,2} - \mathcal{Q}_{r,2}$ where $\mathcal{Q}_{f,2} = \kappa_{f,2}[X_{\text{CO}}]^{n_{2,\text{CO}}}[X_{\text{O}_2}]^{n_{2,\text{O}_2}}$ and $\mathcal{Q}_{r,2} = \kappa_{r,2}[X_{\text{CO}_2}]^{n_{2,\text{CO}_2}}$, we have $\mathcal{Q}'_2 = \mathcal{Q}'_{f,2} - \mathcal{Q}'_{r,2}$, where

$$\mathcal{Q}'_{f,2} = \bar{\mathcal{Q}}_{f,2} \left((n_{2,\text{CO}} + n_{2,\text{O}_2}) \frac{\rho'}{\bar{\rho}} + \frac{T_{a,2} T'}{\bar{T}^2} + n_{2,\text{O}_2} \frac{Y'_{\text{O}_2}}{\bar{Y}_{\text{O}_2}} + n_{2,\text{CO}} \frac{Y'_{\text{CO}}}{\bar{Y}_{\text{CO}}} \right), \quad (2.36)$$

$$\mathcal{Q}'_{r,2} = \bar{\mathcal{Q}}_{r,2} \left(n_{2,\text{CO}_2} \frac{\rho'}{\bar{\rho}} + n_{2,\text{CO}_2} \frac{Y'_{\text{CO}_2}}{\bar{Y}_{\text{CO}_2}} \right). \quad (2.37)$$

The perturbation of $\kappa_{r,2} = \frac{\kappa_{f,2}}{K}$ is not considered in this work for simplicity. The perturbation of correction functions $f_j(\phi)$ is neglected, because lean premixed flame has $f_j(\phi) \approx 1$ homogeneously in the whole domain. The perturbation of reaction rate and heat release rate write

$$\dot{\omega}'_k = W_k \sum_{j=1}^M \nu_{kj} \mathcal{Q}'_j, \quad (2.38)$$

$$\dot{\omega}'_T = - \sum_{j=1}^M \Delta h_{f,j}^o \mathcal{Q}'_j. \quad (2.39)$$

A similar numerical treatment as Avdonin et al. 2019; Meindl et al. 2021 is applied for $\frac{Y'_{\text{CH}_4}}{\bar{Y}_{\text{CH}_4}}$ to avoid division by zero in \bar{Y}_{CH_4} which may occur from nonlinear calculation or interpolation. We choose ϵ to be 5% of the maximum value of CH_4 such that the fraction becomes $\frac{Y'_{\text{CH}_4}}{\bar{Y}_{\text{CH}_4} + \epsilon}$. The robustness of ϵ is verified: tuning ϵ from 5% to 15% changes around 2% in the gain of flame transfer function. A more dedicated description of linearized chemical scheme is presented in the Appendix B of Meindl et al. 2021.

Acknowledgements

The authors thank the CFD group at CERFACS for providing us with their code AVBP. In this context the authors acknowledge especially the hands on help of Gabriel Staffelbach. The authors furthermore gratefully acknowledge Laurent Gicquel, Benedicte Cuenot and Franck Nicoud for fruitful discussions. Chuhan Wang is supported through a scholarship by Ecole polytechnique. The authors gratefully acknowledge the Deutsche Forschungsgemeinschaft (DFG) for funding this work within the project 441269395. The authors gratefully acknowledge the Gauss Centre for Supercomputing e.V. (www.gauss-centre.eu) for funding this project by providing computing time on the GCS Supercomputer SuperMUC-NG at Leibniz Supercomputing Centre (www.lrz.de).

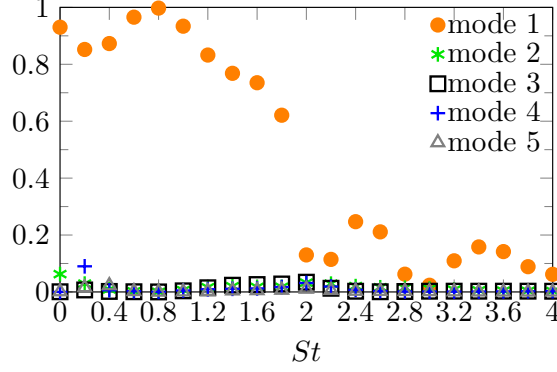


Figure 2.18: Projection of response to inflow forcing onto the resolvent response modes. For the resolvent analysis, the forcing norm is the root-mean-square of velocity forcing in the momentum equations (same as norm A), the response norm is the root-mean-square of velocity fluctuations in the flow response.

2.4 Further discussions

2.4.1 Projection on the basis of resolvent modes

We make an attempt to understand how efficiently the inflow forcing is able to excite optimal responses. This is done by projecting the response onto inflow forcing on the optimal response basis obtained from the resolvent analysis. The resolvent analysis provides an orthogonal basis for flame response, ordered by their importance, namely their *observability* in the flame dynamics. By projection, we can understand how the response to inflow forcing is in alignment with optimal response modes.

The response to inflow forcing is projected onto the resolvent response basis calculated with respect to velocity forcing and response. The complex-number projection coefficients of the five leading modes are computed, and the square of their absolute values is shown as functions of Strouhal number in Fig. 2.18. At $St = 0.8$, the projection on the optimal response (mode 1) almost reaches 1. This can be already implied by the strong gain separation at resonance peak at $St = 0.8$. In other words, the inflow forcing leads to a flame response bearing a close resemblance to that induced by the optimal forcing structure as expected.

There is a significant drop of projection coefficients of the optimal mode beyond $St = 2$. We have not found a firm argument to explain this drop of resemblance, but it may be related to the phase jump at around $St = 2.2$ in the FTF phase.

This projection calculation shows that the structures of the response to inflow boundary and optimal volume forcing at the resonance frequency are very similar, as may have been expected, but this information can already be predicted from the gain separation in resolvent gain curves.

2.4.2 Sensitivity to numerical domain length

The numerical domain length is found to have a negligible effect on the results. More concretely, we extend the outlet position $x_{end} = 10$ cm to $x_{end} = 15$ cm, as shown in Fig. 2.19. We then calculate the FTF from the extended base flow at a few frequencies. The result closely matches the FTF of the non-extended base flow, as shown in Fig. 2.20. Hence, the upstream and downstream boundary conditions can be considered to be appropriately transparent.

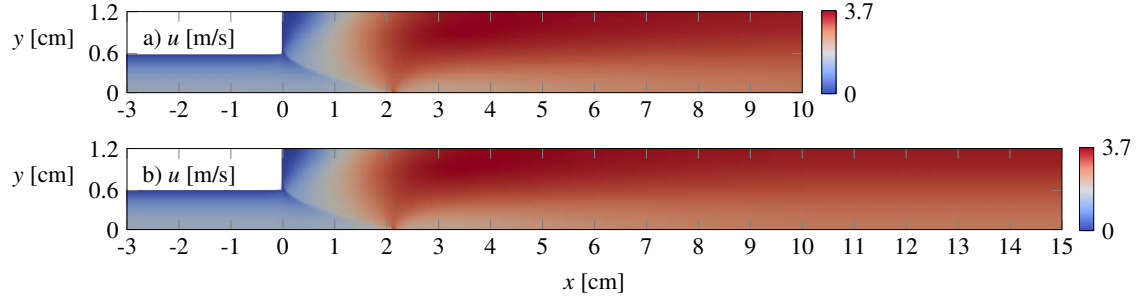


Figure 2.19: Base flow streamwise velocity u of the non-extended domain $x_{end} = 10$ cm and the extended domain $x_{end} = 15$ cm.

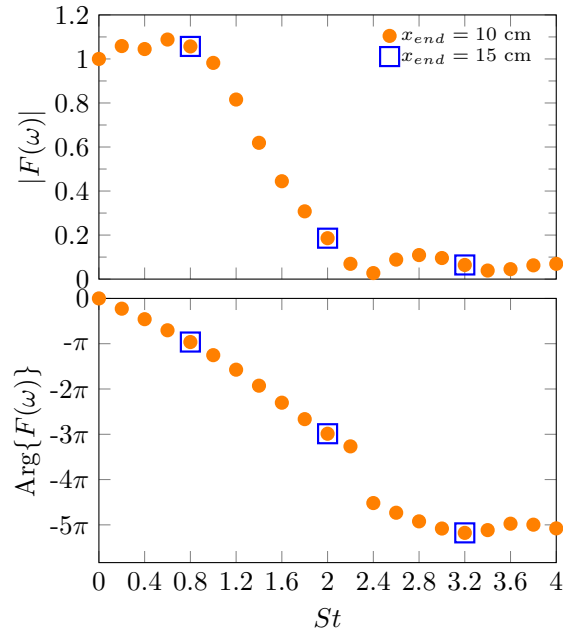


Figure 2.20: FTF of the extended ($x_{end} = 15$ cm) and non-extended ($x_{end} = 10$ cm) domain.

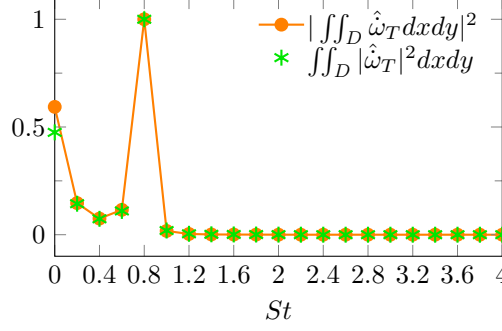


Figure 2.21: Evaluation of response norms for the flat Gaussian forcing at $x_c = -1$ cm. The norm values are normalised by their maximum at $St = 0.8$, respectively.

2.4.3 Choice of response norms

In §2.3.4.2 and §2.3.5, the response norm is taken as the global heat release rate $\hat{\Omega}_T^2 = |\int\int_D \hat{\omega}_T dxdy|^2$, consistent with the FTF. According to Eq. (2.24), the square of the global heat release rate is

$$\hat{\Omega}_T^2 = \hat{q}^H m_\Omega m_\Omega^H \hat{q}, \quad (2.40)$$

which is a rank-1 norm that does not allow to identify more than *one* forcing mode.

In §2.3.6, the response norm is taken as the root-mean-square of the heat release rate $\int\int_D |\hat{\omega}_T|^2 dxdy$. The dimension of this norm is equal to the degrees of freedom of all the fluctuation variables in the heat release rate fluctuation of Eq. (2.39), which allows to identify *a set of* optimal and suboptimal forcing.

To investigate the impact of the choice of norm on the input-output gain, both heat release rate norms are evaluated in the flame response to the Gaussian forcing at different frequencies. After normalisation by their maximum value at $St = 0.8$, respectively, both norms give nearly identical results, as presented in Figure 2.21.

2.4.4 Eigenmodes of the flame

The eigenmodes of the slot flame are calculated from the steady base state. The result is shown in Fig. 2.22. All the eigenvalues are found to be stable with negative linear temporal growth rates, consistent with the nonlinear calculation converging to a steady state. Several branches of decaying linear growth rates with Strouhal numbers are identified. The shapes of velocity fluctuations are highly concentrated near the downstream outlet of the computational domain for all the eigenmodes present in the spectrum. There is no strong indication of an ITA mode at $St = 0.8$. It is probable that the stable ITA mode is strongly damped, and can only be observed in a forcing scenario.

2.4.5 Orr-mechanism

The structures of optimal forcing observed here bear a close resemblance with the Orr-mechanism. The optimal forcing structures are oriented 45° against the shear along the wall channel. But actually we have not found a strong sign of energy amplification due to the Orr-mechanism. During the time that these tilted structures are convected downstream, we find that the amplitude growth that accompanies the upright-tilting is insignificant for the gain. The reason that these tilted structures are the optimal is that they need to impact the flame in the right phase to contribute to the same traveling waves. We conclude

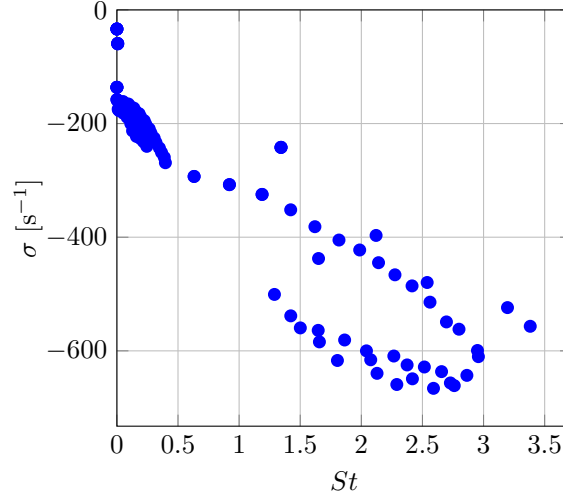


Figure 2.22: Eigenmodes of the slot flame. σ here represents the linear temporal growth rate.

that the Orr mechanism has no strong effect in this flame, and it could be a coincidence that the forcing structures also correspond to an Orr-type perturbation.

2.4.6 Impact of flame attachment

It is important to note that the flame attachment boundary condition has a decisive influence on the flame dynamics and global heat release dynamics (see Sec 11.2.2 of (Lieuwen 2021)). For a spatially uniform disturbance field, if a flame base is allowed to move, no change in the shape of flame surface is expected when the velocity of flame base movement is the same as the velocity disturbances. Whereas in our case, the flame base is anchored to the boundary and the harmonic disturbances originating at the boundary travel along the flame surface, leading to flame wrinkling.

CHAPTER 3

Modal analysis of a bluff body stabilised flame

The instability of a bluff body stabilized flame that acts as an oscillator is investigated. Different from the previous chapter, the oscillator behavior depends on the flow system itself, and no external forcing is introduced. Hence we use modal analysis to investigate this oscillator. A paper submitted to *Journal of Fluid Mechanics* is presented (Wang et al. 2022b), including context of the study, methods, results and discussions.

Contents

3.1	Introduction	44
3.2	Methods	47
3.2.1	Nonlinear governing equations	47
3.2.2	Calculation of base flow and mean flow	48
3.2.3	Global linear analysis	49
3.3	Non-reacting flow	49
3.4	Reacting flow: studies on the steady base state	51
3.4.1	Global modes in base flow	51
3.4.2	Wavemaker analysis	53
3.4.3	Influence of reaction on the base flow	55
3.5	Reacting flow: mean flow analysis	56
3.6	Conclusions	57

Global linear stability of a cylinder anchored flame

Chuhan Wang¹, Lutz Lesshafft¹, Kilian Oberleithner²

¹Laboratoire d’Hydrodynamique, CNRS / Ecole Polytechnique / Institut Polytechnique de Paris, Palaiseau, France

²Laboratory for Flow Instabilities and Dynamics, Technische Universität Berlin, Berlin, Germany

Submitted 04 March 2022

Abstract

The linear stability of a laminar premixed flame, anchored on a square cylinder at $Re = 500$ and confined inside a channel, is investigated via global eigenmode analysis, based on the reacting flow equations with a one-step chemistry scheme. While the flow is unstable in the absence of reaction, flame ignition leads to a stabilisation, as long as the wall temperature of the cylinder is sufficiently low. When the mean flow fields, obtained from nonlinear timestepping, are taken as the basic state for the linear analysis, the leading eigenvalue accurately matches the oscillation frequency observed in the simulation. The “wavemaker” region that controls the global flow dynamics is localised in the shear layer at the rear of the recirculation zone, where the stability or instability results from the balance of shear-derived production and downstream convection of momentum perturbations. It is concluded that instability in this configuration arises from hydrodynamic effects, not fundamentally different from the non-reacting flow case, although the critical parameters and the oscillation frequency are strongly modified by the presence of the flame. This influence is attributed to the significant changes in the base flow, principally due to thermal expansion.

Keywords— global mode, combustion instability, shear instability, premixed laminar flame

3.1 Introduction

Bluff-body burners are of particular interest for flame anchoring in a high-velocity flow. The body generates a recirculation zone in its near wake, keeping the flame at a fixed position and preventing blow-off. Flames anchored to bluff bodies have been extensively studied experimentally and numerically (Williams et al. 1948; Chen et al. 1990; Dally et al. 1998; Shanbhogue et al. 2009a; Ghani et al. 2015). However, vortex shedding may occur in bluff body wakes, which drastically affects the flame dynamics and may even trigger thermoacoustic instability (Manoharan and Hemchandra 2015; Oberleithner et al. 2015a; Emerson et al. 2016). It is therefore important to analyse the physical mechanisms that underpin these oscillations, which can then be targeted for an efficient control. In the field of non-reacting flow, vortex shedding in cylinder wakes is a standard benchmark for stability calculations. The linear stage of oscillation onset in such non-reacting wakes has been rather fully explained within the framework of eigenmode analysis (Noack and Eckelmann 1994; Pier 2002; Theofilis 2003; Barkley 2006; Taira et al. 2020). In the presence

of a flame, however, chemical reaction and associated heat release may strongly change the instability dynamics. The objective of this study is to characterise how the presence of a flame in a square cylinder wake, through the effects of chemical reaction and heat release, changes the instability dynamics. To this purpose, a linear eigenmode analysis will be based on the governing equations for a simple reacting flow; the topic of mean flow versus steady flow as base states, as well as “wavemaker” concepts, will be revisited in this context.

Linear stability analysis characterises the self-excited behaviour of a flow, by calculating the temporal eigenmodes of the linearised governing equations. Conventionally, the real part of complex eigenvalues denotes the growth rate, and the imaginary part denotes the frequency of flow perturbations. Pier 2002 and Barkley 2006 performed linear stability analysis of the base flow and mean flow of a two-dimensional cylinder wake. Here, the *base* flow refers to a steady solution of the flow equations, and the *mean* flow refers to the temporal average of the oscillating flow state. The least stable eigenmode of the base flow fails to capture the shedding frequency at supercritical Reynolds numbers, whereas the corresponding eigenmode of the mean flow gives excellent predictions. The growth rate of the least stable mean flow eigenmode was found to be almost exactly zero. Similar observations have been made in many other flow cases, prompting the postulation of a “real-zero-imaginary-frequency” (RZIF) criterion (Turton et al. 2015; Bengana and Tuckerman 2021), which states that perturbations inducing mean flow modifications saturate when the mean flow becomes neutrally stable. Making use of this criterion, Mantič-Lugo et al. 2014 proposed a self-consistent model to predict the frequency and amplitude of vortex shedding without prior knowledge of the mean flow.

With the added complexity of reaction, flame instability may arise from the inherent coupling among various physical mechanisms, including thermoacoustic effects. The classical thermoacoustic instability refers to a scenario where the flame acts as a frequency-selective amplifier of perturbations, and a surrounding structure acts as an acoustic resonator. Recently, a distinct scenario of “intrinsic thermoacoustic instability” has also been explored (Hoeijmakers et al. 2014; Emmert et al. 2015; Courtine et al. 2015), where the acoustic chamber resonance is replaced with an acoustic-hydrodynamic coupling in the upstream system to close the feedback loop. Hydrodynamic instability of a flame, in the literature, may denote at least two distinct concepts: on the one hand, the term is used to refer to instability dynamics that are intrinsic to the flame dynamics itself, without involving any acoustic resonance, such as the Darrieus-Landau and the thermo-diffusive instability mechanisms (Matalon 2007); on the other hand, it is also used to denote instability of the supporting flow field when unsteady reaction dynamics, although present, are not accounted for. Examples for the latter approach include studies of vortex shedding in bluff body anchored flames (Emerson et al. 2016), shear layer instability (Oberleithner et al. 2015a), the precessing vortex core in swirling flames (Oberleithner et al. 2015b), the coherent structures in turbulent jet flames (Kaiser et al. 2019a; Casel et al. 2022), and inertial waves (Albayrak et al. 2019; Müller et al. 2022). The justification of this approach relies on the *a priori* hypothesis that unsteady reaction does not play an active role in the instability mechanism, therefore it is commonly referred to as the “passive flame” approach (Casel et al. 2022).

In reality however, flame unsteadiness involves a large number of physical processes that may combine to form instability mechanisms. On conceptual grounds, many of these can be either neglected or simplified for a fundamental analysis; in the present context, we choose to regard the low Mach number limit in order to reduce the complexity of compressibility, and we opt for a one-step chemical reaction model that retains much of the specificity of combustion, without overstressing the fuel dependency.

Bluff bodies of different shapes are used to fix the flame position in various com-

bustion configurations, *e.g.* in propulsion applications, afterburners being one example (Shanbhogue et al. 2009a). The basic scenario is a premixed reactant flow passing around a bluff body, which is ignited in the recirculation region that contains heated reaction products. Fundamental studies of flame dynamics in such a case cover a wide range of topics, such as the near-wall anchoring structures (Kedia and Ghoniem 2014; Miguel-Brebion et al. 2016), the onset of flame blow-off (Nair and Lieuwen 2007; Chaudhuri et al. 2012; Kedia and Ghoniem 2015; Vance et al. 2021), the forcing response (Shanbhogue et al. 2009b; Shin et al. 2011; Shin and Lieuwen 2013), the acoustic flame transfer function (Mejia et al. 2018; Kaiser et al. 2019b) and the effect of premixed flow properties including gas composition (Kim et al. 2019; Balasubramanian et al. 2021) and preheated temperature (Erickson and Soteriou 2011; Michaels et al. 2017) on flame dynamics and structures. Closely related to our present investigation are studies of the effect of reactant density ratio on the hydrodynamic instability of bluff body flames (Emerson et al. 2012; Emerson and Lieuwen 2015; Suresha et al. 2016; Emerson et al. 2016). At different preheated reactant temperatures, these authors conducted local stability analysis on experimental velocity and density profiles. A transition from convective to absolute instability was found to occur for preheated lighter unburnt gas when the density ratio between unburnt/burnt gas is close to unity. The authors also estimated the global mode shapes by combining local stability results (Juniper and Pier 2015), for the goal of identifying flow regions related to strong eigenvalue sensitivity (Emerson et al. 2016). The latter is also one of the objectives in the present paper, with an alternative strategy.

We conduct a global linear stability analysis of a two-dimensional premixed laminar flame anchored on a square cylinder. The Navier–Stokes equations for reacting flow are linearised around the steady and mean states, and both the streamwise and cross-stream directions are resolved. Similar approaches have been carried out in recent years for premixed laminar flames. The closest to our study is the analysis by Avdonin et al. 2019, who computed the global instability eigenmode of a slot flame in an anechoic chamber, identified as the intrinsic thermoacoustic mode. Those authors also used linearised approaches to calculate flame transfer functions and entropy wave transfer functions (Albayrak et al. 2018; Meindl et al. 2021). The linear dynamics of M-shaped flames was investigated in a similar framework by Blanchard et al. 2015, 2016, who focused on the input-output behaviour of the flame, including impulse response and pressure wave generation. Their studies were extended to M-shaped swirling flames by Skene and Schmid 2019. In a recent study, we used resolvent analysis to identify the optimal forcing structures in a slot flame, leading to maximal heat release (Wang et al. 2022a). For linear analysis of diffusion jet flames, one may refer to Nichols and Schmid 2008, Qadri et al. 2015, Moreno-Boza et al. 2016, Qadri et al. 2021, Sayadi and Schmid 2021. Modal analysis has also been conducted for hot jets (Coenen et al. 2017; Chakravarthy et al. 2018) and in turbulent swirling flames with the presence of precessing vortex core (Oberleithner et al. 2015a,b).

The reference case of the present study is taken from Kedia and Ghoniem 2014, 2015, where the authors conducted direct numerical simulations (DNS) of a premixed laminar flame anchored on a solid square cylinder inside a channel at $Re = 500$. The governing equations for those simulations were formulated in the low-Mach number limit, and a detailed methane-air reaction scheme of 16 species and 46 steps was implemented. A solid-fluid conjugated heat exchange model was included. Kedia and Ghoniem 2014 found that the non-reacting cold flow displayed vortex shedding, whereas the ignited reacting flow was steady, anchoring at a position immediately downstream of the square. The objective of our work is to use global linear analysis to study the inherent instability mechanism of this flame. We use the same geometry and the same flow parameters as Kedia and Ghoniem 2014, as far as possible within our physical approximations.

The paper is organized as follows. In §3.2, the governing equations and the geometry of the flow configuration are documented. In §3.3, nonlinear timestepping and linear analysis of an unstable non-reacting mean flow is carried out. In §3.4, base flow analysis of the reacting flow with different cylinder temperatures is conducted. A detailed wavemaker analysis is attempted in order to identify which terms contribute, and where, to the leading instability eigenmode. In §3.5, we perform nonlinear timestepping of a slightly unstable flame, alongside a modal analysis of the reacting mean flow. Conclusions and perspectives are given in §3.6.

3.2 Methods

3.2.1 Nonlinear governing equations

The governing equations for reacting flow are formulated in the low Mach number limit (McMurtry et al. 1986), in terms of primitive variables $(\rho, u_x, u_y, h, Y_{\text{CH}_4})$ in Cartesian coordinates (x, y) , where (u_x, u_y) are the streamwise and cross-stream velocity components, ρ is the density, h is the sensible enthalpy and Y_{CH_4} is the mass fraction of methane. The chemical reaction is modelled by a global one-step scheme for a lean methane-air mixture, requiring only one species equation for CH_4 . Each flow variable in the compressible reacting flow equations is expanded in orders of Mach number (McMurtry et al. 1986), and following notations in Albayrak et al. 2018, these equations are written in the form

$$\frac{\partial \rho}{\partial t} = -\frac{\partial}{\partial x_j}(\rho u_j), \quad (3.1)$$

$$\rho \frac{\partial u_i}{\partial t} = -\rho u_i \frac{\partial u_j}{\partial x_j} - \frac{\partial p}{\partial x_i} + \frac{\partial \tau_{ij}}{\partial x_j}, \quad (3.2)$$

$$\rho \frac{\partial Y_{\text{CH}_4}}{\partial t} = -\rho u_j \frac{\partial Y_{\text{CH}_4}}{\partial x_j} - \frac{\partial J_j}{\partial x_j} + \dot{\omega}_{\text{CH}_4}, \quad (3.3)$$

$$\rho \frac{\partial h}{\partial t} = -\rho u_j \frac{\partial h}{\partial x_j} - \frac{\partial q_j}{\partial x_j} + \dot{\omega}_T. \quad (3.4)$$

The system is closed by the equation of state for an ideal gas

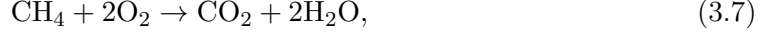
$$p_0 = R_s \rho T. \quad (3.5)$$

The pressure p_0 in the equation of state (3.5) is at the zeroth order of expansion, i.e. independent of Mach number, whereas p in the momentum equation (3.2) is its first-order complement. The molecular stress tensor is given by $\tau_{ij} = -\frac{2\mu}{3} \frac{\partial u_k}{\partial x_k} \delta_{ij} + \mu \left(\frac{\partial u_i}{\partial x_j} + \frac{\partial u_j}{\partial x_i} \right)$, where the molecular viscosity μ is assumed to be constant here. The flux of species transport and heat transfer are modelled as $J_j = -D_s \frac{\partial Y_{\text{CH}_4}}{\partial x_j}$ and $q_j = -\alpha \frac{\partial h}{\partial x_j}$, respectively. The transport coefficients therein are associated with a Schmidt number $\text{Sc} = \frac{\mu}{D_s}$ and a Prandtl number $\text{Pr} = \frac{\mu}{\alpha}$. Constant values $\text{Sc} = 0.7$ and $\text{Pr} = 0.7$ are prescribed in this study, which are valid for a lean methane-air mixture (Sato 1982). R_s in the equation of state is the specific gas constant. In the following, the enthalpy is expressed as $h = C_p T$, where the specific heat capacity C_p is taken to be constant. Combining this definition of enthalpy with (3.1, 3.4, 3.5), we can eliminate the time derivative term in (3.4) and replace it by

$$0 = \rho \frac{\partial u_i}{\partial x_i} + \alpha \rho \frac{\partial}{\partial x_i} \left(\rho^{-2} \frac{\partial \rho}{\partial x_i} \right) + \frac{\rho R_s}{C_p p_0} \dot{\omega}_T, \quad (3.6)$$

in the same way as Kaiser et al. 2019a. The system for the following calculations is then given by (3.1-3.3,3.6).

The reaction rate is modelled by a one-step chemistry scheme,



where the reaction progress rate \mathcal{Q} is given in the form of an Arrhenius law

$$\mathcal{Q} = [\text{X}_{\text{CH}_4}]^{n_{\text{CH}_4}} [\text{X}_{\text{O}_2}]^{n_{\text{O}_2}} T^\beta \exp\left(-\frac{T_a}{T}\right). \quad (3.8)$$

Coefficients for the model constants n_{CH_4} , n_{O_2} , β and T_a are taken from the scheme 1S_CH4_MP1 provided by CERFACS 2017, which is suitable for a lean premixed methane-air gas. The molar concentration of CH_4 and O_2 are given by $[\text{X}_{\text{CH}_4}] = \rho \frac{Y_{\text{CH}_4}}{W_{\text{CH}_4}}$ and $[\text{X}_{\text{O}_2}] = \rho \frac{Y_{\text{O}_2}}{W_{\text{O}_2}}$, respectively, where W_{CH_4} and W_{O_2} denote their molecular mass. The reaction rate in the species equation is given by $\dot{\omega}_{\text{CH}_4} = -W_{\text{CH}_4} \mathcal{Q}$, and the heat release due to combustion in the enthalpy equation is given by $\dot{\omega}_T = -\Delta h_f^o \mathcal{Q}$, where Δh_f^o is the standard enthalpy of reaction.

3.2.2 Calculation of base flow and mean flow

The geometry of the numerical domain, presented in figure 3.1, corresponds to the simulations of Kedia and Ghoniem 2014, 2015 with a square cylinder of side length $D = 5$ mm centred in a channel 25 mm wide. The numerical domain extends $2D$ upstream and $9D$ downstream of the cylinder. Inflow conditions for streamwise velocity, temperature and equivalence ratio are set as

$$U = 1.6 \frac{\text{m}}{\text{s}}, \quad T_0 = 300 \text{ K}, \quad \phi = 0.7, \quad (3.9)$$

which leads to an inflow Reynolds number $\text{Re} = \rho_0 U D / \mu_0 = 500$, where ρ_0 and μ_0 denote the density and the dynamic viscosity at the inflow, respectively. The inlet velocity profile is prescribed as being parabolic, and a no-slip adiabatic condition is used at the channel walls. A no-slip condition is also prescribed on the cylinder surface, but an important difference with respect to the reference experiments is that we prescribe a constant temperature of the cylinder, T_c . Such an isothermal condition is of practical interest in the light of recent studies on the effect of flame holder temperature on the flame dynamics (Miguel-Brebion et al. 2016; Mejia et al. 2018; Cheng et al. 2021).

The nonlinear governing equations are discretised on the unstructured mesh shown in figure 3.1 with a continuous Galerkin method, as provided by the FEniCS software (Alnæs et al. 2015). The mesh contains 41 145 triangular cells, with high spatial resolution in the flame front region.

A steady flow solution is obtained by Newton's iterative method; such a steady state will be denoted a "base flow" in the following. Convergence of Newton's method is conditioned on the initial guess, which must be sufficiently close to the solution. In particular, it is difficult to displace a sharp flame front during the iterations, but much less difficult to successively steepen an initially diffuse front. An adapted approach, which was used to calculate the steady solution of slot flames (Albayrak et al. 2018; Douglas 2021), is applied in the present case. All diffusion coefficients are multiplied by an artificial parameter α , and the heat release term is multiplied by a parameter β . We first enlarge the convergence radius by computing a very viscous non-reacting flow as the initial guess. To this end, α is set to 30 and β is set to 0. Then we gradually decrease α from 30 to 1, and at the same time we increase β from 0 to 1. Each time α and β are changed, one Newton iteration is

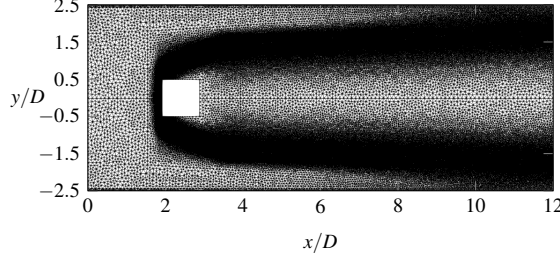


Figure 3.1: Unstructured mesh of the numerical domain. Lengths are normalised with the square width $D = 5$ mm.

performed, until both factors are brought to 1. The final base flow is thus recovered with residual errors on the order of machine precision, after around 25 iteration steps.

To obtain the time-averaged flow fields in unstable configurations, the nonlinear reacting flow equations are integrated in time with a Crank-Nicolson scheme. Averaging is started when the periodic regime is reached. Such time-averaged fields will be called the “mean flow” throughout this study.

3.2.3 Global linear analysis

Flow fluctuations $\mathbf{q}'(\mathbf{x}, t)$ around the steady base state or around the time-averaged mean state are assumed to be governed by the linear equation

$$\mathbf{B} \frac{\partial \mathbf{q}'}{\partial t} = \mathbf{A} \mathbf{q}', \quad (3.10)$$

where the matrices \mathbf{B} and \mathbf{A} are built from linearisation of (3.1-3.3,3.6). This linear assumption is valid for infinitesimally small fluctuations around the base state, and it is hoped to be extendable to finite-amplitude fluctuations around the mean flow in supercritical conditions (Barkley 2006; Mantič-Lugo et al. 2014). The linearisation of the governing equations is performed symbolically within FEniCS by use of the Unified Form Language (Alnæs et al. 2014). The flow fluctuations $\mathbf{q}'(\mathbf{x}, t)$ can be expanded in the basis of eigenmodes $\mathbf{q}'_j(\mathbf{x}, t) = \boldsymbol{\phi}_j(\mathbf{x}) \exp(\lambda_j t)$ obtained from the generalised eigenvalue problem

$$\lambda_j \mathbf{B} \boldsymbol{\phi}_j = \mathbf{A} \boldsymbol{\phi}_j. \quad (3.11)$$

The eigenvalues λ_j and associated eigenvectors $\boldsymbol{\phi}_j$ are computed with a Krylov method. We define the frequency as $f_j = -\text{Im}[\lambda_j]$ and the growth rate as $\sigma_j = \text{Re}[\lambda_j]$, so that $\lambda_j = \sigma_j - if_j$. In the following, the eigenmode with maximal growth rate will be named the *leading* eigenmode, with eigenvalue λ_0 and eigenvector $\boldsymbol{\phi}_0$.

Homogeneous Dirichlet boundary conditions are prescribed for all fluctuations, except pressure, at the inflow, no-slip adiabatic conditions are imposed at the lateral channel walls, and no-slip isothermal conditions, i.e. zero fluctuations of density and velocity, are chosen on the cylinder surface. Stress-free boundary conditions at the outflow are used, which is a common and convenient choice in finite-element formulations for low spurious reflections (e.g. Lesshafft 2018).

3.3 Non-reacting flow

Nonlinear simulation is first performed for a non-reacting flow at $\text{Re} = 500$. The terms related to chemical reaction, $\dot{\omega}_{\text{CH}_4}$ and $\dot{\omega}_T$, are removed from the governing equations

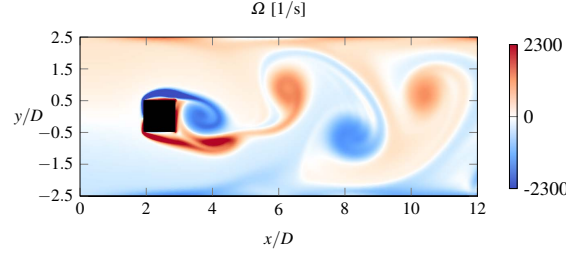


Figure 3.2: Snapshot of the vorticity field of the non-reacting flow, obtained by nonlinear timestepping.

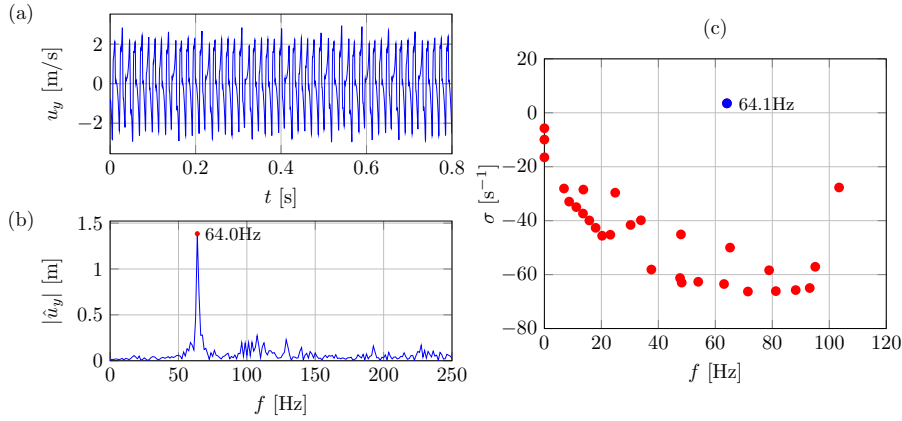


Figure 3.3: (a) Time evolution of u_y measured at location $(x/D, y/D) = (4.5, 0)$ in the non-reacting flow. (b) Frequency spectrum of the signal in (a). (c) Eigenvalues of the non-reacting mean flow. The unstable eigenvalue has $f = 64.1$ Hz, $\sigma = 3.5$ s⁻¹, marked in blue.

for this calculation, and the cylinder temperature T_c is set to be the same as the inflow temperature. Figure 3.2 shows the periodic regime of vortex shedding, in agreement with figure 4 of Kedia and Ghoniem 2014. Note that, due to the parabolic inlet profile and the confinement by no-slip channel walls, the vortex dynamics observed here is different from an unbounded uniform flow past a square cylinder (Davis et al. 1984; Suzuki et al. 1993; Turki et al. 2003).

The temporal signal of the cross-stream velocity u_y , measured at the location $(x/D, y/D) = (4.5, 0)$, is shown in figure 3.3a, and its frequency spectrum is given in figure 3.3b. The temporal signal is quasi-periodic and appears to be near the onset of chaotic dynamics. A distinct peak at 64.0 Hz corresponds to the vortex shedding frequency.

The nonlinear flow fields are averaged over the time horizon shown in figure 3.3a, and perturbation eigenmodes are computed for this mean flow. A leading eigenvalue at 64.1 Hz is identified, in excellent agreement with the measured vortex shedding frequency. Here, the growth rate is found to be $\sigma = 3.5$ s⁻¹, relatively close to zero, therefore fairly consistent with the RZIF criterion. This slightly non-zero growth rate may be attributed to the weak non-periodicity of the unsteady flow (Mantič-Lugo et al. 2014). More details about this non-reacting flow analysis results are given in Appendix A, including a comparison of eigenmodes obtained for base flow and mean flow, and convergence tests with respect to the domain length and to the time averaging interval used in the construction of the mean flow.

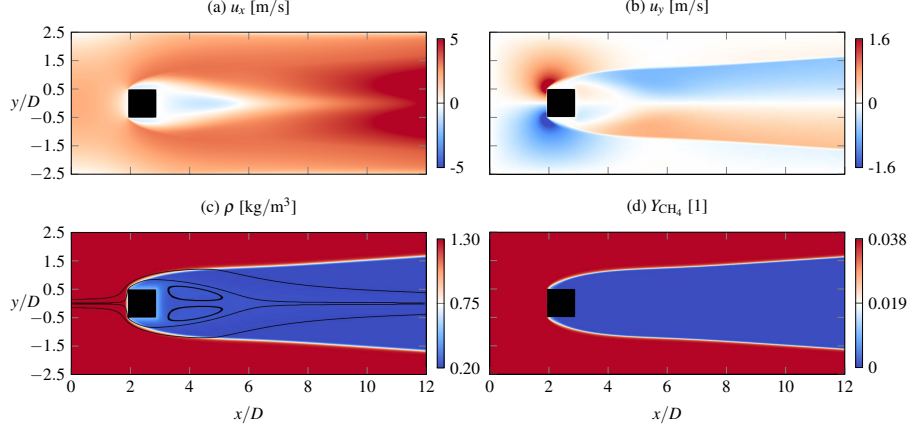


Figure 3.4: Reacting base flow at $T_c = 800$ K. Streamlines are superposed on the density field ρ to visualise recirculation in the flame.

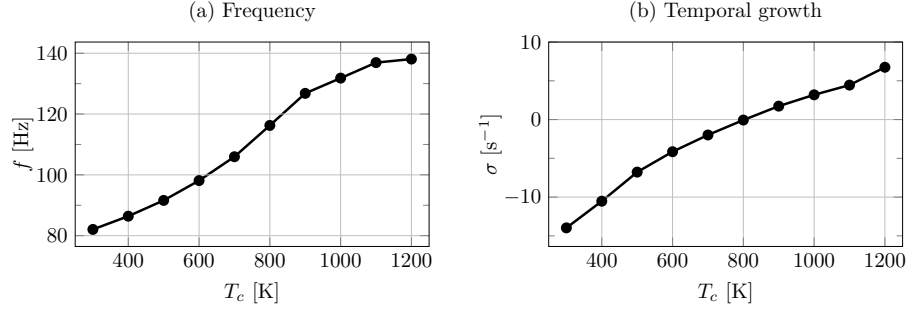


Figure 3.5: Frequency f and growth rate σ of the leading eigenmode of a reacting base flow as a function of cylinder temperature T_c from 300 K to 1200 K.

3.4 Reacting flow: studies on the steady base state

3.4.1 Global modes in base flow

In this section, the steady base state of a reacting flow is computed at various cylinder temperatures T_c , ranging from 300 K to 1200 K with increments of 100 K. The Reynolds number is always 500, and the inflow temperature is maintained at 300 K. A typical steady base state of the reacting flow is shown in figure 3.4 for $T_c = 800$ K: the flame front is anchored on the cylinder, advancing towards the channel walls with downstream distance. A recirculation zone, immediately behind the cylinder, is spatially separated from the flame fronts. These base states resemble the steady states found in the simulations (Kedia and Ghoniem 2014), in spite of our different temperature condition at the cylinder and the simplified reaction scheme.

Eigenmode analysis is conducted on each base flow obtained with different T_c . The frequency and growth of leading eigenvalues are presented in figure 3.5. For cylinder temperatures below 800 K, the leading mode has negative growth and the flow therefore is stable. Heating the cylinder has a significant effect on both the frequency and the growth rate: the frequency almost doubles as T_c is increased from 300 to 1200 K, and the flow becomes unstable at around 800 K.

The effect of cylinder temperature on the global instability of the flame is demonstrated by nonlinear simulation. We take an oscillating flame at $T_c = 1000$ K as the initial field, and we gradually reduce T_c down to 600 K during runtime, according to the variation

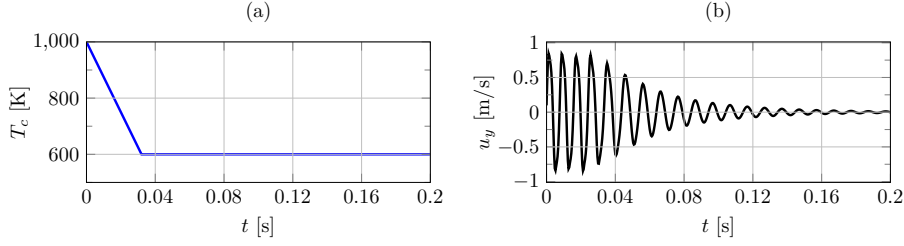


Figure 3.6: Controlled temporal variation of T_c (a), and resulting oscillations u_y at the location $(x/D, y/D) = (4.5, 0)$.

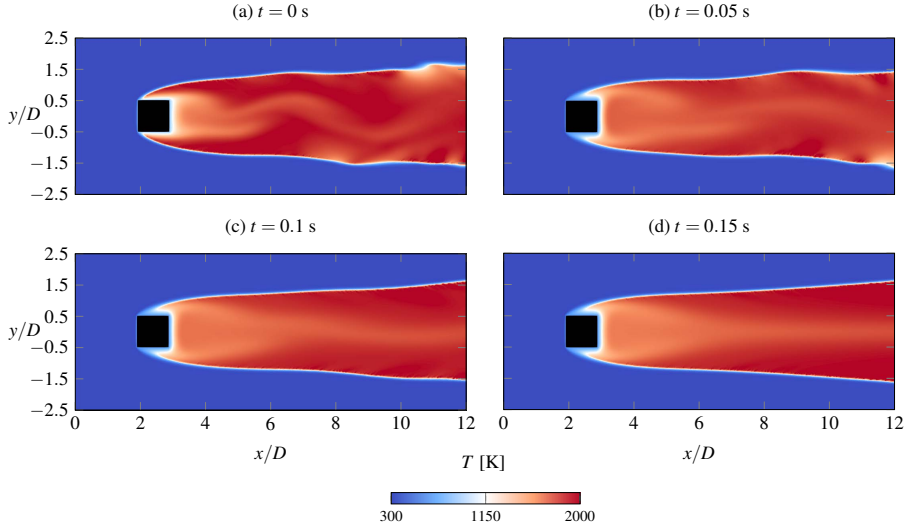


Figure 3.7: Snapshots of the temperature field as T_c changes from 1000 K to 600 K.

displayed in figure 3.6a. The response of the flame to this change of T_c is characterised by the cross-stream velocity u_y , measured at the same position $(x/D, y/D) = (4.5, 0)$ as in the non-reacting case (figure 3.6b). Snapshots of the associated temperature field are presented in figure 3.7. The reacting flow is indeed stabilised as the cylinder temperature is reduced: the oscillation is gradually suppressed, and the flow ultimately settles into its steady state. This nonlinear behaviour is consistent with the linear instability of the base flow. As heating or cooling the flame holder is a practical operation in some common combustor chambers (Miguel-Brebion et al. 2016; Mejia et al. 2018; Cheng et al. 2021), it may provide a simple strategy for the passive control of flame instability.

Eigenmodes of the base flow with critical cylinder temperature $T_c = 800$ K are chosen for a more detailed inspection. The eigenvalue spectrum for this case, in figure 3.8, shows an isolated leading eigenvalue with near-zero growth rate, as well as some stable branches. Most of the stable eigenmodes feature strong fluctuations near the outlet, probably due to the effect of domain truncation (Garnaud et al. 2013a; Lesshafft 2018). The structure of the leading mode is presented in figure 3.9. Its streamwise velocity component is concentrated near the centreline within the hot flame region, typical of the Bénard-von Kármán vortex street, with almost no signature in the flame front. The cross-stream velocity component, however, also has significant amplitudes in the flame front region. This difference can be understood from the base flow velocity gradients across the flame front, which are strong for the cross-stream component, but weak for the streamwise component. Oscillations of the flame front position therefore are clearly visible in the cross-stream velocity perturbations, as well as in the temperature and fuel fraction fields of the instability eigenmode.

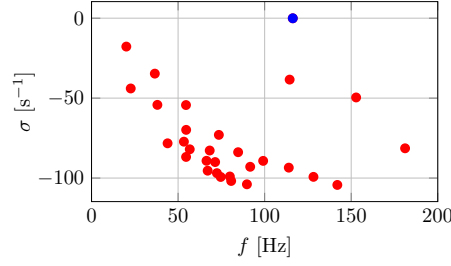


Figure 3.8: Eigenvalues of the reacting base flow at $T_c = 800$ K. The leading eigenvalue with frequency $f = 116.3$ Hz and growth rate $\sigma = -0.1 \text{ s}^{-1}$ is marked in blue.

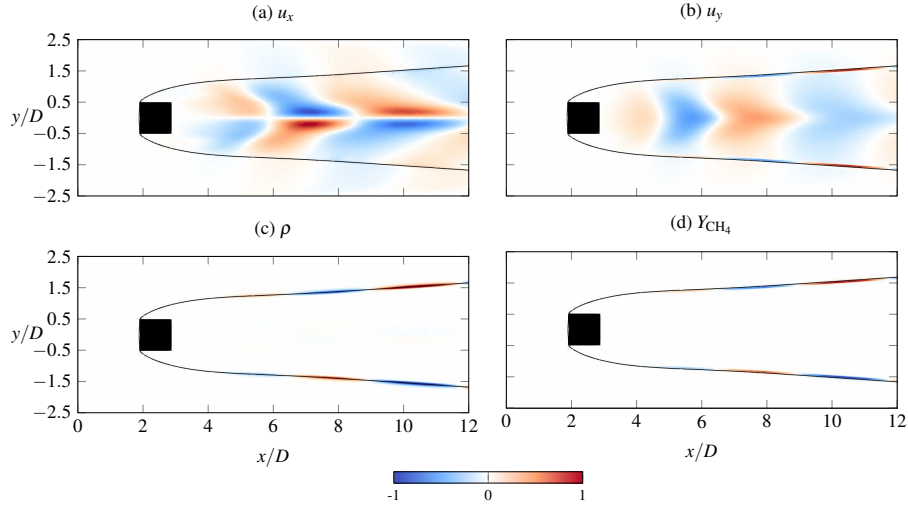


Figure 3.9: Leading eigenmode of the reacting base flow at $T_c = 800$ K. Blue: negative, red: positive. The base flow temperature isocontour of 500 K is superposed, showing the location of flame fronts. All the fields are normalised by their maximum value.

The amplitude of these oscillations in the flame front grow in the downstream direction, suggesting a convective amplification.

3.4.2 Wavemaker analysis

The two main observations from the previous section are the following: (i) at low cylinder temperature, the presence of the flame stabilises the flow; (ii) the instability sets in again as the cylinder temperature is increased above 800 K.

The stabilising effect of reaction has often been observed in experiments and numerical simulations (Bill and Tarabanis 1986; Mehta and Soteriou 2003; Erickson and Soteriou 2011; Kedia and Ghoniem 2014; Oberleithner et al. 2015b; Geikie et al. 2021). A “wavemaker” analysis was carried out by Emerson et al. 2016, in order to identify the sensitivity of the eigenvalue to changes in intrinsic feedback mechanisms. Global eigenmodes were estimated by combining the results from local analysis (Juniper and Pier 2015), and the wavemaker region was found in the recirculation zone of the wake. In the analysis of Emerson et al. 2016, the authors assumed *a priori* that the instability is shear-driven: only the velocity and density fields were taken as input, whereas the effects of unsteady chemical reaction were not taken into account. In this section, we attempt a wavemaker analysis without the quasi-parallel assumption, based on the global modes obtained from the reacting flow equations.

First, the *adjoint eigenvectors* ϕ_j^\dagger are introduced as the eigenvectors of the conjugate-

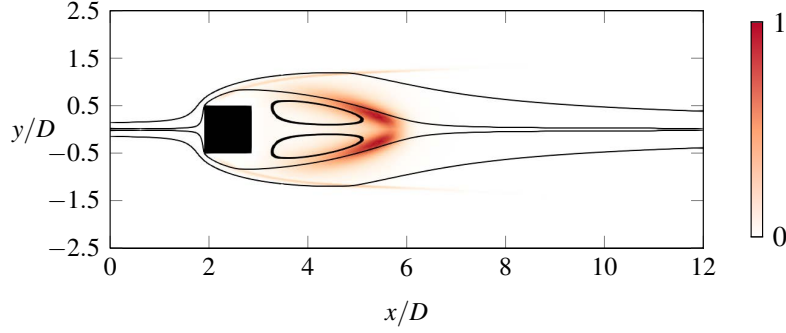


Figure 3.10: Structural sensitivity (Frobenius norm) of the nearly marginally unstable eigenmode at $T_c = 800$ K: wavemaker according to the definition by Giannetti and Luchini 2007. The field is normalised with its maximum value. The streamlines are superposed.

transposed system matrices of (3.11),

$$\lambda_j^* \mathbf{B}^H \phi_j^\dagger = \mathbf{A}^H \phi_j^\dagger. \quad (3.12)$$

A *direct* eigenvector ϕ_j and an adjoint eigenvector ϕ_j^\dagger are thus associated by their complex conjugated eigenvalues. The sets of direct and adjoint eigenvectors, appropriately normalised, fulfill the biorthogonality relation (Hill 1995),

$$\langle \phi_j^\dagger, \mathbf{B} \phi_k \rangle = \delta_{jk}, \quad (3.13)$$

where the spatial inner product over the flow domain Ω is defined as

$$\langle \mathbf{g}(\mathbf{x}), \mathbf{h}(\mathbf{x}) \rangle = \int_{\Omega} \mathbf{g}^* \mathbf{h} d\mathbf{x}. \quad (3.14)$$

The “wavemaker”, as identified by the most commonly used definition of Giannetti and Luchini 2007, is shown in figure 3.10 for the nearly marginally unstable eigenmode at $T_c = 800$ K. The represented quantity is the local Frobenius norm of the structural sensitivity tensor, which is constructed as a local product of the direct and associated adjoint eigenmode (Giannetti and Luchini 2007). Flow regions where this quantity is large are expected to contribute strongly to the global flow instability, through what is commonly called “local feedback mechanisms” in the literature. On this basis, the instability seems to be generated mainly in the shear region of the recirculation bubble in the near wake, close to the downstream stagnation point. This dominant feature in figure 3.10 closely resembles the non-reacting cylinder wake results of Giannetti and Luchini 2007, indicating that similar instability mechanisms are at play in both flow configurations. However, although less prominently, the flame front in the near wake also emerges as part of the wavemaker in figure 3.10.

For further analysis, a variation of the wavemaker definition is used in the following, as proposed by Marquet and Lesshafft 2015, and applied by Chakravarthy et al. 2018 and Paladini et al. 2019. From (3.11) and (3.13), the leading eigenvalue is obtained in the form of a spatial integral,

$$\lambda_0 = \langle \phi_0^\dagger, \lambda_0 \mathbf{B} \phi_0 \rangle = \langle \phi_0^\dagger, \mathbf{A} \phi_0 \rangle = \int_{\Omega} \mathbf{E}(\mathbf{x}) d\mathbf{x}. \quad (3.15)$$

The integrand $\mathbf{E}(\mathbf{x})$ is given by the spatially local product between ϕ_0^\dagger and $\mathbf{A} \phi_0$. Marquet and Lesshafft 2015 name $\mathbf{E}(\mathbf{x})$ the “endogeneity” of the eigenmode, and we will adopt this

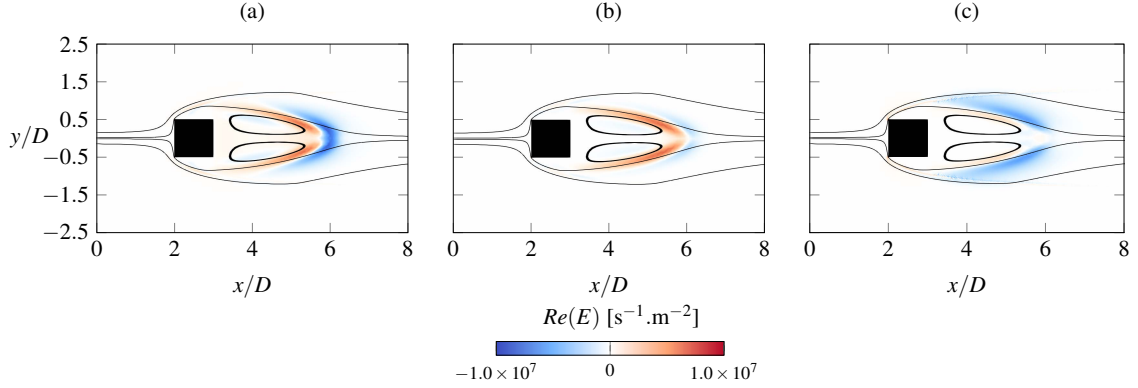


Figure 3.11: Endogeneity field $Re[\mathbf{E}(\mathbf{x})]$ of the nearly marginally unstable eigenmode at $T_c = 800$ K: wavemaker according to the definition by Marquet and Lesshafft 2015. (a) full endogeneity, with spatial integral $Re(\lambda_0) = -0.1 \text{ s}^{-1}$; (b) contribution of the momentum perturbation production term; (c) contribution of the momentum perturbation convection term. The streamlines are superposed.

word for ease of writing. The growth rate $Re(\lambda_0)$ is given by the spatial integral of $Re(\mathbf{E})$, therefore regions where $Re(\mathbf{E})$ is positive are expected to contribute to the destabilisation of the leading eigenmode; conversely, flow regions with negative values are interpreted as having a stabilising influence.

Figure 3.11a displays $Re(\mathbf{E})$ for the neutrally stable flame case with $T_c = 800$ K. Consistent with the wavemaker definition used in figure 3.10, the shear layer near the downstream end of the recirculation bubble is identified as the flow region that most strongly influences the instability growth rate. An inner positive region and an outer negative region appear in the endogeneity plot, both approximately of equal strength, so that $Re(\mathbf{E})$ over the entire domain integrates to $Re(\lambda_0) = -0.1 \text{ s}^{-1}$.

The matrix \mathbf{A} in the wavemaker definition (3.15) can be split into components that represent individual terms of the linearised flow equations, and the isolated contributions of these terms can be visualised as partial endogeneity fields (Marquet and Lesshafft 2015; Chakravarthy et al. 2018). A detailed analysis (see Appendix C) reveals that the dominant contributions to the growth rate stem from the perturbation production term $\rho(\mathbf{u}' \cdot \nabla)\mathbf{U}$ and from the convection term $\rho(\mathbf{U} \cdot \nabla)\mathbf{u}'$ in the linearised momentum equation. The local products of these terms with the adjoint velocity field \mathbf{u}^\dagger , for the dominant eigenmode, are shown in figures 3.11b,c. It is found that the positive and negative regions of the total endogeneity are rather neatly isolated in the partial endogeneity fields due to production and convection, respectively.

3.4.3 Influence of reaction on the base flow

We first examine why the presence of a flame stabilises the flow. In the reference case, Kedia and Ghoniem 2014 confirmed that the flame is stable in all their calculations of reacting flows, whereas the non-reacting flow was found to be unstable. The base flow eigenmodes show consistent results: when keeping the square cylinder temperature at $T_c = 300$ K, ignition reduces the growth rate from $\sigma = 9.1 \text{ s}^{-1}$ in the non-reacting case (see Appendix A) to $\sigma = -13.9 \text{ s}^{-1}$ in the reacting case (figure 3.5b).

Figure 3.12 shows the base state streamlines superposed on the temperature fields, and the associated vorticity fields, of the non-reacting flow and the reacting flow at $T_c = 300$ K. The non-reacting flow is isothermal. For the reacting flow, the flow temperature gradually increases downstream due to the chemical reaction. The flame is situated inside the shear

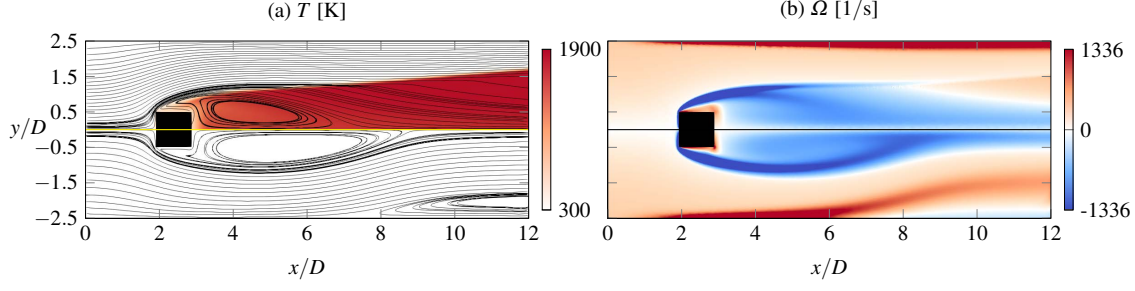


Figure 3.12: Comparison of base flow quantities between reacting flow at $T_c = 300$ K (upper half) and non-reacting flow (lower half). Streamlines superposed on the temperature fields in (a).

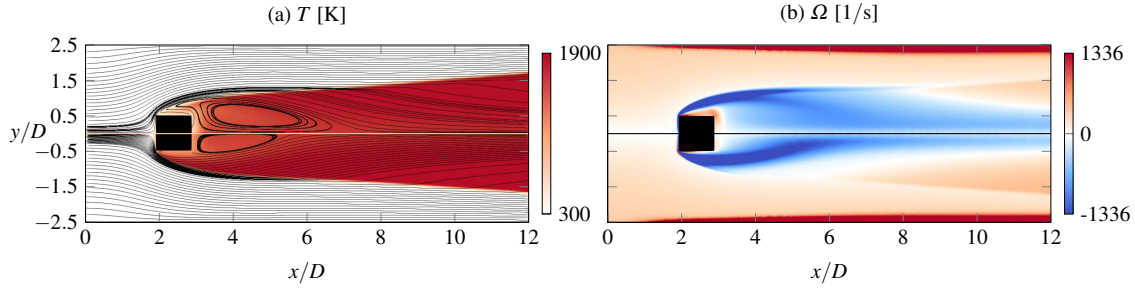


Figure 3.13: Comparison of base flow quantities between reacting flow at $T_c = 300$ K (upper half) and at $T_c = 1000$ K (lower half). Streamlines superposed on the temperature fields in (a).

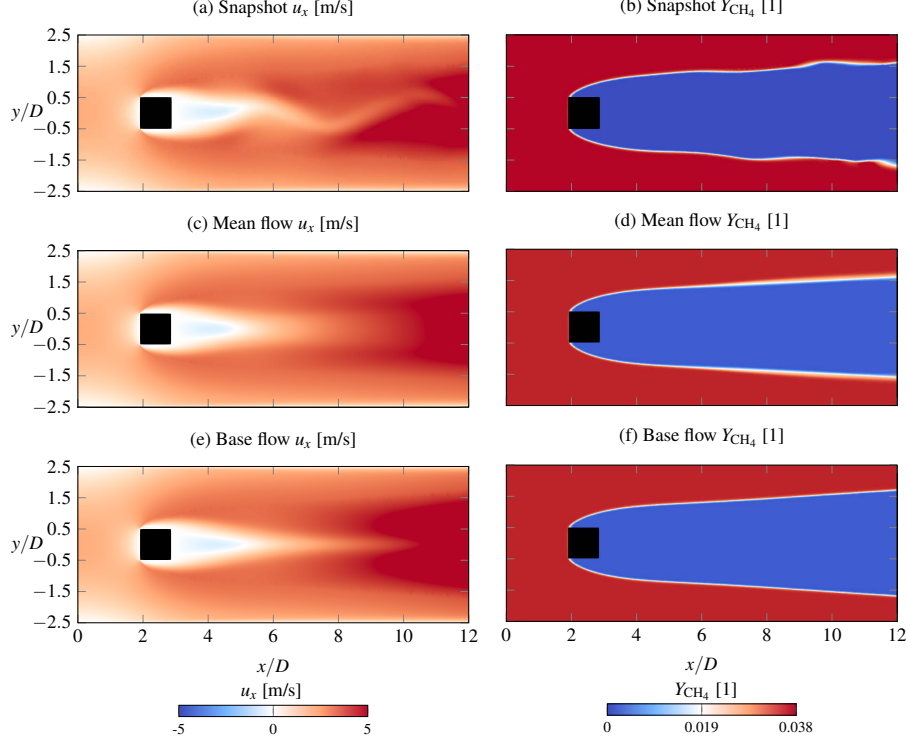
layer in the most upstream part of the wake. The fluid is strongly accelerated normal to the flame front due to the thermal expansion. Consequently, the recirculation bubble is shortened and the wake shear is weakened, as illustrated by the vorticity field in figure 3.12b. The wavemaker analysis has suggested that the instability is mainly controlled by the shear region of recirculation bubble, so a reduced shear weakens the global instability.

In the reacting flow, heating the cylinder increases the growth rate, and instability sets in at a cylinder temperature above 800 K. Figure 3.13 shows the comparison of reacting base flows at $T_c = 300$ K and $T_c = 1000$ K. In the case of $T_c = 1000$ K, the flame front is situated outside the shear layer and the thermal acceleration sets in further upstream. Therefore, the entire shear layer is concentrated while it is squeezed inwards, as shown by the associated vorticity field, which destabilises the flow.

3.5 Reacting flow: mean flow analysis

We consider the case of an unstable flame in the limit cycle. The mean fields and temporal snapshots, shown in figure 3.14a-d, are produced using nonlinear timestepping for $T_c = 1000$ K. The temporal signal of cross-stream velocity u_y at the location $(x/D, y/D) = (4.5, 0)$ is shown in figure 3.15a together with its frequency spectrum in figure 3.15b. Primitive flow variables are averaged over the time horizon shown in figure 3.15a. Note that the mean flow definition depends on the choice of flow variables (Karban et al. 2020). The mean flow quantities are represented by u_x and Y_{CH_4} in figure 3.14c,d. In comparison with their base state counterparts in 3.14e,f, a slightly shorter wake is observed in the mean flow, with a significantly thicker flame front downstream.

The spectrum of the mean flow eigenvalues is given in figure 3.15c. A leading eigenvalue ($f = 132.3$ Hz, $\sigma = 0.2$ s $^{-1}$) separated from all the stable branches is identified. Both base flow and mean flow leading eigenmodes agree well with the measured vortex shedding

Figure 3.14: Snapshot, mean flow and base flow of the reacting flow at $T_c = 1000\text{K}$.Table 3.1: Summary of the base and mean flow analysis results of the reacting flow. Units $[\text{s}^{-1}]$.

measured	base flow eigenvalue	mean flow eigenvalue
132.2	$136.2 + 2.1j$	$132.3 + 0.2j$

frequency, the mean flow mode matching the measured frequency more precisely. The base flow mode is unstable with a slightly positive growth rate, while the mean flow mode has a growth rate of nearly zero, which is consistent with the RZIF criterion (Turton et al. 2015; Bengana and Tuckerman 2021). A comparison with the “passive flame” approach is presented in the Appendix B, and it is shown that the presence of chemical reaction in the linearised equations is necessary in order to accurately capture the oscillating frequency.

In the reacting flow, the growth rate is close to zero ($\sigma = 0.2 \text{ s}^{-1}$), while its counterpart is slight positive in the non-reacting case ($\sigma = 3.5 \text{ s}^{-1}$). Such results are justified by their measured frequency spectrum in figure 3.15b and 3.3b, respectively. The reacting flow shows an oscillatory flow with a distinct frequency peak. In the non-reacting case, small-amplitude components are found apart from the fundamental frequency, showing that the flow is at the onset of chaotic behavior. The reacting case is close to the bifurcation point, while the non-reacting case is not, which leads to stronger nonlinear effects in the latter.

3.6 Conclusions

The global linear instability of a cylinder anchored flame has been investigated, based on the flow equations including chemical reactions. From the analysis on the steady-state base flow, the critical cylinder temperature T_c for global instability transition was predicted. A

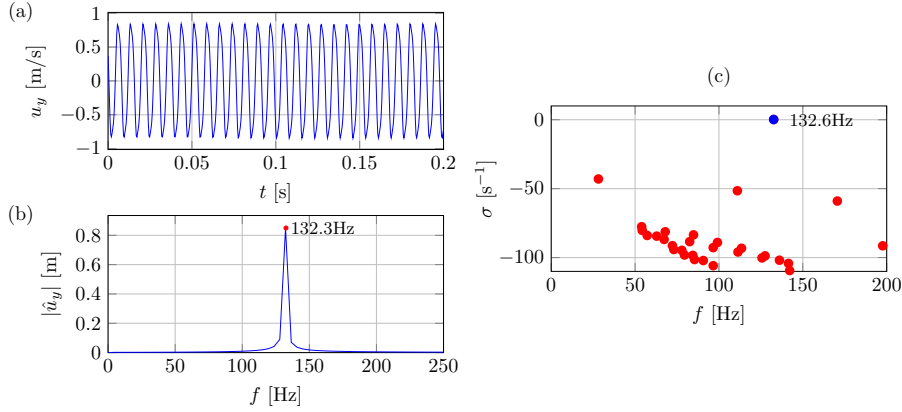


Figure 3.15: (a) Time evolution of u_y measured at location (4.5, 0) of reacting flow ($T_c = 1000$ K). (b) Frequency spectrum of signal in (a). (c) Eigenvalues of the reacting mean flow. The leading eigenvalue is $f = 132.3$ Hz, $\sigma = 0.2$ s $^{-1}$, marked with blue.

mean field analysis of the reacting flow in a limit cycle was conducted. It was shown that the oscillation frequency is very well captured, in agreement with results from the literature on non-reacting wake flows. A comparison with a passive flame approach has demonstrated that the reaction term is essential for this agreement. A wavemaker analysis showed that the flame instability in this configuration is caused by hydrodynamical effects in the wake shear region, whereas the oscillation of flame front is a passive result.

The present work represents one of the first attempts to include a linearised chemical scheme in the analysis of a time-averaged reacting flow, and the result was found to be in perfect agreement with the RZIF criterion. Modal instability analysis of time-averaged mean flows therefore holds great promise for the investigation of flame instability phenomena, also in more complex configurations.

Appendix A: Linear analysis of a non-reacting wake

Both base flow and mean flow analysis are conducted in the non-reacting case. The steady base state closely resembles the initial axisymmetric state in figure 14 of Davis et al. 1984. The mean flow is characterized by a considerably shorter recirculation zone. The eigenspectra of base and mean flow are shown in figure 3.16. The frequencies found in both cases are close to the measured vortex shedding frequency, the mean field giving more accurate results. The growth rate in base state is larger than mean state as expected. Note that there are two unstable eigenvalues identified from the base state in figure 3.16a. The eigenmode with smaller growth exhibits a frequency quite different from the observed vortex shedding, and it is not found in the Fourier spectrum of the nonlinear signal. The existence of this second unstable mode is probably due to the highly supercritical Reynolds number, and this mode may be damped by nonlinear effects as the leading mode with the largest growth develops.

A test of convergence with respect to the domain length is conducted by calculating the base flow with extending the flow domain downstream to $1.5L$ and $2L$ of the standard length L . The base state eigenspectra are given in figure 3.16a, and it is found that the least stable eigenmodes are not sensitive with respect to domain length. A similar convergence test is also performed for the time horizon for averaging the mean flow. Two mean flows are successively obtained by averaging over the first 0.4 s (0-0.4 s) and the second 0.4 s (0.4-0.8 s) in figure 3.3a. It is shown that the least stable eigenmodes from both mean

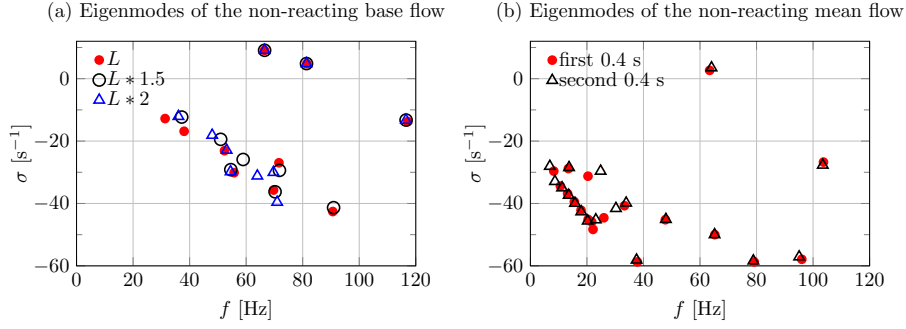


Figure 3.16: (a) Eigenmodes of the non-reacting base flow. The effect of domain length L is tested, with extending the domain downstream to $1.5L$ and $2L$. (b) Eigenmodes of the non-reacting mean flow. The effect of averaging mean flow is tested, with two mean flows averaged during the first 0.4 s (0-0.4 s) and the second 0.4 s (0.4-0.8 s) in figure 3.3, respectively.

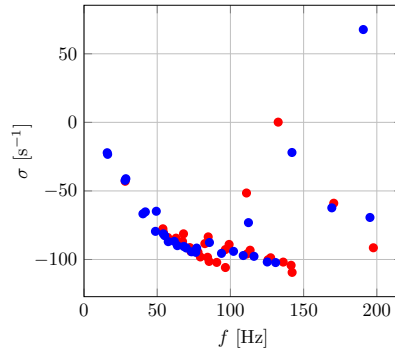


Figure 3.17: Eigenspectra of reacting mean flow obtained from the passive flame approach (blue) and from the complete linearised reacting flow equations (red).

states match each other well.

Appendix B: Examine the passive flame approach in predicting the oscillating frequency

We examine if the passive flame approach (Casel et al. 2022) captures the nonlinear oscillation frequency. The linear analysis is carried out on the reacting mean flow by using the linearised equations of which the chemical heat release in the energy equation and the reaction rate in the transport equation of CH_4 are removed. The eigenvalues obtained from the passive flame approach are shown in blue in figure 3.17. The leading eigenvalue is found to be unstable with a frequency much larger than the nonlinear oscillation frequency. The eigenmode structures of density and fuel mass are not concentrated in the flame front, because the effect of chemical reaction is not included.

Appendix C: contribution to the instability from different terms in flow equations

To quantitatively study the contribution to the global instability from different physical mechanisms, we apply now a decomposition of the eigenvalue by each individual equation. Each line in matrix \mathcal{A} contains the linearized right hand side of one of the four governing

equations (3.1-3.3) and (3.6) at a given grid point, which are in order the conservation equations of mass, momentum, species and enthalpy. By extracting all the lines corresponding to an equation, we can decompose \mathcal{A} into four matrix in the form

$$\mathcal{A} = \mathcal{A}_{\text{mass}} + \mathcal{A}_{\text{momentum}} + \mathcal{A}_{\text{species}} + \mathcal{A}_{\text{enthalpy}}. \quad (3.16)$$

Each matrix on the right hand side is associated with one of the conservation equations at all grid points. The eigenvalue λ_j may then be decomposed in the form

$$\begin{aligned} \lambda_j &= \langle \phi_j^\dagger, \mathcal{A} \phi_j \rangle = \langle \phi_j^\dagger, \mathcal{A}_{\text{momentum}} \phi_j \rangle + \langle \phi_j^\dagger, (\mathcal{A}_{\text{mass}} + \mathcal{A}_{\text{species}} + \mathcal{A}_{\text{enthalpy}}) \phi_j \rangle \\ &= \lambda_{j,\text{momentum}} + \lambda_{j,\text{others}}. \end{aligned} \quad (3.17)$$

$\lambda_{j,\text{momentum}}$ represents the contribution to the j -th eigenmode from the momentum equation and may be considered as purely hydrodynamic effects. $\lambda_{j,\text{others}}$ includes the contribution to the j -th eigenmode from all the other three equations present in the reacting flow equations. Such decomposition is performed for the leading eigenvalue λ_0 in base states of each investigated bluff body temperature T_c and the results are presented in figure 3.18(a). The total temporal growth σ_0 is strongly correlated with $\sigma_{0,\text{momentum}}$, and other equations present due to reactions play a much less significant role.

We now study the detailed contribution of each term in the momentum equations. The linear operator $\mathcal{A}_{\text{momentum}}$ is decomposed into four individual parts

$$\mathcal{A}_{\text{momentum}} = \mathcal{A}_{\text{convection}} + \mathcal{A}_{\text{production}} + \mathcal{A}_{\text{density}} + \mathcal{A}_{\text{pressure}} + \mathcal{A}_{\text{dissipation}}, \quad (3.18)$$

where the linear operators on the right hand side represent convection of perturbation $\bar{\rho} \bar{\mathbf{u}} \nabla \mathbf{u}'$, production of perturbation $\bar{\rho} \mathbf{u}' \nabla \bar{\mathbf{u}}$, density perturbation $\rho' \bar{\mathbf{u}} \nabla \bar{\mathbf{u}}$, pressure $-\nabla p'$, and dissipation $\Delta \mathbf{u}'$ terms successively. The base flow quantities therein are expressed as $\bar{\cdot}$ and the fluctuations as \cdot' . The corresponding eigenvalue contributions are computed in the same manner as equation 3.17 satisfying the relation

$$\lambda_{j,\text{momentum}} = \lambda_{j,\text{convection}} + \lambda_{j,\text{production}} + \lambda_{j,\text{density}} + \lambda_{j,\text{pressure}} + \lambda_{j,\text{dissipation}}. \quad (3.19)$$

We focus once more on the leading eigenmode $j = 0$. The contribution of pressure term $\lambda_{0,\text{pressure}}$ is found to be strictly zero, which is the same result in Marquet and Lesshafft 2015. Note that $\lambda_{0,\text{pressure}} = 0$ simply means the net integrated value of the endogeneity associated with the pressure term vanishes, but it does not mean the pressure endogeneity distribution is zero everywhere in the domain. Figure 3.18(b) shows the instability budget in the momentum equation from the other four terms. Main instability effects originate from $\sigma_{0,\text{convection}}$ and $\sigma_{0,\text{production}}$: the convection stabilizes the flow, whereas the production destabilizes the flow. Contributions from the other two terms are much less pronounced: dissipation has a slightly stabilizing effect and the effect from density perturbation is quite negligible. These results are again highly consistent with the instability budget in the cold cylinder wake (figure 8 in Marquet and Lesshafft 2015). In both cases, it is the net effect of convection and production that principally controls the global instability.

Declaration of Interests

The authors report no conflict of interest.

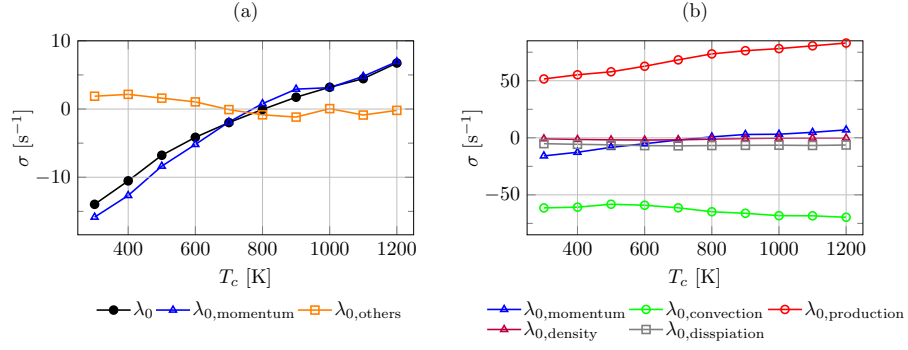


Figure 3.18: (a) Contribution to the temporal growth σ_0 from momentum equations ($\sigma_{0,\text{momentum}}$) and the sum of other equations ($\sigma_{0,\text{others}}$). (b) Decomposition of the contribution of momentum equations $\sigma_{0,\text{momentum}}$: convection of perturbations $\bar{\rho}\bar{\mathbf{u}}\nabla\mathbf{u}'$ ($\sigma_{0,\text{convection}}$), production of perturbations $\bar{\rho}\mathbf{u}'\nabla\bar{\mathbf{u}}$ ($\sigma_{0,\text{production}}$), density perturbations $\rho'\bar{\mathbf{u}}\nabla\bar{\mathbf{u}}$ ($\sigma_{0,\text{density}}$) and dissipation $\Delta\mathbf{u}'$ ($\sigma_{0,\text{dissipation}}$). The contribution related to the pressure term $-\Delta p'$ ($\sigma_{0,\text{pressure}}$) is zero and not shown in the chart.

Acknowledgements

The authors are grateful to Chuhan Wang's PhD jury members Denis Sipp, Taraneh Sayadi, Matthew Juniper, Laurent Gicquel, Franck Nicoud and Tim Lieuwen for their suggestions for improving this work. Chuhan Wang is supported through a scholarship by Ecole Polytechnique. The authors gratefully acknowledge the Deutsche Forschungsgemeinschaft (DFG) for funding this work within the project 441269395.

CHAPTER 4

Modal analysis of a V-shaped flame

We investigate the instability of a V-shaped flame in a geometry where the intrinsic thermoacoustic instability is expected to occur. This chapter describes ongoing work and the results presented are preliminary. The collaborators of this work are Grégoire Varillon and Wolfgang Polifke from TU Munich. Grégoire Varillon chose the parameters of computational domain and conducted nonlinear simulations with OpenFOAM to obtain the steady base states of the V-shaped flame.

Contents

4.1	Motivation	64
4.2	Preliminary results	64
4.2.1	Case $Re = 200$	64
4.2.2	Case $Re = 5000$	67
4.3	Future plan	68

4.1 Motivation

In this project, we study the linear stability of a premixed laminar V-shaped flame, stabilized on an annular burner with a central rod. The V-flame can be visualised in figure 4.1(a) from the heat release of steady base flow calculated by OpenFOAM. There are three main motivations for studying such a V-flame configuration.

First, we intend to study a flame configuration with more complexity. Both configurations of the slot flame in §2 and the bluff-body stabilized flame in §3 are plane flames in Cartesian coordinates. Instead, the equations for a V-flame stabilized on an annular burner has to be formulated in cylindrical coordinates. A number of studies focused on the swirling turbulent V-shaped flames (Candel et al. 2014; Hermeth et al. 2014; Merk et al. 2018; Dupuy et al. 2020), yet the laminar V-shaped flame without swirl is also a benchmark case that has been studied experimentally (Schuller et al. 2003b,a). As discussed in the end of §3, the linearization of chemical reaction on the turbulent mean flows may be technically challenging. Hence, we consider here a laminar V-shaped flame.

Second, we concluded in §3 that hydrodynamic effects dominate the global instability, and the momentum equation contributes the most in that bluff-body stabilized flame. Such a result may have already been expected, as the presence of strong shear in the wake is obvious. We wonder if there is any case where the chemical reaction has a more important impact on the instability, which may result in more contributions to the temporal growth from the conservation equations of energy or species. Thus, we search for other configurations where the shear is less strong, or the shear region is overlapped with the flame front, contrary to the spatial separation between wake shear and flame front in the bluff-body stabilized flame. The latter is the case in the V-shaped flame presented in figure 4.1. The shear is represented by the magnitude of vorticity in figure 4.1(b). Strong shear regions are observed along the inflow channel walls and the lateral chamber walls. A relatively weak but still very visible shear regions is located at the exit of the inflow channel, corresponding to the inner shear layer of V-shaped flame (Guiberti et al. 2015), which coincides with the region of flame fronts indicated by the heat release in figure 4.1(a).

Finally, the appearance of the intrinsic thermoacoustic (ITA) instability has been documented in swirling V-shaped flames in experimental studies (Murugesan et al. 2018; Xu et al. 2021). We expect ITA modes to be present also in non-swirling V-shaped flames. In this chapter, the steady base state is calculated under the assumption of low-Mach number, whereas the global linear modes are calculated with the fully compressible governing equations, in order to include the effects of acoustic feedback that may give rise to the ITA mechanism.

We present the preliminary results of this project in §4.2 including two configurations of a V-shaped flame. The first case is set at a relatively low Reynolds number $Re = 200$ leading to a thicker flame front to test the implementation of linear solver. The second case is at a higher Reynolds number $Re = 5000$ in a geometry that appears suitable for the occurrence of intrinsic thermo-acoustic instability, as explained in the following. The global eigenmodes of those two steady base states are calculated. Future steps of this project are described in §4.3.

4.2 Preliminary results

4.2.1 Case $Re = 200$

The steady base state is calculated with the Navier-Stokes equations for reacting flow via OpenFOAM. The governing equations under the low-Mach-number assumption are

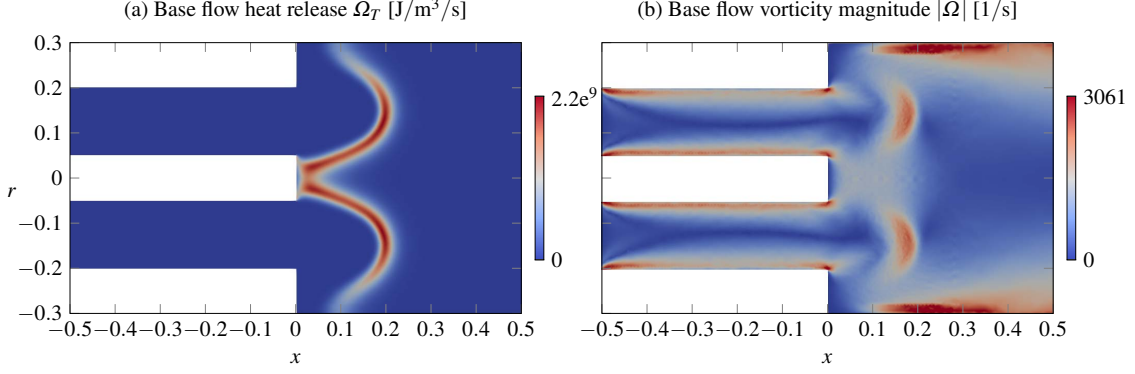


Figure 4.1: Case $Re = 200$: base flow. The units of domain length and width are in centimeter.

formulated in cylindrical coordinates. The swirl is not considered neither in the base state nor in the fluctuations, so the equations do not contain azimuthal components. The calculations are performed in the two-dimensional plane (x, r) , where x represents the axial direction and r represents the radial direction. In the following, we denote u_x as the axial velocity and u_r as the radial velocity.

The computational domain is the half-domain $r > 0$ presented in figure 4.1. The flame is anchored on the central rod of which the radius is 0.05 cm. The inflow channel is 0.5 cm long and 0.15 cm wide. The length of the combustion chamber is 0.5 cm and the radius is 0.3 cm. In the following of this chapter, all lengths are given in centimeters..

A no-slip wall condition is imposed on the central rod ($x = 0, 0 < r < 0.05$), the inner channel wall ($-0.5 < x < 0, r = 0.05$), the outer channel wall ($-0.5 < x < 0, r = 0.2$), the outer vertical wall ($x = 0, 0.2 < r < 0.3$) and the combustion chamber wall ($0 < x < 0.5, r = 0.3$). The thermal condition of the central rod is isothermal at $T = 1700$ K, and that of the outer vertical wall is isothermal at $T = 800$ K. Those two isothermal conditions lead to a flame of V-shape. If the temperature of the outer vertical wall is higher, it may become a M-shaped flame (Guiberti et al. 2015). All the other walls are adiabatic.

A uniform velocity profile $U = 0.5$ m/s is imposed at the inlet, which results in an inflow Reynolds number $Re = 200$. A premixed methane-air gas of equivalence ratio $\phi = 1$ is considered and the associated inlet boundary conditions for the transport species are implemented. The pressure at the outlet boundary is the atmospheric pressure. The global one-step model (CERFACS 2017) is applied for the premixed methane-air reaction, and only the transport equation of methane is required in the governing equations.

The global eigenmodes of the steady base state are calculated through the linearized governing equations that are fully compressible, contrary to the nonlinear base flow solver with low-Mach-number assumption. The results show that all the eigenmodes are stable in this configuration $Re = 200$, as presented in figure 4.2. The structure of the least stable eigenmode is presented in figure 4.3. The heat release fluctuation is of red and blue stripes along the flame front, which is consistent with the counterpart in the slot flame. The velocity fluctuations behave quite differently from the slot flame. In both axial and radial directions, the strong fluctuations are not only observed along the flame front, but also before and behind the flame front.

The effect of domain truncation on the linear global modes is investigated. We extend the computational domain three times downstream such that the computational domain ends at $x = 1.5$, by using the outlet profile $x = 0.5$ in all the extended domain. The eigenmodes corresponding to the extended domain are superposed with the actual com-

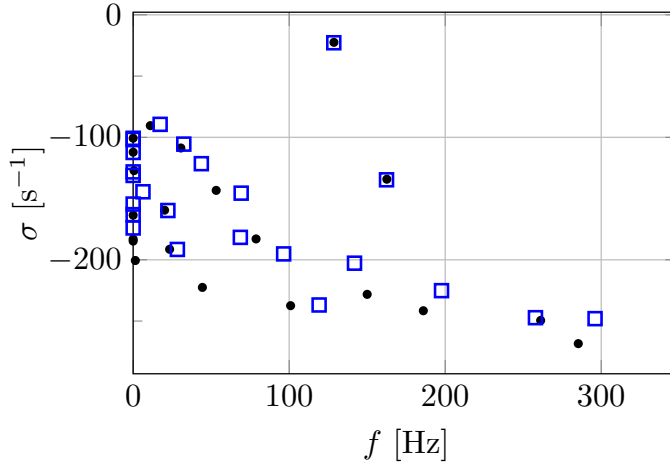


Figure 4.2: Eigenspectra of the case $Re = 200$. The black dots are the eigenspectra of the actual computational domain in figure 4.1 where the domain ends downstream at $x = 0.5$ cm. The blue squares are the eigenspectra of the computational domain extended downstream ending at $x = 1.5$ cm.

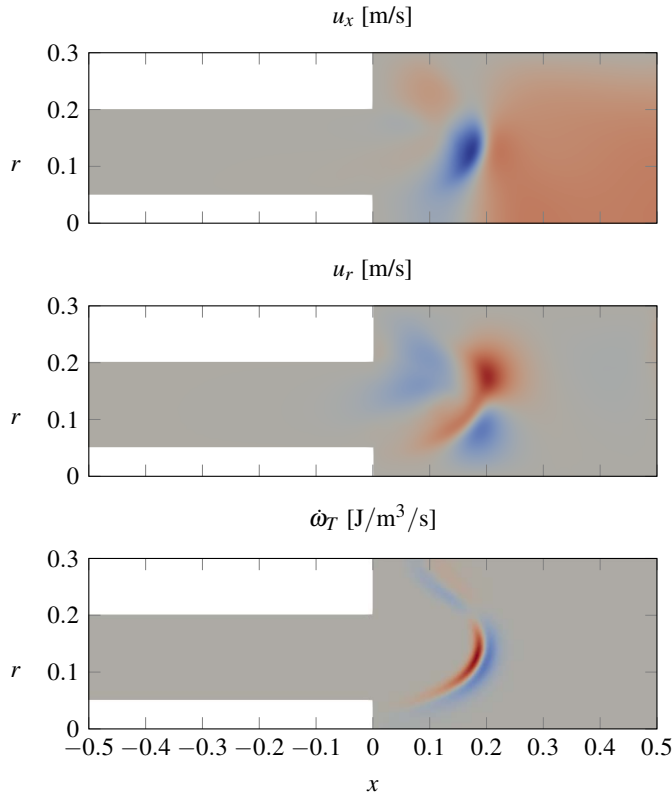


Figure 4.3: Zoom of leading eigenmode 128.7 Hz - 22.5 s^{-1} for the case $Re = 200$.

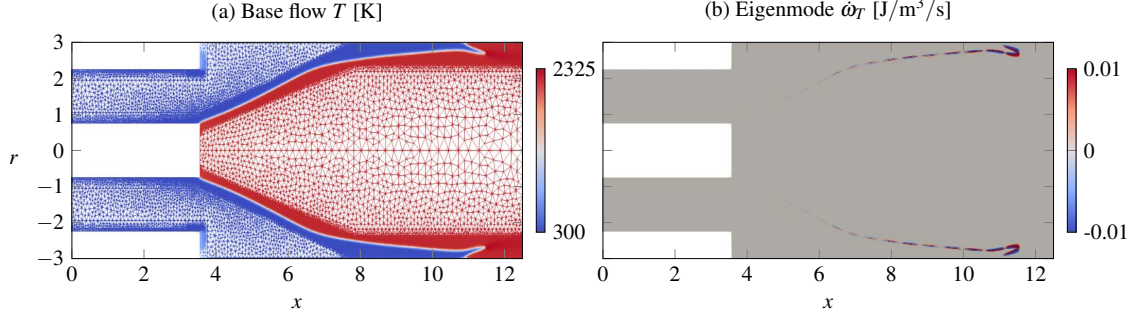


Figure 4.4: Case $Re = 5000$. (a) Mesh superposed base flow temperature field. (b) Real part of the heat release fluctuations corresponding to the eigenvalue $275.9 \text{ Hz} + 11.8 \text{ s}^{-1}$. In (b), the value of the real part of heat release fluctuation is normalised by its maximal value. The color of the heat release is significantly over-saturated (1% of the maximal value as shown in the label of colorbar) to visualize the fluctuation along the flame front. A zoom of the fluctuation at the flame tip region is shown in figure 4.6. The units of domain length and width are in centimeter.

putational domain in figure 4.2. The result shows that the least stable eigenmode is not influenced by the domain length. Hence, it seems to be an ITA mode that does not interplay with the outlet.

4.2.2 Case $Re = 5000$

A criterion of the occurrence of ITA instability considering both the gain and phase of FTF was proposed by Courtine et al. 2015. If we denote the FTF gain as $|F(\omega)|$ and the phase as $\arg[F(\omega)]$, an ITA mode may occur at the angular frequencies ω_c satisfying

$$\arg(F(\omega_c)) = (2q - 1)\pi \quad (q \in \mathbb{N}), \quad (4.1)$$

if the associated gain is beyond a threshold F_c expressed in the form

$$|F(\omega_c)| > F_c, \quad F_c = \frac{1}{T_2/T_1 - 1} \left(1 + \frac{S_2}{S_1} \sqrt{\frac{T_2}{T_1}} \right), \quad (4.2)$$

where S is the spanwise width and T is the temperature. The index 1 and 2 represent the upstream and downstream of the flame, respectively. This criterion underpins that an ITA mode is more probable to occur for a smaller expansion ratio $\frac{S_2}{S_1}$. In Courtine et al. 2015, an unstable ITA mode was reported to occur for a slot flame with $\frac{S_2}{S_1} = 2$ and $Re = 2000$. Thus, we use the same expansion ratio $\frac{S_2}{S_1} = 2$ and $Re = 5000$ for the V-flame.

The geometry of the flame is presented in figure 4.4. The radius of the central rod is 0.75 cm, and the radius of the combustion chamber is 3 cm. The width of inlet channel is 1.5 cm leading to an expansion ratio $\frac{S_2}{S_1} = 2$. The inflow velocity is $U = 2.5 \text{ m/s}$ that results in $Re = 5000$. The base flow temperature field is shown in figure 4.4(a) together with the mesh. The higher Reynolds number brings about a thinner flame front that extends much more downstream with respect to the case $Re = 200$. Such a thin flame front requires higher spatial resolution, as shown in the mesh of figure 4.4(a).

The nonlinear low-Mach-number solver produces a steady base flow. Interestingly, when we calculate the eigenmodes of the solver with the linear compressible solver, a branch of unstable eigenmodes are identified, as presented in figure 4.5.

The structure of eigenmode corresponding to an unstable eigenvalue ($275.9 \text{ Hz} + 11.8 \text{ s}^{-1}$) is illustrated by its heat release fluctuation in figure 4.4(b), where the heat release

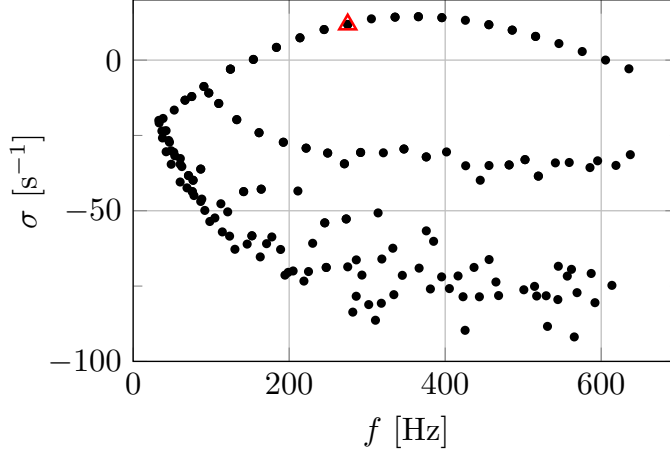


Figure 4.5: Eigenspectra of the case $\text{Re} = 5000$. The red triangle is the the eigenvalue $275.9 \text{ Hz} + 11.8 \text{ s}^{-1}$ at which we plot the eigenmode structures in figure 4.4(b) and in figure 4.6.

is observed along the spatially extended flame front. However, different from the case $\text{Re} = 200$, strong fluctuations are highly concentrated at the flame tip, as shown in the zoom of flame tip region in figure 4.6. The structure of velocity modes also suggests strong oscillations of the flame tip. Similar structures are observed in the other unstable eigenmodes along the unstable branch.

Several branches of stable eigenvalue are found in the eigenspectra, most of which take the form similar to the unstable eigenmodes. But there are fluctuations of similar magnitudes within the flame tip and the outlet of the computational domain. Further calculations of eigenmodes with different domain lengths are needed in order to rule out spurious effects from the numerical outflow..

4.3 Future plan

A remarkable result at this stage is that an unstable branch of eigenmodes is identified at $\text{Re} = 5000$ in a geometry of expansion ratio $\frac{S_2}{S_1} = 2$ where the ITA modes may occur. The unstable eigenmodes are obtained with the compressible solver from a steady base state calculated under the low-Mach-number assumption. It seems that those unstable modes occur because of the acoustic feedback introduced by the compressibility.

The next step of this project should be a validation of the current linear solver through a comparison of the FTF with respect to nonlinear simulations, which is the same procedure in §2.3.4 for validating the linear solver.

Once the linear solver is validated, we will conduct a wavemaker analysis to identify the active flow region that drives the global instability of flame. The endogeneity analysis performed in §3 for the bluff-body stabilized flame can be applied again, but this time we expect that the conservation equations of energy and species transport play a more important role.

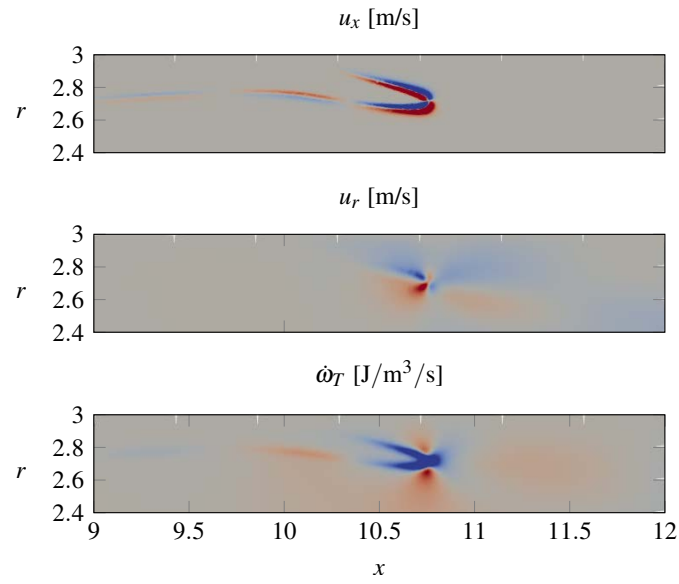


Figure 4.6: Zoom of eigenmode $275.9 \text{ Hz} + 11.8 \text{ s}^{-1}$ for the case $\text{Re} = 5000$.

CHAPTER 5

Towards coherent structures in jet flames: streaks in non-reacting jets

The instability of non-reacting jets is investigated with particular focus on the influence of streaks. The context of the study is first given, followed by a paper published in *Journal of Fluid Mechanics* (Wang et al. 2021). This chapter is a *side project* from the thesis topic flame instability, yet it is still very related to one of the future perspectives of that main topic, as described in the context.

Contents

5.1	Context	72
5.1.1	Streaks in boundary-layer flames	72
5.1.2	Streaks as optimal perturbations in shear flows	73
5.1.3	Linear instability mechanisms in jets	74
5.2	Paper: The effect of streaks on the instability of jets	76
5.2.1	Introduction	76
5.2.2	Evolution of rolls and streaks in a parallel jet	77
5.2.3	Linear stability analysis	80
5.2.4	Conclusions	87
5.3	Further discussions	89

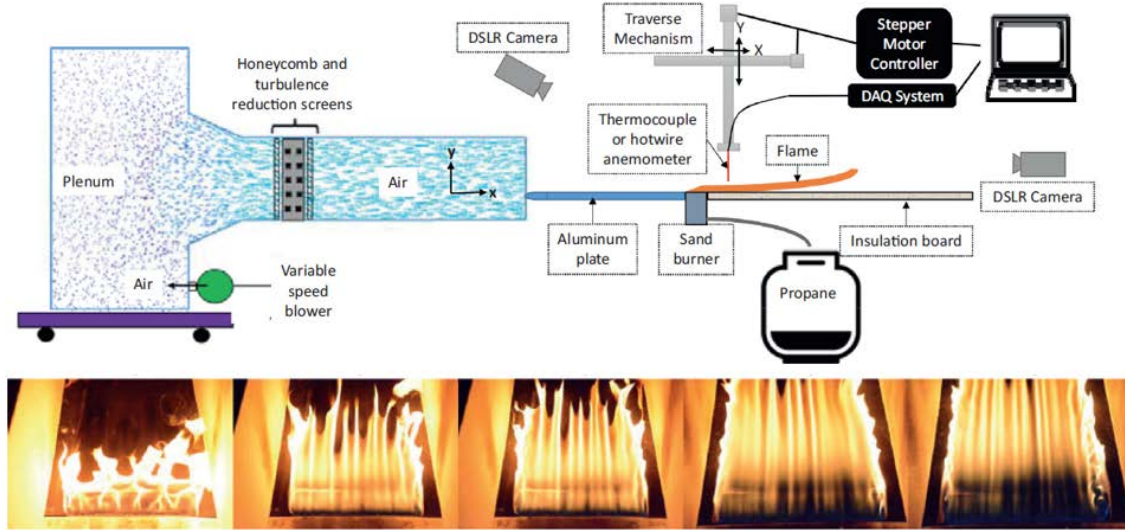


Figure 5.1: Streamwise streaks in boundary layer flames (figure taken from Miller et al. 2017). The upper half is the experimental set up. The lower half is overhead view of flames under different wind velocities.

5.1 Context

5.1.1 Streaks in boundary-layer flames

Streaks play a significant role in the instability and transition of wall-bounded flow such as boundary-layer flow, Couette flow and channel flow (Butler and Farrell 1992; Jiménez 2013). Streaks are characterised as streamwise elongated structures of high and low velocity with alternating patterns in the cross-plane. These large-scale structures originate from streamwise vortices that lift up low-speed fluid away from the wall and push high-speed fluid towards the wall, which is known as the *lift-up* mechanism (Landahl 1975).

In recent years, the presence of streaks in so-called *boundary-layer flames* was investigated experimentally. An important motivation of studying the reactive flows within a boundary layer is to model the wild fires propagating over the forests and grasslands (Finney et al. 2015). A laboratory-scale experimental setup of boundary-layer flame (Miller et al. 2017) is presented in figure 5.1. These experiments were carried out first in the laminar boundary layer (Miller et al. 2017, 2018). A burner is installed at the same level of a horizontal board at the exit of a wind tunnel. A boundary layer is developed along the horizontal surface, and coherent streaky structures of flame are observed within the boundary layer. The onset of streaks are controlled by the pre-existing velocity perturbations upstream. The growth and deformation of these structures further downstream depends on the buoyancy forces generated by heating the surface. Three-dimensional redistribution of temperature due to the existence of these coherent structures was reported. Higher temperature was measured in the streaks, while lower temperature was measured in the region between the streaks. The effect of freestream turbulence on these coherent structures was investigated (Ren et al. 2022). The incoming turbulent flow advances the onset of coherent structures and increases the growth of streaks in the streamwise direction.

A linear stability analysis of a boundary-layer flame was performed very recently by Hakes et al. 2021. The authors investigated the instability of the flames on the upper and lower surfaces of inclined burning plates. The temporal growth rate of perturbations, including streamwise vortices and spanwise traveling waves, was calculated with buoyancy

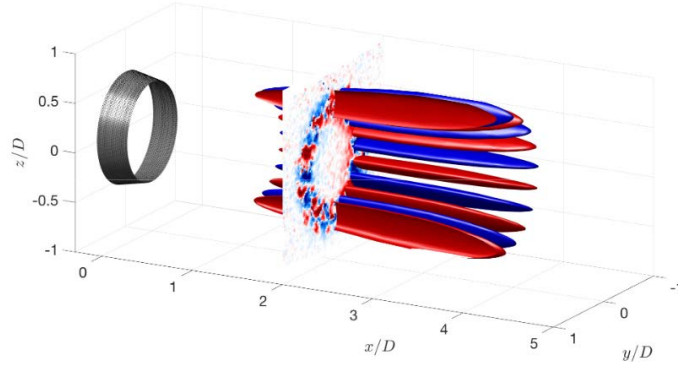


Figure 5.2: Streaky structures in turbulent jets (figure taken from Nogueira et al. 2019).

effects taken into account. The results of temporal growth successfully explained the experimental observations that the flame spreading underside the inclined surface extend further downstream than the upside surface.

The presence of streaks in flames is a relatively new research domain, and within our knowledge, the work of Hakes et al. 2021 is the first attempt of linear stability analysis where the streaks are taken into account as perturbations. In spite of its important motivation of modelling the spreading of wild fire driven by wind, the boundary-layer flame is a very specific configuration where the flame develops along a surface inside the boundary layer. More generally, a flame in a combustor or in an open atmosphere does not lie on any support, as it is the case of flame configurations investigated in the previous chapters. Apart from this, the presence of wall is not a necessary condition for the occurrence of streaks. The lift-up effect can be active in free shear flows as well (Brandt 2014).

The presence of large-scale streaky structures was recently reported in jets, obtained by the spectral proper orthogonal decomposition (SPOD) of experimental data (Nogueira et al. 2019), as shown in figure 5.2. Thus, it is expected that streaks are also present in turbulent jet flames. Towards studying the streaks in jet flames, we carry out a fundamental study, in this chapter, on the lift-up effect in non-reacting jets.

5.1.2 Streaks as optimal perturbations in shear flows

The growth of streaks induced by the streamwise vortices is associated with the non-normality of the Navier-Stokes operator and has been studied extensively using the non-modal analysis introduced in §A.2 for various flow configurations. The onset and amplification of the streaks are modeled as the response to optimal perturbations, including initial perturbations, harmonic forcing and stochastic forcing (Hwang 2011). When the streaks reach a certain amplitude, its presence in the distorted base flow leads to a secondary instability that stabilises or destabilises the base flow. Introducing 3D streamwise vortices and streaks to 2D flows has been used for stability and transition control, in this respect (Choi et al. 2008).

Pujals et al. 2009 computed the optimal transient growth of a parallel and spanwise uniform turbulent flow in a plane channel. The optimal perturbations are counter-rotating streamwise vortices inducing streaks of alternating signs. The optimal amplification of streaks in the Couette flow was computed with respect to the initial conditions, harmonic forcing and stochastic forcing (Hwang and Cossu 2010b). The most amplified spanwise scale is in good agreement with that of the streaks calculated by DNS. Del Guercio et al. 2014 calculated the optimal perturbations in a parallel wake. The streamwise vortices and

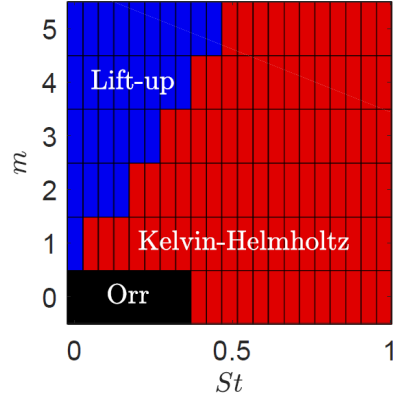


Figure 5.3: Dominant linear instability mechanisms in the space of frequency and azimuthal wavenumber at Mach number 0.4 (figure taken from Pickering et al. 2020).

streaks of sinuous and varicose shape are identified as the most amplified perturbations. To investigate if the optimal perturbations can suppress the absolute instability, DNS was conducted on the base flow superposed with these perturbations of finite amplitudes. Both the sinuous and varicose structures reduce the maximal growth rate, and can suppress the absolute instability at a sufficient amplitude. Marant and Cossu 2018 performed similar transient growth calculations for a parallel plane shear layer to study the influence of finite-amplitude streaks on the Kelvin-Helmholtz instability. It was found that sinuous streak structures have a stabilising effect, whereas varicose structures destabilise the Kelvin-Helmholtz eigenmode over certain parameter regimes.

In this chapter, we study the streaks in parallel round jets following the same procedure as the work cited above. The streamwise vortices and streaks in jets are calculated as optimal perturbations of the largest transient growth. These perturbations structures are imposed on the round jets with a finite amplitude. Nonlinear timestepping is carried out to let the distorted streaky base flow develop before linear stability analysis conducted on the frozen base flow. The first step consisting of calculating optimal perturbations in round jets has already been done by Jiménez-González and Brancher 2017, yet our approach based on an eigenvalue decomposition in §A.2.1 allows to identify not only the most amplified optimal mode, but also the suboptimal modes.

5.1.3 Linear instability mechanisms in jets

It is important to note that the streaks and the associated lift-up mechanism is only one of the instability mechanisms in jets. Pickering et al. 2020 summarized the three main linear mechanisms in jets as the Kelvin-Helmholtz (KH) instability, the Orr mechanism and the lift-up effect. The dominant mechanism at different temporal frequencies and azimuthal wavenumbers are identified according to the SPOD and the resolvent modes, as shown in figure 5.3. We briefly explain here these three mechanisms by referring to the work of Pickering et al. 2020.

The *KH* instability in jets takes form of a convectively unstable eigenmode of a parallel or quasi-parallel shear layer. In resolvent analysis, the KH instability is characterized by the optimal response mode in the range of large gain separations against the suboptimal modes, for $St \in [0.3, 1]$ (Garnaud et al. 2013b; Lesshafft et al. 2019). In Pickering et al. 2020, the optimal velocity response at $St = 0.6$ has similar amplitudes in all the three directions and the amplitude of corresponding forcing rapidly decreases at the nozzle exits.

A resolvent-based structural sensitivity is introduced, showing the overlap between forcing and response on different flow directions (Qadri and Schmid 2017). These sensitivity structures are concentrated upstream along the lip line. The sensitivity of streamwise velocity response to streamwise and radial velocity forcing is approximately at the same magnitude.

The *Orr* mechanism refers to the optimal response of the jet in the context of nonmodal analysis in a global framework. The optimal forcing structures are oriented 45° against the mean shear. It takes place at lower frequency $St < 0.3$. In Pickering et al. 2020, the forcing structures gradually increase downstream from the nozzle, opposite to those in the *KH* instability. The sensitivity of streamwise velocity response to streamwise velocity is dominant, with respect to the velocity forcing in other directions. In §2, the optimal forcing structures are also oriented 45° against the mean shear, for the forcing both with velocity and fuel mass fraction. But we believe the Orr mechanism in that slot flame has little impact, because the magnitude of velocity response grows little downstream.

The *lift-up* mechanism takes place at further lower frequencies for non-zero azimuthal numbers. In the optimal response, the magnitude of streamwise perturbations is nearly an order of magnitude higher than that of the two other directions, indicative of the strong presence of streaks in the streamwise directions. The amplitude of forcing structures in the radial and azimuthal directions is at least an order of magnitude larger than those in the streamwise directions, showing the optimal forcing structures take the form of streamwise vortices. The streamwise velocity response is found to be more sensitive to the radial velocity forcing than that of the streamwise, in contrast to the optimal mode identified as the Orr mechanism at higher frequencies.

The streamwise vortices and streaks in Pickering et al. 2020 are identified as optimal forcing and the associated response via the resolvent analysis, that is the frequency approach in §A.2.2. In this chapter, we consider those structures as optimal perturbations, more precisely, the streamwise vortices as optimal perturbations leading to the largest growth of streaks, so it belongs to the temporal approach in §A.2.1. Different from Pickering et al. 2020 who carried out their analysis in a 3D non-parallel framework, we study a 2D parallel round jets with 3D velocity components. The parallel jet assumption is necessary in our study in order to restrict the number of parameters, and to arrive at generic conclusions that are independent of the many parameters that influence the dynamics of a concrete jet configuration, such as the nozzle condition and turbulent viscosity. This also allows a detailed discussion of convective and absolute instability, in the following paper (Wang et al. 2021).

5.2 Paper: The effect of streaks on the instability of jets

The effect of streaks on the instability of jets

Chuhan Wang¹, Lutz Lesshafft¹, André V.G. Cavalieri², Peter Jordan³

¹Laboratoire d’Hydrodynamique, CNRS / Ecole Polytechnique / Institut Polytechnique de Paris, Palaiseau, France

²Instituto Tecnológico de Aeronáutica, São José dos Campos, Brazil

³Institut Pprime, CNRS / Université de Poitiers / ENSMA, Poitiers, France

Received 2 June 2020; revised 15 September 2020; accepted 27 October 2020

Abstract

The presence of elongated streaks of high and low streamwise velocity in the shear layer of circular jets breaks the axisymmetry of their steady-state solution. If the streaks are considered to be part of the base flow, for the purpose of linear instability analysis, the instability eigenmodes are thus affected by their presence. The resulting changes of growth rate and spatial shapes of eigenmodes, related to the shear instability in jets, are investigated here for parallel base flows. Optimal streamwise vortices (“rolls”) with prescribed azimuthal periodicity are computed, such that the transient temporal growth of the streaks that they produce is maximal. The presence of finite-amplitude streaks requires the formulation of eigenvalue problems in a two-dimensional cross-plane. Sinuous rolls and streaks are found to have a stabilising effect on the Kelvin-Helmholtz instability, whereas the varicose rolls and streaks have a destabilising effect. Absolute instability is not found to occur. This work shows that the effects of rolls and streaks need to be taken into account for more precise modelling of jet instability.

Keywords— jets, absolute/convective instability

5.2.1 Introduction

Rolls and streaks, and their role in instability dynamics and laminar-turbulent transition, have been extensively studied in the context of wall-bounded shear flows (Butler and Farrell 1992; Jiménez 2013). *Rolls*, defined as vortices in the cross-plane of the flow, transport high-speed fluid towards the wall and low-speed fluid away from the wall, thereby creating *streaks* in the main flow velocity (“lift-up effect”; Landahl 1975). These streaks are themselves subject to instabilities (Park et al. 2011), and are even assumed to play a central role in the self-sustained process of wall-bounded turbulence (Waleffe 1997; Hwang and Cossu 2010a). However, the very presence of rolls and streaks in *free* shear flows such as jets has seldom been recognised until recently. Nogueira et al. 2019 documented the appearance of streaky structures in the turbulent velocity field of a high-speed jet, by processing particle image velocimetry data with spectral proper orthogonal decomposition. A linear analysis of the mean flow confirmed that the transient growth of these structures is caused by the lift-up effect. Pickering et al. 2020 investigated the formation of streaks in developing jets, obtained from large-eddy simulation, in response to harmonic forcing

input, concluding that streaks may be expected to dominate perturbations in jets at low frequencies.

A linear analysis of the growth of streaks in round jets was conducted by Jiménez-González and Brancher 2017, who computed optimal initial conditions for transient energy growth. These were found to take the shape of rolls, leading to the creation of streaks. Marant and Cossu 2018 performed similar transient growth calculations for a parallel plane shear layer. Those authors then went on to characterise the influence of finite-amplitude streaks on the linear Kelvin–Helmholtz instability. It was found that “sinuous” streak structures have a stabilising effect, whereas “varicose” structures destabilise the Kelvin–Helmholtz eigenmode over certain parameter regimes. A similar analysis of wake flows was conducted by Del Guercio et al. 2014, where the situation was found to be different: both the sinuous and varicose structures reduce the maximal growth rate, and the varicose streaks have a more stabilising effect than sinuous streaks of the same amplitude. A *quadratic* variation of the eigenvalues with respect to the streak amplitude was found in both of these works, consistent with results from a second-order sensitivity analysis.

On the basis of these recent studies, the present article investigates how the presence of rolls and streaks modifies the linear instability characteristics of round jets. The scope and study programme are quite similar to the plane shear-layer investigation of Marant and Cossu 2018. As streaks in turbulent jets are well modelled using a transient growth analysis (Nogueira et al. 2019), we evaluate here how optimal rolls and streaks, obtained with a similar procedure, affect the Kelvin–Helmholtz mechanism in jets, which is relevant for understanding the interplay between streaks and the well-documented wavepackets in jets (Jordan and Colonius 2013; Cavalieri et al. 2019). Differently from (Marant and Cossu 2018), the curvature of a jet shear layer induces self-interaction effects, and in particular “jet-column” dynamics, which scale with the jet diameter and are absent in single plane shear layers. Jet-column dynamics are similar to the interaction dynamics between the two shear layers that form a plane jet or wake; the absolute mode in round jets without counterflow is of the jet-column type (Lesshafft and Huerre 2007). While our present study considers only streamwise-invariant base flow settings, the role of streaks in jets is not limited to these. For instance, streak structures have been observed to appear prominently in the braid regions between convecting ring vortices, as shown most recently in the experiments of Kantharaju et al. 2020 and in the optimal perturbation analysis of Nastro et al. 2020.

The paper is organised as follows. In §5.2.2, linearly optimal roll structures are computed, consistent with Jiménez-González and Brancher 2017, that maximise the transient temporal growth of streaks in an axisymmetric jet base flow. The nonlinear flow development, in the presence of finite-amplitude rolls, is then simulated in time. In §5.2.3, frozen instances of streaky parallel jets, obtained in this way, are taken as base flows for linear stability analysis, and the sensitivity of temporal eigenmodes with respect to rolls and streaks is discussed. The maximum temporal mode as well as the absolute growth rate in jets distorted by rolls and streaks are investigated. Conclusions and perspectives are given in §5.2.4.

5.2.2 Evolution of rolls and streaks in a parallel jet

We seek roll structures that lead to the fastest growth of streaks in a parallel and initially axisymmetric jet (Jiménez-González and Brancher 2017). The initial velocity in the streamwise z direction is given by the usual profile of Michalke 1971:

$$W(r) = \frac{1}{2} + \frac{1}{2} \tanh \left[\frac{1}{4b} \left(\frac{1}{r} - r \right) \right], \quad (5.1)$$

where b represents the non-dimensional momentum shear-layer thickness and r the radial coordinate. The profile, as all quantities in what follows, is scaled with respect to the jet radius R and the centreline velocity W_c . The viscosity ν of an incompressible fluid is characterised by the Reynolds number, $\text{Re} = W_c R / \nu$. Values $\text{Re} = 10^4$ and $b = \frac{1}{20}$ are used throughout this study.

We define *rolls* as a set of counter-rotating vortices in the cross-stream plane, with radial and azimuthal velocity components $u_r(r, \theta)$ and $u_\theta(r, \theta)$, where θ is the azimuthal coordinate. Through convection, the rolls distort the axisymmetric profile (5.1), such that the streamwise velocity changes in time as $W(r) + u_z(r, \theta, t)$. The perturbation u_z represents the *streaks*. As we limit all following instability analysis to streamwise-invariant base flows, rolls and streaks are assumed to be independent of the streamwise coordinate z .

It is to be clarified at this point that the computation of optimal initial conditions for the transient growth of streaks is not the focus of this study, but only a necessary step for the following instability analysis of streaky base flows. The transient growth scenario over short and long time horizons has been amply documented by Jiménez-González and Brancher 2017. Furthermore, in accordance with that work as well as with Marant and Cossu 2018 and the connected studies cited in §5.2.1, we deliberately stay within the classical assumption of a streamwise-invariant base flow (including the rolls and streaks), in order to provide a first characterisation of the effect of streaks on the shear instability in round jets. This choice allows us to restrict the number of parameters, and to arrive at general conclusions from local instability analysis. It is hoped that these will be beneficial for the future analysis of non-parallel streaky jet base flows, which will necessitate a three-dimensional global framework, including nozzle conditions and justifications for turbulent mean flow modelling.

5.2.2.1 Optimisation in the linear limit

Following the approach of Jiménez-González and Brancher 2017 and Marant and Cossu 2018, and references therein, optimal roll shapes for streak generation are sought in the linear limit of small velocities $(u_r, u_\theta, u_z) \ll 1$. The number of rolls and streaks around the azimuth is prescribed by an azimuthal wavenumber m , such that the variations of u_r , u_θ and u_z in θ are given by a factor $e^{im\theta}$. In the following, we refer to m as the “streak wavenumber”.

For a given value of m , temporal eigenmodes of the axisymmetric profile (5.1) are computed, under the restriction of z -invariance (zero axial wavenumber). These computations are performed in polar coordinates, such that only the radial coordinate is discretised via Chebyshev collocation (Lesshafft and Huerre 2007), and non-oscillatory eigenmodes (in time) are recovered. The full spectrum of these eigenmodes, which satisfy the incompressibility condition of zero velocity divergence, is then used as a non-orthogonal basis for the optimisation of transient perturbation growth.

The optimal rolls and streaks are identified such that their kinetic energy is maximised in a linear framework. For a perturbation $\mathbf{u}(r, m, t)$, the initial perturbation $\mathbf{u}_0 = \mathbf{u}(r, m, t = 0)$ is sought such that the quotient

$$\sigma^2 = \frac{\|\mathbf{u}(T)\|^2}{\|\mathbf{u}_0\|^2} \quad (5.2)$$

is maximised, where T is a prescribed finite evolution time. The norm is defined as $\|\mathbf{u}\|^2 = \int_0^{r_{max}} (|u_r|^2 + |u_\theta|^2 + |u_z|^2) r dr$, where r_{max} denotes the maximal radial coordinate in the computation domain. An orthogonal set of optimal and suboptimal initial perturbations

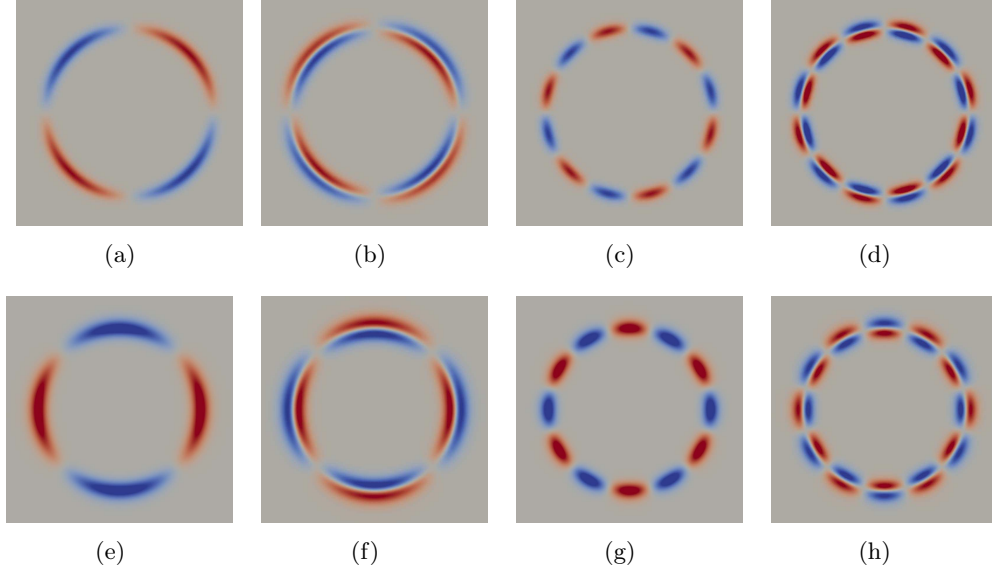


Figure 5.4: Optimal (a,c,e,g) and first suboptimal (b,d,f,h) linear rolls and streaks for streak wavenumbers $m = 2$ (a,b,e,f) and $m = 6$ (c,d,g,h). Top row: streamwise perturbation vorticity (rolls) at $t = 0$; bottom row: streamwise perturbation velocity (streaks) at $t = T = 1$. Red colour is positive, blue colour is negative.

\mathbf{u}_0 can then be obtained by singular value decomposition (Schmid and Henningson 2001). All three components of perturbation velocity are included in the norms in (5.2), which means that the energies of both rolls and streaks are taken into account.

Identical optimal structures as shown by Jiménez-González and Brancher 2017 are recovered, for the same base flow (5.1) and the same gain definition (5.2), characterised by roll structures in the initial condition \mathbf{u}_0 (vorticity in the cross-plane), which give rise to streaks in $\mathbf{u}(T)$ (axial velocity). These structures, obtained over a time horizon $T = 1$, are presented in figure 5.4 for $m = 2$ and $m = 6$. Note that the shapes of these rolls and streaks are insensitive to the choice of sufficiently short time horizons, so that $T = 0.1$ or $T = 10$ give practically identical results for the optimal initial condition. According to Jiménez-González and Brancher 2017, viscous decay of rolls and streaks becomes important at time scales $T = O(1000)$, much larger than the turbulent coherence scales in the jet flows that motivate the present study.

While Jiménez-González and Brancher 2017 computed, through direct-adjoint looping, the *optimal* initial conditions that lead to the highest gain, the present singular value decomposition technique also allows us to recover the following *suboptimal*s. The optimal and first suboptimal initial perturbations for both example values of m are shown in figure 5.4; in analogy with the plane shear-layer results of Marant and Cossu 2018, we refer to the optimal structures in subfigures (a,c,e,g) as “sinuous”, and to the first suboptimal ones in subfigures (b,d,f,h) as “varicose”. Subsequent suboptimal structures are characterised by an increasing number of radial oscillations.

5.2.2.2 Nonlinear time stepping

In the following simulations, optimal and suboptimal initial conditions (u_r, u_θ) are projected onto a two-dimensional Cartesian mesh in the (x, y) cross-plane, and are added with a finite amplitude to the initially axisymmetric streamwise base flow velocity pro-

file (5.1). This perturbed base flow is then advanced in time, according to the complete nonlinear Navier-Stokes equations for incompressible flow,

$$\partial_t \mathbf{u} + (\mathbf{u} \cdot \nabla) \mathbf{u} = -\nabla p + Re^{-1} \nabla^2 \mathbf{u}, \quad (5.3)$$

$$\nabla \cdot \mathbf{u} = 0, \quad (5.4)$$

expressed in Cartesian velocity components. Finite elements, provided by the FEniCS library (Logg and Wells 2010), are used to discretise these equations in the (x, y) plane, and time stepping is performed by use of the Crank-Nicolson method. The velocity components in these Cartesian calculations are denoted $\mathbf{u} = (U, V, W)$.

Example results from these simulations, with $m = 6$, are shown in figure 5.5: the first case (top row) develops from a sinuous initial condition; the second case (bottom row) starts from a varicose one. The jet deformation due to the sinuous perturbation is more apparent, and reminiscent of the profile shapes of jets from corrugated nozzles (Lajús et al. 2019). While the sinuous rolls mostly lead to azimuthal variations of the radial position of the shear layer, the varicose rolls lead to a thickening and thinning of the shear layer at different azimuthal positions. These effects correspond to the parameters R and Θ , respectively, of the velocity profiles in Lajús et al. 2019.

To quantify the intensity of rolls and streaks, their amplitudes A_r and A_s are defined in the same way as in Marant and Cossu 2018 and references therein:

$$A_s(t) = \frac{1}{2 \max_{x,y}(W_b)} \left(\max_{x,y}[W(t) - W(0)] - \min_{x,y}[W(t) - W(0)] \right), \quad (5.5)$$

and

$$A_r(t) = \frac{1}{4 \max_{x,y}(W_b)} \left(\max_{x,y}[U(t)] + \max_{x,y}[V(t)] - \min_{x,y}[U(t)] - \min_{x,y}[V(t)] \right). \quad (5.6)$$

The growth of streak amplitude, caused by sinuous and varicose rolls, is shown in figure 5.6: these computations are initialised with rolls of amplitude $1\% \leq A_r \leq 3\%$, and the streak wavenumber is again chosen as $m = 6$. The streak amplitude, which initially is zero, is found to increase approximately linearly in time, and the linear growth rate in the initial stage scales with the roll amplitude. The amplitude growth of varicose streaks is slower. As the rolls experience viscous dissipation, their amplitude $A_r(t)$ decreases slowly in time. Note that in our parallel-flow setting, rolls generate streaks, but streaks have no influence on rolls, even in the nonlinear regime. Therefore, the roll amplitude may be set as an initial condition parameter, whereas the streak amplitude is simply a function of time in the base flow evolution. The streak amplitude is then chosen as a parameter instead of evolution time, because it indicates more directly the intensity of the jet deformation. Snapshots of these time-evolving streaky jets, characterised by the values of m , A_r and A_s , and by their sinuous or varicose symmetry, are now taken as base flows for the purpose of linear stability analysis.

5.2.3 Linear stability analysis

Linear stability analysis is carried out in Cartesian coordinates (x, y, z) . Velocity perturbations (u'_x, u'_y, u'_z) and pressure p' are assumed to take the form of normal modes $[u'_x, u'_y, u'_z, p'](x, y, t) = [u_x(x, y), u_y(x, y), u_z(x, y), p(x, y)] \exp(-i\omega t + ikz)$. The linear perturbation equations are

$$-i\omega u_x + U \partial_x u_x + \partial_x U u_x + V \partial_y u_x + \partial_y U u_y + ikW u_x + \partial_x p - Re^{-1}(\partial_{xx} u_x + \partial_{yy} u_x - k^2 u_x) = 0, \quad (5.7)$$

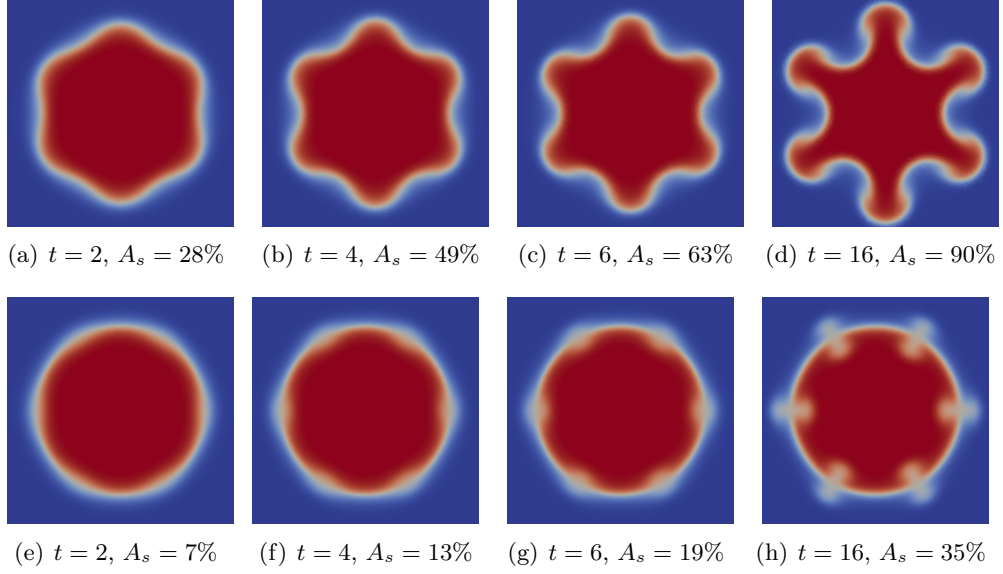


Figure 5.5: Nonlinear time evolution of $m = 6$ streaks in jets: streamwise velocity. (a, b, c, d) Sinuous rolls as initial condition (see figure 1g); (e, f, g, h) varicose rolls as initial condition (see figure 1h). Both cases start from initial roll perturbations with amplitude $A_r(t = 0) = 3\%$, as defined in (5.5).

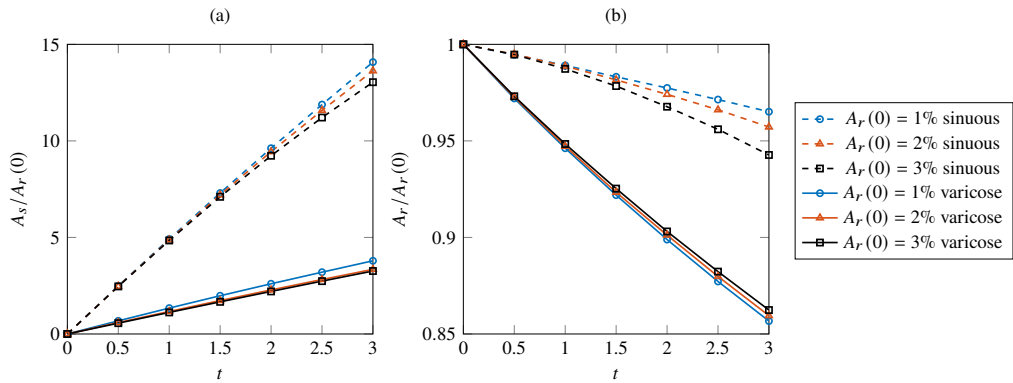


Figure 5.6: Time evolution of the streak amplitude $A_s(t)$ and the roll amplitude $A_r(t)$, both normalised by $A_r(0)$, with sinuous and varicose rolls of $m = 6$ as initial perturbations of amplitude $A_r(0) = 1\%, 2\%, 3\%$.

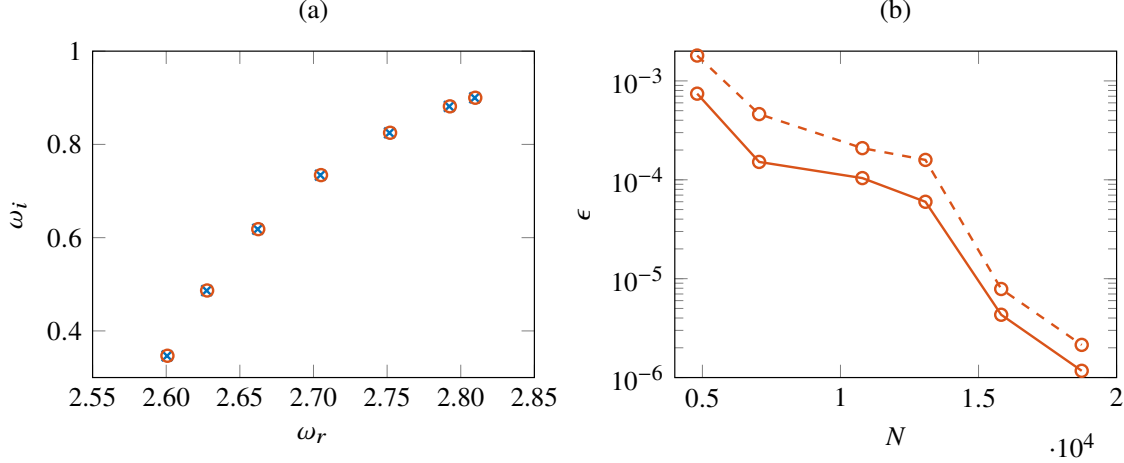


Figure 5.7: Validation and mesh convergence of the linear stability results computed in the (x, y) plane. Eigenmodes with streamwise wavenumber $k = 5$ of an axisymmetric base flow (5.1) are shown. (a) Validation against a polar formulation, where only the radial coordinate is discretised: the seven leading eigenmodes ($n = 0, \dots, 6$) computed in the (x, y) plane (\circ) and in polar coordinates (\times). (b) Relative error ϵ of the growth rate ω_i (solid line) and the frequency ω_r (dashed line) of the $n = 0$ eigenmode, as a function of the number of grid points N in the (x, y) plane. Results for $N = 22041$ are taken as reference.

$$-i\omega u_y + U\partial_x u_y + \partial_x V u_x + V\partial_y u_y + \partial_y V u_y + ikW u_y + \partial_y p - Re^{-1}(\partial_{xx} u_y + \partial_{yy} u_y - k^2 u_y) = 0, \quad (5.8)$$

$$-i\omega u_z + U\partial_x u_z + \partial_x W u_x + V\partial_y u_z + \partial_y W u_y + ikW u_z + ikp - Re^{-1}(\partial_{xx} u_z + \partial_{yy} u_z - k^2 u_z) = 0, \quad (5.9)$$

$$\partial_x u_x + \partial_y u_y + ik u_z = 0. \quad (5.10)$$

Finite-element discretisation is applied by use of the FEniCS library on a two-dimensional mesh in the (x, y) plane. Second- and first-order Lagrangian elements are used to discretise perturbation velocity and pressure, respectively. The discretised equations are assembled as an eigenvalue problem $\mathcal{A}\mathbf{q} = \omega\mathcal{B}\mathbf{q}$, where the eigenvalues ω and the associated eigenvectors $\mathbf{q} = (u_x, u_y, u_z, p)$ for a fixed k are computed via the Arnoldi algorithm. Eigenvalue calculations on the two-dimensional (x, y) mesh have been validated against the one-dimensional polar formulation used in §5.2.2.1, discretised only in r , for a strictly axisymmetric base flow. For a wavenumber $k = 5$, the seven most unstable eigenmodes are compared in figure 5.7(a), and excellent agreement is found between these two different formulations. Grid convergence is then examined to determine the required number of grid points N in the (x, y) plane, to be used for linear stability analysis. Real and imaginary parts of the dominant eigenvalue ($n = 0, k = 5$) are tracked. The eigenvalue obtained with the largest number of points ($N = 22041$) is taken as reference, and the relative error ϵ , as a function of N , with respect to this reference value is presented in figure 5.7(b). A number of $N = 15821$ grid points is deemed satisfactory, giving convergence within five significant digits, and is kept for the following computations. As nomenclature, we define the temporal growth rate as $\omega_i = \Im[\omega]$ and the frequency as $\omega_r = \Re[\omega]$. We denote the azimuthal wavenumber of eigenmodes n , so as to distinguish it from the streak wavenumber m , which characterises the azimuthal periodicity of the streaky base flow.

5.2.3.1 Linear sensitivity analysis

In the limit of infinitesimal base flow modifications, the effect of streaks on instability eigenvalues (growth rate and frequency) can be predicted by way of sensitivity analysis

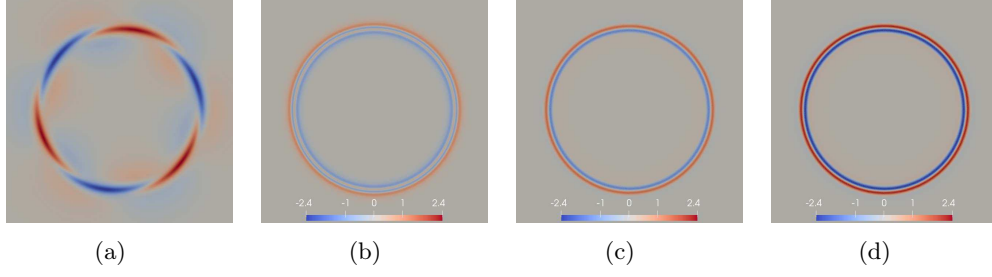


Figure 5.8: First-order sensitivity of the growth rate with respect to base flow modifications: (a) an instability eigenmode ($n = 3$, $k = 5$) of the axisymmetric base flow (axial velocity); associated sensitivity with respect to (b) radial velocity, (c) azimuthal velocity and (d) streamwise velocity changes in the base flow.

(Hill 1992; Marquet et al. 2008). In the context of streaks in plane shear layers, Marant and Cossu 2018 demonstrated that this analysis needs to be expanded to second order, if one wishes to correctly retrieve the quadratic dependency of eigenmodes on streak amplitude. The same observation had been reported before from studies of instability control in plane two-dimensional flows via spanwise-periodic base flow modifications (Hwang and Choi 2006; Tammisola et al. 2014; Boujo et al. 2019). If, however, in the present configuration, rolls and streaks in jets cause first-order variations in the instability eigenvalues, then a sensitivity analysis will allow us to identify roll shapes that optimally destabilise linear eigenmodes.

A given base flow variation $\delta\mathbf{Q} = (\delta U_r, \delta U_\theta, \delta U_z)$ induces a variation $\delta\mathcal{A}$ of the matrix of the linearised Navier-Stokes operator. The resulting first-order variation $\delta\omega$ of the eigenvalue associated with a direct eigenvector \mathbf{q} and an adjoint eigenvector \mathbf{q}^+ (appropriately normalised; see Chomaz 2005 for details) is given by

$$\delta\omega = \mathbf{q}^{+\text{H}} \delta\mathcal{A} \mathbf{q} = \mathbf{s}^{\text{H}} \mathcal{M} \delta\mathbf{Q}. \quad (5.11)$$

The superscript H denotes the transpose conjugate, the matrix \mathcal{M} contains mesh-dependent quadrature coefficients for a scalar product and \mathbf{s} is the base flow sensitivity field (nomenclature as in Lesshafft and Marquet 2010). The effect of a given base flow variation $\delta\mathbf{Q}$ on the eigenvalue is given by its projection onto the sensitivity field; consequently, if we restrict the norm of $\delta\mathbf{Q}$ to a fixed value, its *optimal shape* for maximum destabilisation of an eigenmode is given by the imaginary part of the associated \mathbf{s} .

Such a sensitivity field (imaginary part) is shown in figure 5.8, for an eigenmode with wavenumbers ($n = 3$, $k = 5$) in an axisymmetric (non-streaky) base flow. It can be seen that, at first order, the temporal growth rate is only sensitive to changes in the shear. All components of the sensitivity are found to be axisymmetric, although the underlying eigenmode is not. This result, consistent with the shear layer and wake studies cited above, indicates that rolls and streaks, here defined as non-axisymmetric base flow modifications with zero mean along the azimuth, can only have a second-order effect, but not a first-order effect, on the eigenmodes. Optimisation could be performed on the second-order sensitivity operator to identify azimuthally non-uniform base flow modifications for maximum change of an eigenmode (Boujo et al. 2015, 2019).

5.2.3.2 Linear stability of finite-amplitude streaky jets

Linear stability analysis is now carried out to identify the temporal growth rate ω_i of eigenvalues in frozen instances of streaky base flows. For illustrative purposes, the effect

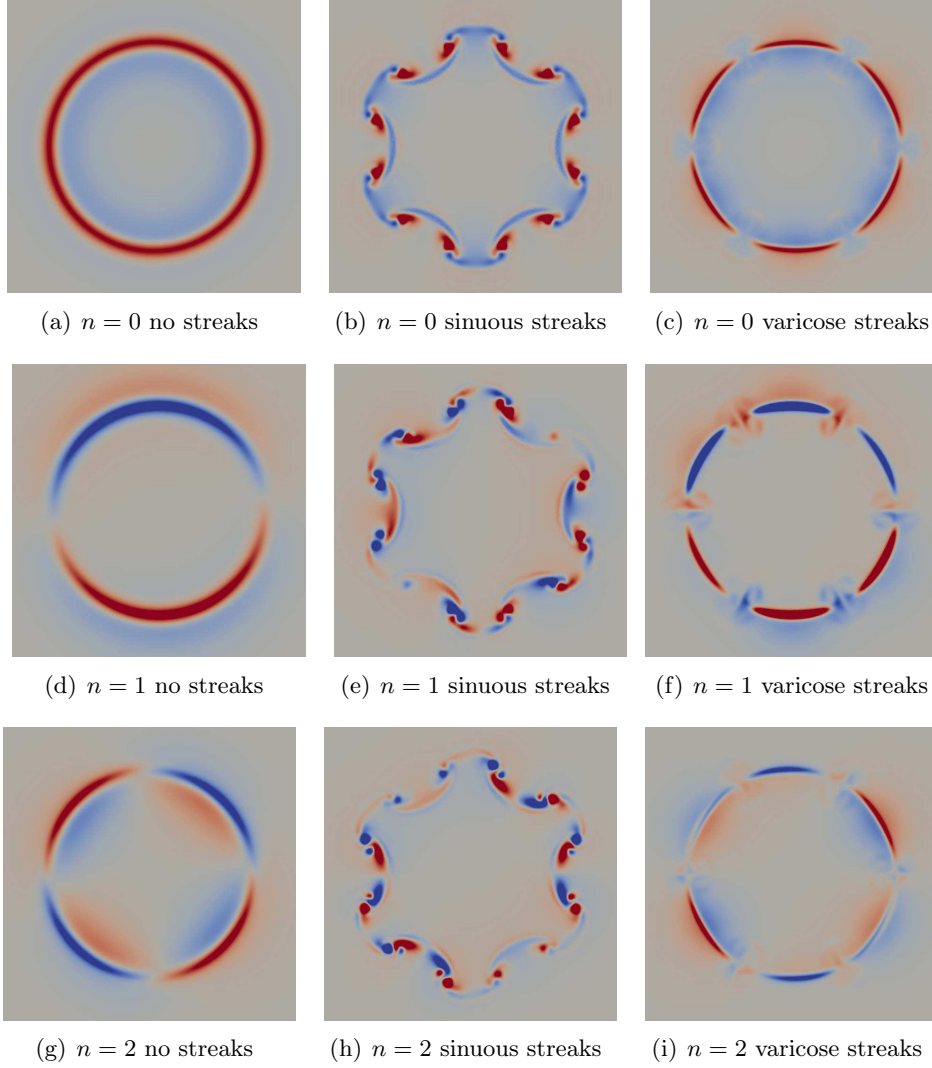


Figure 5.9: Eigenmodes ($n = 0, 1, 2$ and $k = 5$) of axisymmetric and streaky jets, with streak wavenumber $m = 6$. Sinuous case: $A_r = 10\%$, $A_s = 40\%$; varicose case: $A_r = 10\%$, $A_s = 51\%$. Streamwise velocity is shown.

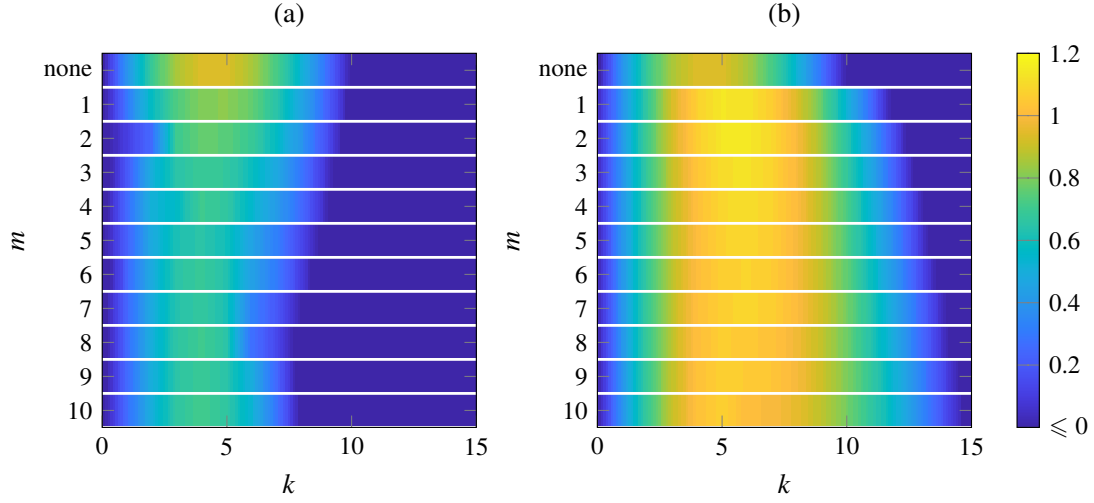


Figure 5.10: Temporal growth rate ω_i as a function of k and m for $A_r = A_s = 5\%$. Only positive (unstable) values are represented. The first row with label “none” represents the growth rate found for the axisymmetric base flow without streaks. (a) Sinuous rolls/streaks. (b) Varicose rolls/streaks.

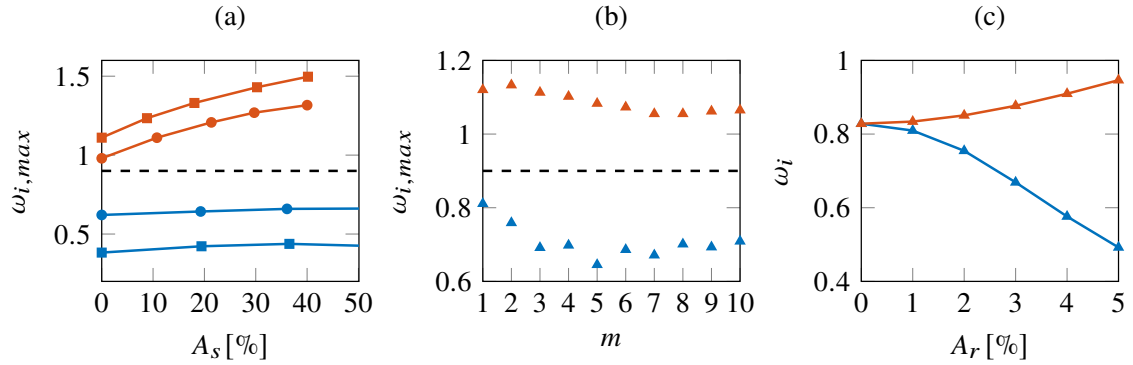


Figure 5.11: Parameter studies of the temporal growth rate ω_i . Blue and red symbols represent sinuous and varicose variations of the base flow, respectively. The temporal growth of the purely axisymmetric jet is shown for comparison (dashed line). Maximum growth rate $\omega_{i,max}$ (a) as a function of streak amplitude $A_s(t)$ for $m = 6$ and $A_r(0) = 5\%$ (circle), 10% (square). (b) as a function of streak number m for the most destabilising k for $A_r = 5\%$ and $A_s = 5\%$. (c) Growth rate ω_i as a function of A_r for $m = 6$, $k = 6$ and $A_s = 0$. The initially axisymmetric ($n = 0$) eigenmode is tracked in (c).

of rolls and streaks on the shapes of some eigenmode shapes is shown in figure 5.9: basic eigenmodes in the axisymmetric case, with azimuthal wavenumbers $n = 0, 1$ and 2 , have been continuously tracked towards high amplitudes A_r and A_s in base flows with sinuous and with varicose roll and streak structures. In the caption, we extend the use of n to the high-amplitude cases in this loose sense of mode tracking, fully aware that the implied symmetries are not strictly preserved in these cases (see the detailed discussion of mode tracking in Lajús et al. 2019).

Systematic variations of the dominant temporal growth rate ($n = 0$) over streamwise wavenumber k are represented in figure 5.10. Amplitudes $A_r = A_s = 5\%$ are fixed, and instability growth rates are plotted for streak wavenumbers $m = 1, \dots, 10$. The range of unstable wavenumbers is narrowed in the presence of sinuous streaks, but largely widened for cases with varicose streaks.

In figure 5.11(a), the maximum ω_i over all streamwise wavenumbers k , denoted as $\omega_{i,max}$, is presented as a function of $A_s(t)$. The sinuous perturbations, decreasing $\omega_{i,max}$, have a stabilising effect, whereas the varicose perturbations, increasing $\omega_{i,max}$, destabilise the jets. The maximum temporal growth rate of a streaky jet with sinuous perturbations does not strongly change as the streaks gain amplitude, whereas that with varicose perturbations increases monotonically with the streak amplitude. These results are consistent with the findings of Lajús et al. 2019: the sinuous streaks lead to an azimuthal change of the shear layer position (parameter R in (Lajús et al. 2019)), which has little effect on jet stability. In contrast, the varicose streaks lead to azimuthal variations of the shear-layer thickness (parameter Θ in (Lajús et al. 2019)), which has a destabilising effect. While it is tempting to discuss these tendencies on the basis of the azimuthally averaged base flow distortions, Marant and Cossu 2018 and Lajús et al. 2019 have demonstrated that such a discussion is incomplete, because the periodic variations of the base flow contribute to the change of eigenvalues on the same order as their average.

The effect of the streak wavenumber m on $\omega_{i,max}$ is presented in figure 5.11(b) for $A_r = A_s = 5\%$. Over all m studied, the varicose perturbations lead to an increase of temporal growth rate, while the sinuous perturbations always decrease the temporal growth rate. The same qualitative behaviour, as demonstrated here only for $m = 6$, is observed at all values of m , including the special case $m = 1$ (“shift-up” as opposed to “lift-up”; see Jiménez-González and Brancher 2017). In figure 5.11(c), the changes of the temporal growth rate of the dominant $n = 0$ eigenmode as a function of small roll amplitude are tracked. It is found that the growth rate variations are initially quadratic in A_r , which indicates a second-order sensitivity. This is consistent with our findings in §5.2.3.1 that the first-order sensitivity of azimuthally periodic base flow modifications, rolls and streaks, is zero. A quantitative second-order sensitivity analysis is not attempted here, as the result can be expected to be similar to that of Marant and Cossu 2018.

5.2.3.3 Absolute instability of streaky jets

Although the results of our jet study so far display the same trends as revealed by Marant and Cossu 2018 for plane shear layers, the effect of streaks on the *absolute* instability mode in jets deserves to be examined. In jets, the absolute mode is of the *jet-column* type (Lesshafft and Huerre 2007), and therefore physically distinct from the plane shear layer case. In a similar study of parallel wakes, Del Guercio et al. 2014 observed that sinuous as well as varicose spanwise perturbations may reduce the absolute growth rate and even suppress the absolute instability. Brandt et al. 2003 demonstrated a similar stabilising effect of streaks on the absolute mode in a Blasius boundary layer.

For our standard jet base flow, variations of the absolute growth rate $\omega_{0,i}$ (see Huerre

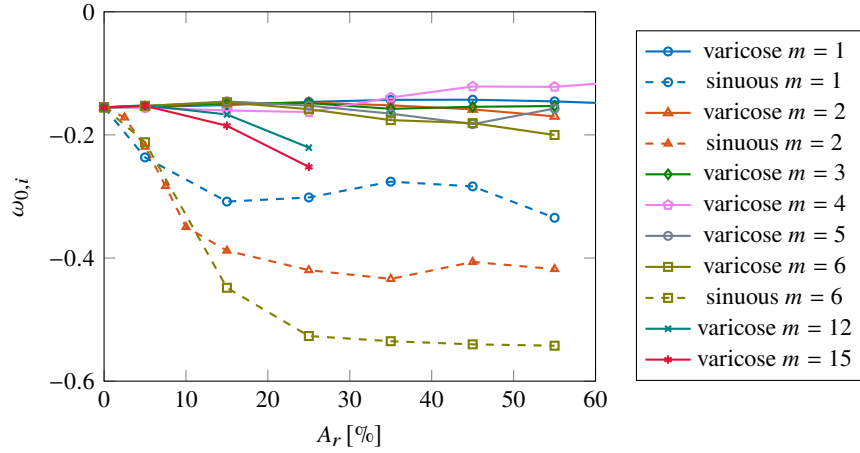


Figure 5.12: Variations of the absolute growth rate $\omega_{0,i}$ with roll amplitude A_r . The streak amplitude A_s is zero.

and Monkewitz 1990) with roll amplitude A_r are shown in figure 5.12. The streak amplitude is set to zero in this example. In the case of varicose perturbations, increasing A_r slightly increases the absolute growth rate $\omega_{0,i}$ for streak wavenumbers $m < 6$, but even a very high roll amplitude does not give rise to absolute instability. Varicose rolls with $m \geq 6$ are seen to decrease $\omega_{0,i}$. Sinuous rolls are found to have a stabilising effect on the absolute growth rate, higher m being more stabilising. Additional computations, not presented here, show that non-zero values of the streak amplitude A_s do not lead to further significant destabilisation of the absolute jet-column mode. In conclusion, a situation where rolls and streaks would give rise to absolute instability in jets could not be identified.

5.2.4 Conclusions

The effect of rolls and streaks on the local instability properties of round jets has been investigated in this work for various control parameters. First, optimal sinuous and varicose rolls and streaks, in the sense of maximal energy growth, have been identified for prescribed numbers of streaks along the azimuth. Optimal and suboptimal rolls and streaks take a form similar to the sinuous and varicose perturbations found in plane mixing layers. In both scenarios, streaks grow within the jet shear layer due to the lift-up mechanism. Sinuous roll structures impart wavy displacements of the shear layer, whereas varicose rolls lead to periodic variations of its thickness. Nonlinear simulations show that rolls evolve slowly in time, only subject to viscous decay, while streaks experience linear amplitude growth in their initial stage.

Linear stability analysis has been performed on frozen instances from nonlinearly evolved streaky jet flows. The observed trends are clear and easily summarised: sinuous rolls and streaks, which themselves represent the fastest-growing transient structures, induce a decrease in the growth rate of Kelvin-Helmholtz instability modes. Varicose rolls and streaks, in contrast, lead to increased instability. The first-order sensitivity of Kelvin-Helmholtz eigenmodes in a non-streaky jet has been computed, and found to be strictly axisymmetric, even for non-axisymmetric mode shapes. Therefore, the effect of low-amplitude rolls and streaks, with zero axisymmetric projection, cannot be explained from such an analysis. Consistent with this result, the variations of instability growth rates with roll amplitude have been shown to be nonlinear, presumably quadratic, analogous to the more detailed sensitivity studies of plane shear flows in the recent literature.

Finally, the absolute growth rate of the axisymmetric jet-column mode in streaky jets

has been examined. Although varicose rolls do lead to a slight destabilisation of this mode, the instability has been found to remain convective over the investigated parameter space. On this basis, the presence of rolls and streaks in jets, although certain to change the quantitative instability properties, is not expected to lead to self-sustained oscillations.

The results from the present investigation lead to the conclusion that the presence of rolls and streaks affects the instability properties of round jets in ways similar to those described by Marant and Cossu 2018 for the setting of plane shear layers. The inclusion of roll structures in the base flow, compared to the roll-free settings of Marant and Cossu 2018, has been found to have a similarly strong, but not qualitatively different effect as the streaks alone. An important limiting assumption in the present study, which is to be relaxed in future work, lies in the restriction to *streamwise-invariant* rolls and streaks. Despite this limitation, the significant modification of Kelvin-Helmholtz instability growth rates clearly indicates that roll and streak perturbations in jets must be accounted for in future modelling of jet instability behaviour.

Acknowledgement

This work has received funding from the Clean Sky 2 Joint Undertaking under the European Unions Horizon 2020 research and innovation programme under grant agreement No 785303. The article reflects only the authors' view, the Joint Undertaking is not responsible for any use that may be made of the information it contains.

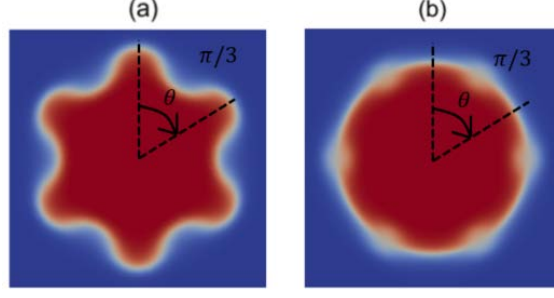


Figure 5.13: Streaky base flows at $t = 6$ taken from 5.5(c)(g) to illustrate the sampling of streamwise velocity profiles.

5.3 Further discussions

The rolls and streaks of sinuous shapes have a stabilizing effect on the jet, whereas those of varicose shapes destabilise the jet. To understand the mechanisms of those instability changes, we try to explore the streamwise velocity profiles of the streaky jets, averaged over all the radial directions. As illustrated in figure 5.13 for streaky base flows at $m = 6$, we uniformly take one hundred azimuthal numbers θ in $[0, \pi/3]$, and along each radial direction r associated with an azimuthal number θ , we interpolate the streamwise velocity $W(r)$. The averaged streamwise velocity profile $W(r)$ over all the sampled directions in $\theta \in [0, \pi/3]$ are shown in figure 5.14(a). To quantitatively assess these velocity profiles, we introduce the non-dimensional momentum thickness θ_t defined as

$$\theta_t = \int_0^\infty u(r) (1 - u(r)) dr. \quad (5.12)$$

The momentum thickness of the axisymmetric round jet profile in (5.1) is 0.05. We trace the evolution of this thickness in the developing streaky base flows with respect to the streak amplitude A_s and time t , as shown in figure 5.15. At $t = 0$, the momentum thickness is 0.05, because there are only rolls in the base flow and the streamwise velocity profile is not affected. With the time developing, the averaged momentum thickness of both sinuous and varicose streaky base flows are found to increase. At the ending time of calculation $t = 16$, the averaged momentum thickness in the sinuous base flow is much higher than the varicose base flow. From this result, we can only conclude that the sinuous perturbations seem to have a strong stabilisation effect by increasing the averaged momentum thickness. The increase of momentum thickness in the base flow with varicose perturbations contradicts with their destabilisation effects.

We further introduce another quantity to characterise these profiles, that is the radial gradient of the streamwise velocity $\frac{dW}{dr}$. This radial gradient associated with the averaged profile in figure 5.14(a) is shown in figure 5.14(b). The peak of the radial gradient at $r = 1$ is slightly larger in the varicose base flow than the axisymmetric base flow, which is relatively consistent with its destabilisation effect observed.

The averaged streamwise velocity profile is only related to the KH instability, because it only depends on the radial direction r . To characterise the changes in azimuthal direction of these velocity profiles, we calculate the momentum thickness θ_t and the maximum velocity gradient $\frac{dW}{dr}$ of *each* sampled velocity profile, and their covariance is shown in table 5.1. The covariance of both θ_t and maximum $\frac{dW}{dr}$ is larger in the varicose base flow than the sinuous one, suggesting that the azimuthal change of velocity profile is stronger in the varicose base flow. Such changes in the azimuthal directions may be the origin of the destabilisation.

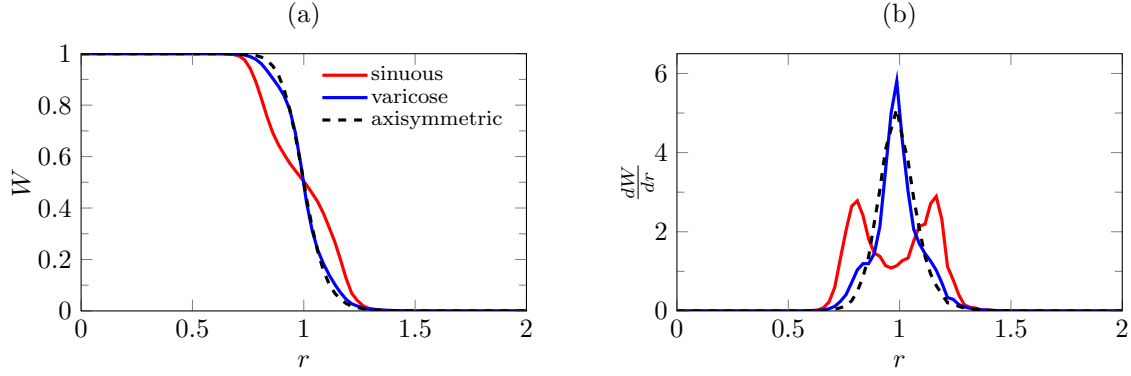


Figure 5.14: The averaged streamwise profile $W(r)$ (a) of streaky base flows in figure 5.13, and the associated radial gradient $\frac{dW}{dr}$ (b).

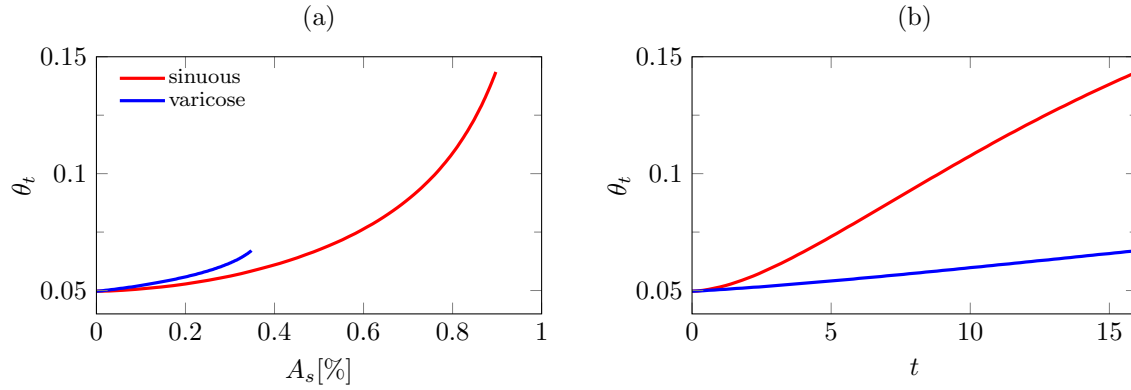


Figure 5.15: Evolution of the averaged momentum thickness θ_t for $m = 6$ with respect to the streak amplitude A_s (a) and calculation time t (b).

Table 5.1: Covariance of momentum thickness θ_t and the maximum of streamwise velocity gradient $\frac{dW}{dr}$ of streaky base flows in figure 5.13 .

	sinuous	varicose
θ_t	12%	26%
$\max[\frac{dW}{dr}]$	20%	34%

In the above analysis of streamwise velocity profiles in streaky base flows, some results seem to be consistent with the stabilisation and destabilisation effect shown by the linear temporal growth rates, but there is no conclusive argument obtained from the effective momentum thickness.

CHAPTER 6

Conclusions and perspectives

Contents

6.1	Summary of the main contributions	94
6.2	Perspectives	96
6.2.1	Closed-loop control of the flame instability based on linearized governing equations	96
6.2.2	Role of chemistry model in linear analysis of turbulent flames . .	97
6.2.3	Impact of conjugate solid-fluid heat transfer on the flame stability	98
6.2.4	Nonlinear nonmodal stability analysis for flames	99

6.1 Summary of the main contributions

The objective of this thesis has been to study the flame instability using the linear stability analysis tool box. The flame instability that we discussed here pertain to small-amplitude fluctuations around a steady base state or a time-averaged mean state. The origin of these perturbations may arise from the interactions and feedback between flame, flow and acoustics. The global linear analysis framework, which has been widely used for the study of shear flows, can take into account all those interactions, because the complete governing equations are discretized in the entire computational domain.

In previous analyses of the non-reacting shear flows, the shear flows are categorized into stable, amplifier-type and oscillator-type. The amplifiers are driven by external perturbations, whereas the oscillator behaviors are intrinsic to the flow system itself. It is natural to extend those notions to the flame, and to understand how linear analysis tools can help in the study of flame instability. Thus, we chose a slot flame as an amplifier-type flame, and a bluff body stabilized flame as an oscillator-type flame.

A novel finite-element code based on the FENiCS framework has been developed to conduct linear analysis with one-step and two-step chemical schemes. The governing equations to describe the flame dynamics, including the conservation equations of momentum, mass, energy and species transport are discretized in two-dimensional Cartesian or cylindrical coordinates. The chemical heat release in the energy equation, and the reaction progress rates in the equations of species transport are linearized and implemented, distinguishing from the codes for non-reacting flows. The standard stability analysis tools of modal and non-modal analysis are implemented, and their mathematical formulations are given in the appendix A.

In §2, the instability of a premixed slot flame that acts as an amplifier has been investigated. That slot flame is globally stable by itself, but it responds to external excitations. Our linear code accurately computed the FTF, with respect to the DNS, with a much lower computational time. An input-output analysis is formulated, which maps the flow response to external forcing inputs, making the resonance peaks in the frequency responses visible. It has been argued that these peaks may correspond to an intrinsic thermoacoustic mode resonance. This input-output formulation answers the question how much energy is required to be injected to the system such that a flow response can be maintained, which provides extra information about the energy that cannot be directly inferred from the FTF. We then investigated where and how the global heat release rate responds to an arbitrary forcing, through introduction of a receptivity vector. Finally, we use the resolvent analysis to isolate the efficient perturbations that determine the unsteadiness of flame. An orthogonal basis of optimal forcing and response structures has been identified, ordered by the efficiency of forcing. Two different input-output norms are investigated, with either the velocity or fuel species as the forcing, while the heat release is taken as the response in both definitions of norm. The optimal mode is found to have a large gain separation with respect to the suboptimal modes, which means there is a unique way to trigger the maximal flame response. From comparing the shape of optimal and suboptimal modes, it has been inferred that the optimal forcing generates flame displacement perturbations that add up constructively. In this way, the perturbations can travel to the flame tip, where the heat release is maximized.

In §3, the instability of a bluff body stabilized flame has been investigated. The flame acts an oscillator that displays self-excited behaviour when the temperature of the bluff body is above 800 K. The linear analysis tools have been demonstrated to well predict the transition and the frequency of oscillations, as it has already been the case for the wake instability behind a circular cylinder in a non-reacting cold flow. By calculating the

eigenmodes from steady base states of different bluff body wall temperatures, we predict that cooling the bluff body can stabilize the flame, which is consistent with nonlinear time-resolved simulations. By calculating the eigenmodes from the time-averaged mean flow at a supercritical bluff wall temperature, we can accurately capture the oscillating frequency with respect to that measured in nonlinear timestepping. The most interesting part of that study would be the identification of the wavemaker regions that drive the instability. Through a decomposition of contributions to the eigenvalue, the wavemaker regions are identified in the wake shear behind the recirculation bubble, and the conservation of momentum equation contributes the most to the eigenvalue. Thus, it is the hydrodynamics that control the global instability of that flame configuration.

We are looking for other configurations of oscillator-type flames whose eigenvalue is not dominantly controlled by the equation of momentum conservation. Thus, in §4 we study a V-shaped flame in a geometry where the thermoacoustic instability is predicted to occur. A branch of unstable eigenmodes has been identified from the steady base state, and the next step is to validate the linear solver and conduct wavemaker analysis with those unstable modes.

A side project of this thesis studies the effect of streaks on the instability of non-reacting jets. Coherent structures have been recently studied in boundary layer flames in both laminar and turbulent regimes, and the presence of streak structures may impact the flame instability. Also very recently, large-scale streaky structures are observed in turbulent jets, so it is very probable that streaks may be present in turbulent flames as well. Before pursuing a configuration of flames with streaks, we intend to carry out a fundamental study of the effect of streaks on the non-reacting jets, in the aspect of jet instability. In §5, rolls and streaks in the sense of optimal perturbations that maximize the growth of rolls and streaks are identified with chosen azimuthal numbers. The optimal and suboptimal rolls and streaks take the form similar to the optimal sinuous and suboptimal varicose perturbations in the mixing layer. Nonlinear timestepping shows that rolls in the shear layers generate streaks whose amplitude grows linearly in an early stage. The sinuous rolls and streaks show a stabilising effect in the sense of decreasing the maximal temporal growth rate. Conversely, rolls and streaks of varicose shapes exhibit a destabilisation effect. Those sinuous and varicose rolls and streaks do not induce absolute instability in jets.

This thesis may be considered a methodology work that demonstrates the utility of linear tools in the study of flame instability, particularly in laminar premixed flames. In the context of amplifier-type flow, linear tools allow fast calculations of FTF, characterization of input-output behaviour, identification of the receptivity to global heat release and calculation of the optimal forcing via resolvent analysis. In the context of oscillator-type flow, linear tools allow to predict the transition and oscillating frequency, and to identify the main region and the main physical mechanisms that drive the instability. Most of the analyses mentioned above have rarely been conducted in the research of flame instability, or conducted via nonlinear timestepping with a considerably higher cost.

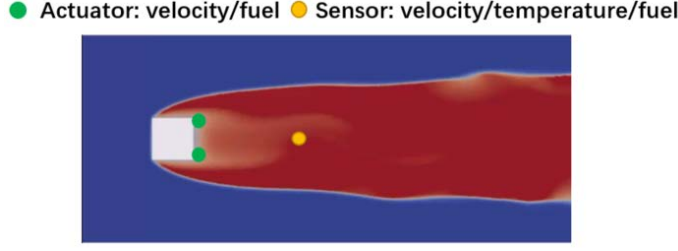


Figure 6.1: Illustration of closed-loop control in the oscillator-type flame.

6.2 Perspectives

6.2.1 Closed-loop control of the flame instability based on linearized governing equations

Open-loop and closed-loop strategies have been applied in the control of flame instability to prevent or mitigate undesirable oscillations in combustion systems (Zhao et al. 2018). The closed-loop strategy consists of implementation of the sensors that measure the reference signal, the actuators that alter the behaviour of the system, and the controllers of optimization algorithm that calculate the command signal of actuators from the measured sensor signal. Closed-loop control of flame instability is often based on the unidimensional equations that describe the thermoacoustic interactions (Dowling and Morgans 2005). The instability occurs when the acoustical energy generated by combustion is higher than the acoustic loss through the boundary. To decrease the acoustical energy generated, the actuators are modulators of injected fuel mass that directly modulate the heat release, and loudspeakers that alter the acoustic frequency selection. In those strategies, the control of instability associated with thermoacoustic interaction is emphasized, but the instability from hydrodynamics is seldom considered into the system modelling process. Other types of actuators are the pistons or plasma actuators that impose a volume forcing and change the velocity inside the flow system (Zhao et al. 2018), which have been frequently used in the non-reacting flows.

In the non-reacting shear flows, direct modelling based on the physical governing equations has already been used as a standard procedure in the closed-loop control of flow unsteadiness (Sipp et al. 2010), either in the context of oscillator-type flow (Barbagallo et al. 2009) or amplifier-type flow (Barbagallo et al. 2012). Without taking into account the noise in the system, the control problem can be formulated in a state-space representation in the form

$$\mathcal{B} \frac{\partial \mathbf{q}'}{\partial t} = \mathcal{L} \mathbf{q}' + \mathcal{C} \mathbf{c}', \quad (6.1)$$

$$\mathbf{w}' = \mathcal{W} \mathbf{q}', \quad (6.2)$$

where \mathbf{c}' is the command signal of the actuator, \mathbf{w}' is the measured signal of the sensor. \mathcal{C} and \mathcal{W} are the transfer matrix of \mathbf{c}' and \mathbf{w}' with respect to the flow state \mathbf{q}' . The modelling of \mathcal{L} is the essential part of system modelling and it may be obtained by direct modelling with the linearized governing equations, as what has always been done throughout this thesis. Further model reduction techniques are required to decrease the degrees of freedom of \mathcal{L} so that a low-dimensional controller can be designed. The model reduction techniques have already been applied for the control problems in non-reacting flows such as combination of global modes (Barbagallo et al. 2009), eigenvalue realisation algorithm (Flinois and Morgans 2016) or identification of frequency response by low-order transfer functions (Jin et al. 2020).

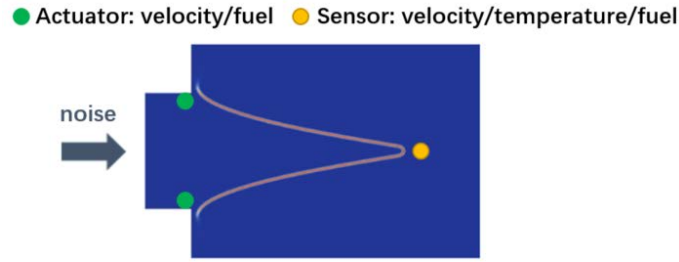


Figure 6.2: Illustration of closed-loop control in the amplifier-type flame.

Above all, it is straightforward to do a closed-loop control of flame oscillations based on a state-space representation via the flow equations. In the same manner as Barbagallo et al. 2009, 2012 for non-reacting flows, the closed-looped control can be considered both for the oscillator- and amplifier-type reacting flows described in this thesis illustrated in figure 6.1 and figure 6.2, respectively. The state-space model can be directly obtained by the linearized flow equations, which have already been proven to be capable of capturing the linear flame dynamics. With respect to the traditional methods mostly concentrating on the thermoacoustic, such modelling would consider the coupling between hydrodynamics and thermoacoustic. Also, based on the physical model including the spatial information on the two-dimensional flow field, this method would help identify the optimal positions of sensors and actuators (for example, by wavemaker analysis in Flinois and Morgans 2016). Control strategies by using different flow quantities, such as velocity, temperature and fuel mass, as measured and forcing signal can be tested.

6.2.2 Role of chemistry model in linear analysis of turbulent flames

As already discussed, in stability analysis, the involvement of the linearized chemistry model is the most important difference with respect to the non-reacting flow. One of the main contributions of this thesis is that adding the linearized chemistry into the governing equations can help accurately capture the dominant frequency of an oscillator and calculate the FTF of an amplifier. The flame configurations that we consider here are in laminar regimes, which provide relatively clean steady base states for linearization. However, the linearization of chemistry scheme is already a considerable numerical challenge even in those laminar flame cases, especially for the two-step chemistry as documented in the appendix of §2. In the turbulent flames, the time-averaged mean states would be more distorted, and the linearization of chemical schemes would appear to be more difficult.

At the end of §3, the passive flame approach for linear analysis was discussed. Such approach does not contain the chemical heat release in the linearized equations, so it considers purely hydrodynamic effects. Our results showed that the passive flame approach failed to capture the oscillation frequency and the temporal growth from the mean flow of that bluff body stabilized flame. However, passive flame approaches have already been successfully used in several studies to capture the unstable mode (Oberleithner et al. 2015a), and to predict the coherent structures (Kaiser et al. 2019a; Douglas et al. 2021) in turbulent flames, sometimes even in excellent agreement with experimental results. Thus, more efforts should be dedicated in a fundamental comprehension of the necessity of linearized chemical scheme in stability analysis. From a theoretical point of view, the global heat rate fluctuation is influenced by the change of flame surface area and the flame speed (Wang et al. 2009). These two effects tune in at sufficiently high forcing frequencies due to the stretch of flame surface, with the heat release rate modulating again the internal flame structure.

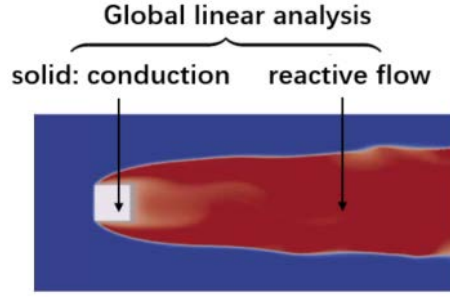


Figure 6.3: Illustration of global linear analysis for a reactive flow with conjugate solid-fluid heat transfer.

Once the chemical heat release is proven to be necessary to be included in the linearized governing equations, a following question is if the chemical schemes can be simplified, for example using a one-step scheme instead of 18-step scheme for a hydrogen combustion. Such a simplification would reduce the number of transport equations to only one transport equation of the fuel, which considerably reduce the dimension of Jacobian matrix. Note that the one-step scheme would only be used for the linear analysis, in other words, the base or mean flow may still be calculated with an 18-step scheme from an external solver. An alternative approach is using the reaction progress variables to replace the detailed chemistry reaction (Douglas 2021), yet the coefficients in the reaction progress variables must be identified consistently to be capable of reproducing the linear dynamics.

6.2.3 Impact of conjugate solid-fluid heat transfer on the flame stability

Thermal boundary conditions of the flame anchoring position can significantly change the flame dynamics (Mejia 2014). In the case of a slot flame, the transfer function of a flame with adiabatic wall condition or isothermal wall condition largely differs from each other (Avdonin et al. 2019). In the calculation of the V-shaped flame in §4, we found that varying the thermal boundary condition could considerably change the flame shape, which had been documented as a transition between V and M shape as a function of the wall temperature in the outer recirculation zone (Guiberti et al. 2015). It would be interesting to see if linear analysis can help study the sensitivity of flame to those thermal boundary conditions.

In §3, the boundary condition of the bluff body wall is isothermal and the transition was found to be controlled by the bluff body wall temperature. However, in the reference calculation of Kedia and Ghoniem 2014, a more realistic boundary condition of conjugate fluid-solid heat transfer is considered. It could be an interesting study to conduct a global stability analysis of that conjugate fluid-solid heat transfer configuration, with linearising the reactive Navier-Stokes equations in the fluid domain, and the heat diffusion equation in the solid domain. This idea is illustrated in figure 6.3. The Jacobian matrix of both subdomains can then be assembled together with an appropriate boundary condition of heat flux. The sensitivity of global instability to the coefficients of heat diffusion and convection, which may characterise the properties of solid material, can be discussed. Recent progress on the linear analysis of fluid-structure interactions (Pfister and Marquet 2020; Negi et al. 2020) could be helpful in the problem formulation, for example, decomposition of the input-output gain to the contributions from solid, fluid, and solid-fluid coupling, respectively (Pfister et al. 2021).

6.2.4 Nonlinear nonmodal stability analysis for flames

An output of this thesis is a linear code to study the flame instability, and it is expected that the linear tools presented can be extended to a large range of flame configurations in laminar and turbulent regimes. However, one should not be obsessed with those linear tools, because inherent nonlinear dynamics play an important role in the flame instability (Noiray et al. 2008).

The nonlinear version of nonmodal analysis could be an appropriate framework for such a discussion, which can be formulated either in the frequency or temporal domain, as it is the case in the linear nonmodal analysis given in §A.2. The additional parameter in nonlinear analysis is the energy of initial perturbations or the external forcing. In the temporal domain, the optimal energy growth associated with the disturbances of a given initial energy and a target time can be calculated through a nonlinear direct-adjoint looping (Cherubini et al. 2011; Kerswell 2018). The target time of the spatial developing flows have to be carefully chosen so that the convected disturbances are still inside the truncated flow region (Kerswell 2018). The nonlinear optimal perturbations identified can be considered as the seeds with minimal energy that lead to the flow transitions. In the frequency domain, the optimal forcing structures of a finite amplitude at given frequencies can be searched (Rigas et al. 2021), which may be understood as a nonlinear version of the resolvent analysis. A similar optimisation procedure to that of the temporal domain can be formulated based on the harmonic-balanced Navier-Stokes equations, which allow the triadic interactions for a forcing with multiple harmonics.

Those nonlinear nonmodal analysis have already been applied in the boundary layers and wall-bounded flows to identify the minimal seeds and various scenarios for turbulent transitions. For other spatial developing flow that we are interested in, the nonmodal analysis carried out in jets (Garnaud et al. 2013b,a) and flames as presented in §2, only considers linear perturbations. Hence, it is a potential direction to include the nonlinear dynamics of jets and flames into their stability analysis, via those nonlinear nonmodal techniques. With respect to the current calculations tools, a direct-adjoint solver is required to be developed. Then, one could start with identifying the nonlinear perturbations in a two-dimensional non-reacting jet and comparing the results with linear analysis, before moving on to the reacting cases.

APPENDIX A

Linear analysis methodologies

The mathematical formulations for linear analysis used in this thesis are presented. At the end of each method description, the configurations where the method is applied in the thesis is referred to.

Contents

A.1	Modal analysis	102
A.1.1	Direct and adjoint modes	102
A.1.2	Wavemaker analysis	103
A.1.3	Sensitivity to base flow modifications	104
A.2	Nonmodal analysis	105
A.2.1	Temporal approach: transient growth	105
A.2.2	Frequency approach: resolvent analysis	106

A.1 Modal analysis

A.1.1 Direct and adjoint modes

Consider the Navier-Stokes equations written in the form

$$\mathcal{B} \frac{\partial \mathbf{q}}{\partial t} = \mathcal{NS}(\mathbf{q}), \quad (\text{A.1})$$

where $\mathbf{q}(\mathbf{x}, t)$ is the state vector as a function of spatial coordinates \mathbf{x} and time t . In the incompressible case, the state vector is simply $\mathbf{q} = [\mathbf{u}, p]$ in which \mathbf{u} is velocity and p is pressure. \mathcal{NS} represents the nonlinear operator of the Navier-Stokes equations. \mathcal{B} represents the coefficients multiplied in front of temporal derivative term on the left hand side. In the incompressible case, \mathcal{B} is an identity matrix. We define the *base flow* as the equilibrium solution of the nonlinear equation, so the steady flow state \mathbf{q}_0 satisfies

$$\mathcal{NS}(\mathbf{q}_0) = 0. \quad (\text{A.2})$$

We then consider unsteady perturbations $\mathbf{q}'(\mathbf{x}, t)$. The state vector is then decomposed as

$$\mathbf{q}(\mathbf{x}, t) = \mathbf{q}_0(\mathbf{x}) + \epsilon \mathbf{q}'(\mathbf{x}, t), \quad (\text{A.3})$$

where ϵ is introduced to represent the infinitesimal amplitude of perturbations with respect to the steady flow state. Combining equations (A.1)-(A.3), we obtain

$$\epsilon \mathcal{B} \frac{\partial \mathbf{q}'}{\partial t} = \mathcal{NS}(\mathbf{q} + \epsilon \mathbf{q}'). \quad (\text{A.4})$$

The Navier-Stokes operator is then linearized around the base flow in the form

$$\epsilon \mathcal{B} \frac{\partial \mathbf{q}'}{\partial t} = \mathcal{NS}(\mathbf{q}_0) + \epsilon \mathcal{L}(\mathbf{q}_0) \mathbf{q}' + \mathcal{O}(\epsilon^2), \quad (\text{A.5})$$

that leads to

$$\mathcal{B} \frac{\partial \mathbf{q}'}{\partial t} = \mathcal{L}(\mathbf{q}_0) \mathbf{q}'. \quad (\text{A.6})$$

By solving the generalized eigenvalue problem

$$\lambda \mathcal{B} \mathbf{q}' = \mathcal{L}(\mathbf{q}_0) \mathbf{q}', \quad (\text{A.7})$$

the flow perturbations \mathbf{q}' can be expanded on the eigenmode basis

$$\mathbf{q}'_j(\mathbf{x}, t) = \phi_j(\mathbf{x}, t) \exp(\lambda_j t), \quad (\text{A.8})$$

where $\phi_j(\mathbf{x}, t)$ is the eigenvector and $\lambda_j = \sigma_j - i f_j$ is the eigenvalue of mode j . The real part of the eigenvalue corresponds to the temporal growth rate, denoted as $\sigma_j = \Re(\lambda_j)$, while the imaginary part of the eigenvalue corresponds to the frequency, denoted as $f_j = -\Im(\lambda_j)$.

The global linear stability analysis aims at answering the question if infinitesimal perturbations around a steady state grow or decay temporally. The flow is addressed as *globally stable* if the temporal growth rate of all the eigenmodes σ_j are negative. In this case, all the infinitesimal perturbations exponentially decay in the long time. In contrast, the flow is addressed as *globally unstable* if there exists at least one positive temporal growth rate. The frequency selection of unsteady perturbations is determined by the associated imaginary part f_j . The complex eigenvectors $\phi_j(\mathbf{x}, t)$ characterize the spatial structure of fluctuation

amplitudes and phases. The global modes are calculated in §3 for the bluff-body stabilized flame and in §4 for the V-shaped flame.

The adjoint eigenmodes are then introduced. We first define the spatial inner product $\langle \cdot \rangle$ with respect the mesh quadrature \mathcal{M} as

$$\langle \mathbf{a}(\mathbf{x}), \mathbf{b}(\mathbf{x}) \rangle = \int_{\Omega} \mathbf{a}^* \mathbf{b} d\mathbf{x} = \mathbf{a}^* \mathcal{M} \mathbf{b}, \quad (\text{A.9})$$

where the calculation domain is Ω . In the following, the spatial inner product is always defined with respect to the mesh quadrature \mathcal{M} , and the latter is not explicitly written. The adjoint linear operator \mathcal{L}^\dagger and the adjoint eigenvectors \mathbf{q}'^\dagger satisfy the relation

$$\langle \mathbf{q}'^\dagger, \mathcal{B} \frac{\partial \mathbf{q}'}{\partial t} - \mathcal{L} \mathbf{q}' \rangle = \langle -\mathcal{B}^\dagger \frac{\partial \mathbf{q}'^\dagger}{\partial t} - \mathcal{L}^\dagger \mathbf{q}'^\dagger, \mathbf{q}' \rangle, \quad (\text{A.10})$$

Thus, the adjoint eigenvalue problem is defined as

$$-\mathcal{B}^\dagger \frac{\partial \mathbf{q}'^\dagger}{\partial t} = \mathcal{L}^\dagger \mathbf{q}'^\dagger, \quad (\text{A.11})$$

which is equivalent to

$$\lambda^* \mathcal{B}^\dagger \mathbf{q}'^\dagger = \mathcal{L}^\dagger \mathbf{q}'^\dagger, \quad (\text{A.12})$$

where the adjoint eigenvalues λ^* are the complex conjugates of direct eigenvalues λ . The adjoint eigenfunction of mode j is written as

$$\mathbf{q}'^\dagger_j(\mathbf{x}, t) = \phi_j^\dagger(\mathbf{x}, t) \exp(\lambda_j^* t). \quad (\text{A.13})$$

The direct and adjoint eigenvectors are bi-orthogonal satisfying the relation

$$\langle \phi_j^\dagger, \mathcal{B} \phi_k \rangle = \delta_{jk}, \quad (\text{A.14})$$

where δ_{jk} is the Kronecker symbol. The bi-orthogonality is an important property used in the following sensitivity analysis.

A.1.2 Wavemaker analysis

Although the temporal stability and frequency selection can be calculated from the global modes, the global modes themselves do not further reveal the feedback mechanisms that generate the instability dynamics. The local feedback in global modes is characterized by local flow regions that drive the instability, and the identification of active flow regions is generally addressed as the *wavemaker* analysis (Chomaz et al. 1991). A summary of different methods to identify active flow regions is given in Paladini et al. 2019. They may be classified into two main categories: calculation of an eigenvalue variation $\delta\lambda_j$ and decomposition of eigenvalue λ_j itself.

The classical method belong to the first category is proposed by Giannetti and Luchini 2007, who identified active flow regions through the concept of structural sensitivity, that is the spatial overlap between the direct and adjoint modes. The variation of eigenvalue of mode j is expressed as

$$\delta\lambda_j = \langle \phi_j^\dagger, \phi_j \rangle. \quad (\text{A.15})$$

By applying the Cauchy-Schwarz theorem, the upper bound of the modulus of eigenvalue variation can be obtained as

$$|\delta\lambda_j| \leq \mathcal{M}_k w_k, \text{ where } w_k = \left\| \phi_j^\dagger \right\| \left\| \phi_j \right\|. \quad (\text{A.16})$$

Thus, the regions of local feedback bringing about the largest eigenvalue variations can be estimated by the structural sensitivity vector $\phi_j^\dagger \cdot \phi_j$.

The second category is based on a decomposition of eigenvalue λ_j onto the contribution of each cell in the calculation domain. By making use of the property of bi-orthogonality in (A.14), we multiply the adjoint eigenvector ϕ_j^\dagger on both sides of the direct eigenvalue problem (λ_j, ϕ_j) and we obtain

$$\lambda_j = \langle \phi_j^\dagger, \lambda_j \mathcal{B} \phi_j \rangle = \langle \phi_j^\dagger, \mathcal{L} \phi_j \rangle = \int_{\Omega} \mathbf{E}_j(\mathbf{x}) d\mathbf{x}, \quad (\text{A.17})$$

where

$$\mathbf{E}_j(\mathbf{x}) = \phi_j^{\dagger*} \cdot (\mathcal{L} \phi_j). \quad (\text{A.18})$$

This vector $\mathbf{E}_j(\mathbf{x})$ is denoted as the *endogeneity* of eigenmode (λ_j, ϕ_j) (Marquet and Lesshafft 2015). The integration of the contribution of each cell to the eigenvalue is exactly the value of λ_j . The spatial structure of the endogeneity field can reveal how much a local region contributes to the endogenous flow dynamics, and determine the most active flow region that drives the global instability. The spatial integration of $\mathbf{E}_j(\mathbf{x})$ is exactly the eigenvalue λ_j . If we define the frequency associated part in $\mathbf{E}_j(\mathbf{x})$ as $\mathbf{E}_{j,f}(\mathbf{x}) = -\Im[\mathbf{E}_j(\mathbf{x})]$ and the temporal growth associated part as $\mathbf{E}_{j,\sigma}(\mathbf{x}) = \Re[\mathbf{E}_j(\mathbf{x})]$, it is immediately clear that

$$\int_{\Omega} \mathbf{E}_{j,f}(\mathbf{x}) d\mathbf{x} = f \text{ and } \int_{\Omega} \mathbf{E}_{j,\sigma}(\mathbf{x}) d\mathbf{x} = \sigma. \quad (\text{A.19})$$

This endogeneity analysis method was first proposed by Marquet and Lesshafft 2015 with an application in the incompressible cylinder wake. It was further applied in the buoyant jet and plume (Chakravarthy et al. 2018), and the transonic buffet (Paladini et al. 2019). In this thesis, we apply this analysis in §3.4 for the bluff-body stabilized flame.

A.1.3 Sensitivity to base flow modifications

In Giannetti and Luchini 2007, the wavemaker is interpreted as a localized internal feedback of perturbations that leads the change of eigenvalue. Another interpretation of wavemaker is the modification of base flow, because small perturbations of non-normal operators may considerably alter the temporal stability and frequency selection (Chomaz 2005). The following question is how to identify the base flow modifications that destabilize the most the flow. Such analysis was first developed in a local analysis setting with application on the plane Couette flow (Bottaro et al. 2003), and later in a global setting applied on the cylinder wake flow (Marquet et al. 2008).

We consider small base flow modifications δq_0 that lead to the variation of base flow linear operator $\delta \mathcal{A}$, the variation of eigenvalue $\delta \lambda_j$ and the variation of eigenvector $\delta \phi_j$. The eigenvalue problem in (A.7) is reformulated as

$$(\lambda_j + \delta \lambda_j) \mathcal{B}(\phi_j + \delta \phi_j) = (\mathcal{L} + \delta \mathcal{L})(\phi_j + \delta \phi_j), \quad (\text{A.20})$$

that results in

$$\delta \lambda_j = \langle \phi_j^\dagger, \delta \mathcal{L} \phi_j \rangle = s_j^* \mathcal{M} \delta q_0. \quad (\text{A.21})$$

The base flow sensitivity vector s_j corresponding to the eigenmode j can then be extracted as $s_j = \mathcal{M}^{-1} \frac{\partial \lambda_j^*}{\partial q_0}$. If one aims at maximal $\delta \lambda_j$ under the constraint of variation modulus $\langle q_0, q_0 \rangle = 1$, it is immediately found that the base flow variation should satisfy the relation

$$q_0 = \alpha s_j, \text{ where } \alpha \in \mathbb{R}. \quad (\text{A.22})$$

The base flow sensitivity vector represents the spatial changes in the base flow that maximally destabilise the corresponding eigenmode. In this thesis, this analysis is applied in a parallel setting for the streaks in jets (§5.2.3.1).

A.2 Nonmodal analysis

The modal analysis determines the long-time intrinsic behaviour, especially useful for the prediction of frequency and transition of unstable oscillators. Instead, due to the non-normality of the operator \mathcal{L} (Chomaz 2005), the short-time behaviour of perturbations may grow considerably fast and lead to transitions, even in a globally stable flow. Such a flow is driven by external perturbations and considered as an amplifier. The short-time behaviour is investigated through the nonmodal analysis (Schmid and Henningson 2001), formulated either in temporal or frequency domain. The temporal approach identifies the initial perturbations leading to the optimal *transient growth* over a temporal horizon. In the frequency approach, an input-output mechanism is formulated to study the response of a flow system to an exterior harmonic forcing. The optimal forcing structures are identified by a standard method addressed as the *resolvent analysis*.

A.2.1 Temporal approach: transient growth

The temporal approach identifies the optimal initial perturbations that experience the fastest growth during a finite time window T . Mathematically, the initial perturbation $\mathbf{q}'_0(\mathbf{x}, t = 0)$ is sought such that the quotient

$$\sigma^2 = \frac{\|\mathbf{q}'(T)\|^2}{\|\mathbf{q}'_0\|^2} \quad (\text{A.23})$$

is maximized. Here the norm $\|\cdot\|$ represents an energy norm defined as $\|\mathbf{q}'\|^2 = \int_{\Omega} \mathbf{q}'^* \cdot \mathbf{q}' d\mathbf{x}$. In the incompressible setting, the energy norm may be taken as the energy of velocity perturbations $\int_{\Omega} |\mathbf{u}|^2 d\mathbf{x}$, where $|\mathbf{u}|^2 = |u_x|^2 + |u_y|^2$ for the Cartesian coordinates (x, y) . Such an optimisation problem can be solved by a time looping with the direct and adjoint equations, or a singular value decomposition (Schmid and Henningson 2001). The latter allows to identify not only the optimal perturbation that grows the fastest but also an orthogonal set of suboptimal perturbations ordered by the gain σ^2 representing their transient growth. A description of solution with the singular value decomposition is given in the following.

We aim at obtaining a matrix $\mathcal{P}(t)$ that represents the linear propagator to calculate the perturbation at a time moment t such that

$$\mathbf{q}'(t) = \mathcal{P}(t)\mathbf{q}'_0. \quad (\text{A.24})$$

The linear operator \mathcal{L} defined in (A.7) can be diagonalized in the form

$$\mathcal{L} = \mathcal{S}\Lambda\mathcal{S}^{-1}. \quad (\text{A.25})$$

The diagonal matrix Λ contains all the eigenvalues λ_j on its diagonal. Each column of the left-hand-side matrix \mathcal{S} is an eigenvector ϕ_j . The perturbations \mathbf{q}'_0 can be expanded as

$$\mathbf{q}'_0 = \mathcal{S}\boldsymbol{\alpha}, \quad (\text{A.26})$$

where the vector $\boldsymbol{\alpha}$ contains the coefficients of \mathbf{q}' in the eigenvalue basis. It is clear that those coefficients can be obtained by

$$\boldsymbol{\alpha} = \mathcal{S}^{-1}\mathbf{q}'_0, \quad (\text{A.27})$$

so the operator \mathcal{S}^{-1} is also addressed as the projection operator. The time evolution of perturbation \mathbf{q}' can then be obtained as

$$\mathbf{q}'(t) = \mathcal{S} \exp(\Lambda t) \boldsymbol{\alpha} = \mathcal{S} \exp(\Lambda t) \mathcal{S}^{-1} \mathbf{q}'_0, \quad (\text{A.28})$$

so the projector is obtained as

$$\mathcal{P}(t) = \mathcal{S} \exp(\Lambda t) \mathcal{S}^{-1}. \quad (\text{A.29})$$

If we formulate the energy norm in the matrix form $\|\mathbf{q}'\|^2 = \mathbf{q}'^H \mathcal{M} \mathbf{q}'$ with the mesh quadrature \mathcal{M} , where \cdot^H represents the Hermitian operator, the optimisation problem in (A.23) becomes

$$\sigma^2 = \frac{\mathbf{q}'_0{}^H \mathcal{P}(T)^H \mathcal{M} \mathcal{P}(T) \mathbf{q}'_0}{\mathbf{q}'_0{}^H \mathcal{M} \mathbf{q}'_0}, \quad (\text{A.30})$$

which is a problem of the Rayleigh quotient. By making use of the equations (A.26)(A.29), we can formulate a generalized eigenvalue problem

$$\exp(\Lambda^* T) \mathcal{S}^H \mathcal{M} \mathcal{S} \exp(\Lambda T) \alpha = \sigma^2 \mathcal{S}^H \mathcal{M} \mathcal{S} \alpha. \quad (\text{A.31})$$

The solution of this eigenvalue problem gives optimal linear combination α_{opt} of the eigenmodes ϕ_j , with respect to the energy growth σ^2 over a temporal horizon T . The optimal initial perturbation is then given by

$$\mathbf{q}'_{0,\text{opt}} = \mathcal{S} \alpha_{\text{opt}}. \quad (\text{A.32})$$

We identify the optimal perturbations in a round jet as rolls and streaks in §5.2.2.1.

A.2.2 Frequency approach: resolvent analysis

We consider a flow driven by an external forcing \mathbf{f}' of very small amplitude that acts directly on the temporal derivative of flow variables in the form

$$\mathcal{B} \frac{\partial \mathbf{q}'}{\partial t} = \mathcal{L} \mathbf{q}' + \mathcal{P} \mathbf{f}'. \quad (\text{A.33})$$

The vector \mathbf{f}' only contains non-zero forcing components. For example, if the forcing is imposed on the momentum equations, the dimension of \mathbf{f}' equals to the degrees of freedom of all the velocity components (in the temporal derivative of left-hand-side of the momentum equations). Thus, a rectangular matrix \mathcal{P} is introduced to fit the dimension between the size of \mathbf{f}' and \mathbf{q}' : the number of columns is the size of vector \mathbf{f}' and the number of rows is the size of vector \mathbf{q}' . In the case of forcing on momentum equations, values of coordinates corresponding to the velocity is set to be 1, and values of other coordinates are set to be 0. The matrix \mathcal{P} allows to impose the forcing on the selected equations, for instance, the momentum equations, so it is often addressed as the selective matrix.

The optimal forcing can be formulated as a *boundary* forcing problem, or a *volume* forcing problem. In the first case, a standard problem is to identify the optimal forcing profile at the flow inlet. In the second case, the forcing is located inside the flow region, that can represent some small disturbances inside the flow region.

In the present thesis, we focus on the identification of optimal *volume* forcing. In this context, the matrix \mathcal{P} may be further adjusted for two utilities. First, the matrix \mathcal{P} allows to restrict the forcing region, for example, inside the upstream nozzle of a jet. In this case, among all the coordinates corresponding to the forcing, we are required to further select all the coordinates inside the forcing region prescribed, and we set their value to be 1. In other words, the coordinates of the region outside the forcing region are set to be 0. Second, if one expects a smooth variation of forcing inside the flow region, for instance, a zero forcing at the inlet and a smooth variation of forcing amplitude from the inlet to the exit of a nozzle, we can set real values from 0 to 1 with a continuous variation inside the nozzle.

We consider time-harmonic forcing $\mathbf{f}' = \hat{\mathbf{f}}e^{i\omega t}$ at frequency $\frac{\omega}{2\pi}$, and its associated time-harmonic response $\mathbf{q}' = \hat{\mathbf{q}}e^{i\omega t}$. That leads to a relation between $\hat{\mathbf{q}}$ and $\hat{\mathbf{f}}$ in the frequency domain

$$(i\omega\mathcal{B} - \mathcal{L})\hat{\mathbf{q}} = \mathcal{P}\hat{\mathbf{f}}. \quad (\text{A.34})$$

The resolvent operator $\mathcal{R}(\omega)$ is introduced following

$$\hat{\mathbf{q}} = \mathcal{R}(\omega)\mathcal{P}\hat{\mathbf{f}}, \quad \mathcal{R}(\omega) = (i\omega\mathcal{B} - \mathcal{L})^{-1}. \quad (\text{A.35})$$

To this end, the forcing and the response are formulated in an *input-output* way: it is the forcing $\hat{\mathbf{f}}$ that results in the response $\hat{\mathbf{q}}$ through the frequency-dependant resolvent operator $\mathcal{R}(\omega)$.

The question to be answered by the resolvent analysis is, what is the most efficient way to force the flow to obtain the maximal response. To quantitatively measure the efficiency of a forcing, We define an input-output gain σ^2 that relates the forcing with response in the form

$$\sigma^2 = \frac{\|\hat{\mathbf{q}}\|^2}{\|\hat{\mathbf{f}}\|^2}, \quad (\text{A.36})$$

where the forcing and response norms are given by

$$\|\hat{\mathbf{f}}\|^2 = \hat{\mathbf{f}}^H \mathcal{M}_f \hat{\mathbf{f}}, \quad \|\hat{\mathbf{q}}\|^2 = \hat{\mathbf{q}}^H \mathcal{M}_q \hat{\mathbf{q}}. \quad (\text{A.37})$$

The matrix of forcing norm \mathcal{M}_f is strictly definite positive whose dimension is the same as forcing vector $\hat{\mathbf{f}}$, for instance, the total dimension of forcing on the momentum equations $\hat{\mathbf{f}}_u$ and $\hat{\mathbf{f}}_v$. It cannot be singular, because all the components in $\hat{\mathbf{f}}$ are non-zero. The width of response norm \mathcal{M}_q is the same as response vector $\hat{\mathbf{q}}$ of all degrees of freedom. It is allowed to be semi-definite positive if it only takes several flow variables as the response norm. For example, only the velocity is included in the response if we measure the energy of velocity fluctuations as the response norm, while the velocity is not included in the response norm if we measure the mean square of heat release fluctuations as the response norm.

Inserting the definition of resolvent operator (A.35) into the input-output gain (A.36), we obtain

$$\sigma^2 = \frac{\hat{\mathbf{f}}^H \mathcal{P}^H \mathcal{R}^H \mathcal{M}_q \mathcal{R} \mathcal{P} \hat{\mathbf{f}}}{\hat{\mathbf{f}}^H \mathcal{M}_f \hat{\mathbf{f}}}, \quad (\text{A.38})$$

which can be transformed into the generalized eigenvalue problem

$$\mathcal{P}^H \mathcal{R}^H \mathcal{M}_q \mathcal{R} \mathcal{P} \hat{\mathbf{f}} = \sigma^2 \mathcal{M}_f \hat{\mathbf{f}}. \quad (\text{A.39})$$

By solving this eigenvalue problem, we obtain an orthogonal basis of forcing labeled by their efficiency σ^2 , such that

$$\langle \hat{\mathbf{f}}_j^\dagger, \mathcal{M}_f \hat{\mathbf{f}}_k \rangle = \delta_{jk}. \quad (\text{A.40})$$

We can also demonstrate that the orthogonality of response basis by multiplying $\hat{\mathbf{f}}^H$ on the left-hand side. For the optimal forcing $\hat{\mathbf{f}}_{\text{opt}}$ with the largest energy gain, we can obtain the associated optimal response $\hat{\mathbf{q}}_{\text{opt}}$ through the resolvent operator in the form

$$\hat{\mathbf{q}}_{\text{opt}} = \mathcal{R}(\omega)\mathcal{P}\hat{\mathbf{f}}_{\text{opt}}. \quad (\text{A.41})$$

Here the optimisation problem is formulated as a generalized *eigenvalue* problem, either in the case of a temporal approach (A.31) or a frequency approach (A.39). Instead, the *singular* value decomposition is often addressed as the standard method to solve the

problem in nonmodal analysis. We make a brief remark on this point by considering the frequency approach (A.38) as an example. If we take the Cholesky decomposition of forcing and response norm matrix in the form

$$\mathcal{M}_f = \mathcal{N}_f^H \mathcal{N}_f \text{ and } \mathcal{M}_q = \mathcal{N}_q^H \mathcal{N}_q, \quad (\text{A.42})$$

we can formulate a singular value problem

$$\mathcal{N}_q \mathcal{R} \mathcal{P} \mathcal{N}_f^{-1} \hat{\mathbf{f}} = \sigma \hat{\mathbf{f}}, \quad (\text{A.43})$$

which is equivalent to the generalized eigenvalue problem (A.39). The optimal forcing and the gain can be obtained by a singular value decomposition of the linear operator $\mathcal{N}_q \mathcal{R} \mathcal{P} \mathcal{N}_f^{-1}$.

The resolvent analysis is used in §2 to identify the optimal forcing structures in a slot flame.

APPENDIX B

Numerical methods

A description of the main functions in the code applied to the bluff-body stabilised flame is given.

Contents

B.1	Description of different codes developed	110
B.2	Implementation of variational formulations in FENiCS	110
B.3	Newton solver	111
B.4	Timestepper	113
B.5	Linear analysis and eigenvalue solvers	113

B.1 Description of different codes developed

Two codes for linear analysis of flame instability are developed and used in this thesis. Both codes are developed based on the FENiCS library (Logg and Wells 2010) using finite-element methods for spatial discretisation on two-dimensional unstructured meshes. The codes are developed in Python environment.

One is the code *Felics* developed by Thomas Ludwig Kaiser with reference to a previous finite-element code developed by Lutz Lesshafft. This code allows to import the mean flow obtained by the external calculation tools, and then interpolate it on a new mesh whose number of grid points is low enough for a linear analysis based on the Jacobian matrix (Kaiser and Oberleithner 2021; Casel et al. 2022). We took part in the code development through properly implementing the reacting flow solver for flame analysis with one-step and two-step chemistry schemes. We created a separated branch of the Felics code for the study of slot flame and V-shaped flame, in which we implement the suitable governing equations and linearize the equations by symbolic calculations.

Another code is developed for the study of bluff-body stabilised flame. The key difference from the previous code is that this code calculates the base and mean flow inside the code, and then linear analysis is directly performed on the same mesh. The import and interpolation of external mean flow is not possible. Till the end of this thesis, only the reacting flow solver using low-Mach-number assumption and one-step chemical scheme has been implemented. A base flow solver based on the Newton iteration, and a nonlinear timestepper to get the eventual mean flow have been implemented.

B.2 Implementation of variational formulations in FENiCS

The FENiCS library provides a direct and compact way to implement the partial differential equations to be solved through the finite-elements methods. In the finite-elements methods, we look for an approximate solution of the true solution by using a linear combination of basis functions in a prescribed function space. It is the linear combination of coefficients that we seek to get the approximate solution. The approximate solution is in the prescribed function space, often addressed as the function space of *trial function*.

The routine procedure in a finite-method problem is the following: we substitute the approximate solution in the partial differential equations, multiply this approximation by a function in the space of *test function*, and then integrate over the entire computational domain. The integration by parts is then performed on the second derivative in the diffusion terms and the gradient of pressure in the flow equations, yielding boundary flux. The function space of test function can be chosen the same as the trial function. In our code, we use the continuous Galerkin method, with respect to the discontinuous Galerkin method where the function space is piecewise continuous. In the following, we describe the code used in the calculation of the bluff-body stabilised flame.

BuildFunctionSpace: Build the mixed function space including all the flow variables on a given mesh. In the low-Mach-number reacting case with one-step chemistry, the mixed function space contains velocity (VectorElement), pressure (FiniteElement), density (FiniteElement) and mass fraction of species (FiniteElement). All the elements are Lagrangian triangular elements. The elements for the velocity are of second order. The elements for the other three scalars are of first order.

InitialConditions: Set the initial conditions of a function for calculating a base flow.

GenerateTestFunctions: Generate test functions to be multiplied on both sides of the weak form from the built function space.

OperatorNonlinear: Construct the right hand side of nonlinear governing equations according to (3.1-3.3) and (3.6). The nonlinear form is constructed based on a function evaluated on the base or mean state of which the values are either initialized through **InitialConditions** or loaded from previous calculations. The test functions are multiplied to the weak form.

B.3 Newton solver

In our code, we use Newton method to calculate the steady solutions of the governing equations. Other methods often used to calculate the steady base state include the selective frequency damping method (Åkervik et al. 2006), which adds a dissipative forcing term to each flow on the right hand side. To this end, extra equations corresponding to each independent flow variables are required to be involved. Considering that the number of variables in the reacting flow equations are already large, we decide to use the Newton method.

The Newton iteration has a finite radius of convergence, so it is not possible to obtain a base flow from an arbitrarily initialized flow field in one calculation, for any configuration of which the convergence is not obvious, such as a flame or a jet at high Reynolds number. The common practice that we use is to calculate from a flow with setting a very large viscosity (or Stokes flow) and without chemical reaction, as illustrated in figure B.1. We multiply a play factor before all the diffusion terms denoted as β_{visco} . Here β_{visco} is not only set in the momentum equation, but also in the energy equation and species equation in front of the diffusion terms therein. Another play factor is multiplied before the chemical heat release term denoted as β_{hr} .

For the calculation of the bluff-body stabilised flow, we begin with setting β_{visco} around 30, and β_{hr} equal to 0.16 in the first iteration. The steady base state obtained with this set of parameter is shown in B.1(a). We observe very minor consumptions of fuel, but it is a good sign consistent with the strong diffusion effects and tiny heat release. Then, we calculate intermediate flow fields by gradually decreasing the value of β_{visco} , and increasing the value of β_{hr} , respectively. The steady solution corresponding to these intermediate parameters are shown in B.1(b-e). We can already observe a flame layer with the parameters in B.1(b), and furthermore the flame thickness is gradually reduced, especially with the increase of Reynolds number following the decrease of β_{visco} . Note that it may be required to adjust the relaxation parameter that controls the step length in Newton solver to get a good convergence in each intermediate flow field.

Calculation of the steady base state of the flame has also been conducted via Newton solver by Albayrak et al. 2018; Douglas 2021. In our case, the convergence of steady base flow can reach the machine precision, given a well-designed mesh to resolve the flame.

At the beginning of this thesis, we also implemented a Newton solver to calculate the base flow for the slot flame. In the lower half of figure B.2, we show the base flow calculated with Newton solver in FENiCS, but for simplicity, this calculation is conducted with a one-step chemical scheme. The upper half of figures are the base flow calculated with AVBP with the two-step BFER chemistry. The difference of flame tip position simply comes from the different chemical schemes used.

We chose AVBP to calculate the base flow, because it is considered as a standard code of high-fidelity to simulate the flame dynamics. It also has more advanced numerical schemes

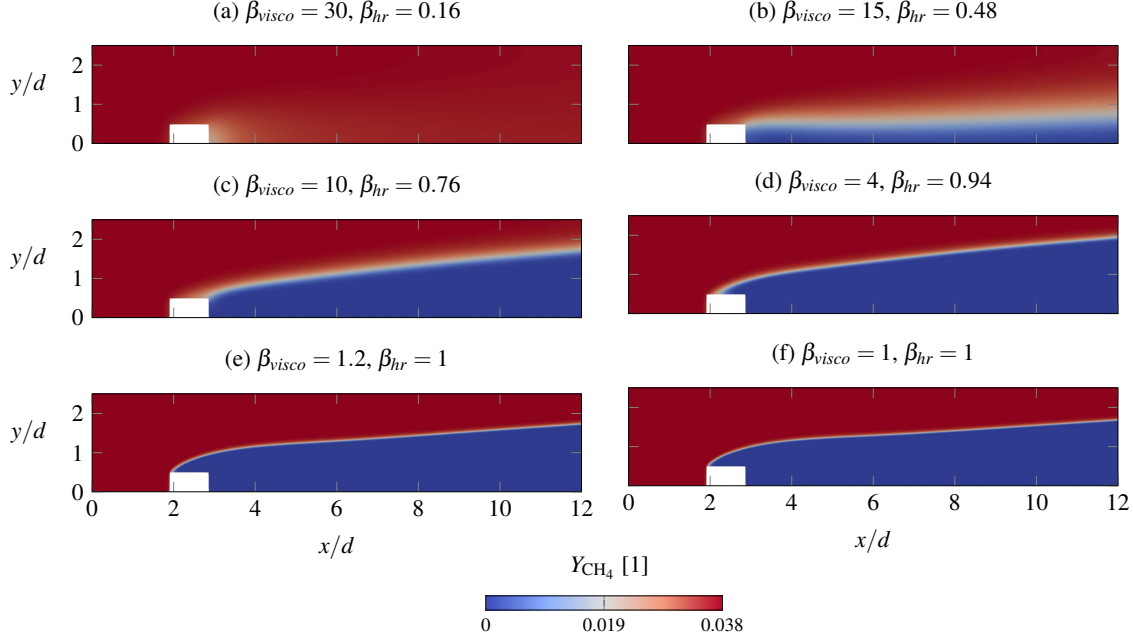


Figure B.1: Illustration of Newton iteration by gradually decreasing diffusion factor β_{visco} and increasing heat release factor β_{hr} until they reach 1. Intermediate steady base states for convergence to the final steady base state are shown.

adapted for flame simulations. When we tried to use our Newton solver to calculate a base flow with two-step chemistry, the convergence was far more difficult to achieve.

However, it should be noticed there is a very important advantage of having a steady base flow solver inside the linear code, with respect to importing a base flow calculated from an exterior solver such as AVBP. In the case that we have a Newton solver inside our code, we can calculate the base flow, and then on the same *mesh* and with the exact same *equations* linearized from the nonlinear one, we can conduct the linear analysis accordingly. In contrast, when we import a base flow from the exterior, it happens very often that we have to interpolate that base flow on another mesh, because the number of grids for nonlinear calculations could be very large. Such interpolation inevitably involves numerical errors into the base flow. Besides, the governing equations from an exterior solver could be very complicated (i.e. a compressible reacting flow in AVBP), and sometimes we do not know the exact nonlinear equations and the physical parameters (i.e. tabulated heat capacity) used in the exterior solver. Thus the base flow imported could be not conforming as a steady solution of our equations at all. This can lead to very wrong results in the linear calculation, especially for a very steep problem here with large gradients across the flame fronts (i.e. the gain of FTF can reach up to 10 using some other interpolation methods). Such observation was also confirmed in the thesis of Kampen 2006.

We find the Newton solver is very good at thinning the flame front, which was also confirmed in Douglas 2021, but the Newton solver is very bad at moving the flame front. For example, when we intended to smooth the interpolated base flow imported from the AVBP, we found that the convergence was not able to be reached even though we use the governing equations very close to that used in the AVBP.

The following two functions in our code concern the Newton solver.

BoundaryConditionsNonlinear: Construct the boundary conditions of Newton solver and nonlinear timestepping.

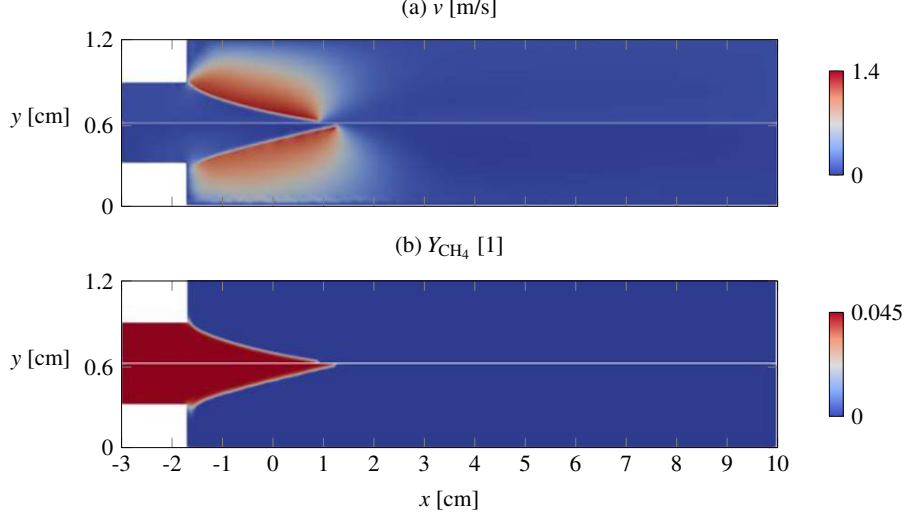


Figure B.2: Base flow of the slot flame computed by the AVBP (upper half) and the Newton solver (lower half).

Newton: Use Newton iteration method to calculate a steady base state.

B.4 Timestepper

A timestepper is developed to conduct nonlinear timestepping on unstable oscillating flames. The Crank-Nicolson method is used for the time discretisation. We separate the linear terms and nonlinear terms on the right-hand side of the flow equations (A.1), in the form

$$\mathcal{B} \frac{\partial \mathbf{q}}{\partial t} = \mathcal{N} \mathcal{S}_{nonlinear}(\mathbf{q}) + \mathcal{N} \mathcal{S}_{linear}(\mathbf{q}), \quad (\text{B.1})$$

where $\mathcal{N} \mathcal{S}_{linear}$ includes the linear terms, that is, the diffusion and pressure gradient, and $\mathcal{N} \mathcal{S}_{nonlinear}$ contains all the nonlinear terms such as the convection and chemical reactions. If we denote the flow variables at the present time step as \mathbf{q}^n and the flow variables at the next time step to be calculated at \mathbf{q}^{n+1} , the Crank-Nicolson method writes

$$\mathcal{B} \frac{\mathbf{q}^{n+1} - \mathbf{q}^n}{\Delta t} = \frac{1}{2} [\mathcal{N} \mathcal{S}_{nonlinear}(\mathbf{q}^{n+1}) + \mathcal{N} \mathcal{S}_{nonlinear}(\mathbf{q}^n)] + \mathcal{N} \mathcal{S}_{linear}(\mathbf{q}^n). \quad (\text{B.2})$$

The desired flow variable \mathbf{q}^{n+1} is obtained by solving this equation using the nonlinear solver with Newton method. The length of time step Δt should be well chosen to ensure the convergence.

TimeStepping: Conduct nonlinear timestepping with an implicit method, the Crank-Nicolson method.

B.5 Linear analysis and eigenvalue solvers

In the linear analysis, we are required to obtain first the linear operators \mathcal{B} and \mathcal{L} in the equation $\mathcal{B} \frac{\partial \mathbf{q}'}{\partial t} = \mathcal{L}(\mathbf{q}_0) \mathbf{q}'$. The sparse matrices in the format CSR are constructed. The left-hand-side matrix \mathcal{B} is constructed with trial functions. For example, in the form $\bar{\rho} \mathbf{u}'$, $\bar{\rho}$ is imported from base flow and \mathbf{u}' is in the trial function space.

In contrast, the right-hand-side operator $\mathcal{L}(\mathbf{q}_0)$ is obtained by linearizing the nonlinear operator $\mathcal{NS}(\mathbf{q}_0)$ through the symbolic calculation function **derivative** in FENiCS. The function **derivative** allows to linearize the given nonlinear form and evaluate the linearized form on given values of variables, that is, the value of base or mean flow in our case. Thanks to this function, it is no longer necessary to explicitly write the linear form of \mathcal{B} , which can be a very complicated in the reacting flow equations, for example, the linearization of reaction schemes, temperature-dependant viscosity and heat capacity.

The homogeneous Dirichlet condition are imposed by removing all the lines and columns corresponding to the index of the boundaries.

The matrix \mathcal{B} in the generalized eigenvalue problem $\lambda \mathcal{B} \mathbf{q}' = \mathcal{L}(\mathbf{q}_0) \mathbf{q}'$ is not definitely positive. To this end, the eigenvalues are calculated via the implicitly restarted Arnoldi algorithm with a given shift-invert value (Lehoucq et al. 1998). It is possible to calculate the eigenvalues inside the Python environment using **eigs** in Scipy, or export the matrix to Matlab to calculate the eigenvalue with the Matlab function **eigs**. Although it seems that the eigenvalue solver in both environments are wrapper of the eigenvalue solver in ARPACK, sometimes the correct eigenvalues of the flame are not able to be obtained through Scipy. The reasons may lie in the definitely positive property of the left-hand matrix \mathcal{B} , but it has not been entirely understood. Thus, it is recommended to use the Matlab function **eigs**, at least as a double-check.

In the generalized eigenvalue problem of the resolvent analysis $\mathcal{P}^H \mathcal{R}^H \mathcal{M}_q \mathcal{R} \mathcal{P} \hat{\mathbf{f}} = \sigma^2 \mathcal{M}_f \hat{\mathbf{f}}$, the matrix $\mathcal{P}^H \mathcal{R}^H \mathcal{M}_q \mathcal{R} \mathcal{P}$ is definitely positive. The optimal gains can be calculated through the implicitly restarted Arnoldi algorithm without prescribing a shift-invert value. the function **eigs** in Scipy is capable of well computing the eigenvalues associated with the optimal forcing.

GenerateTrialFunctions: The trial functions approximating the unknown variables are generated. The trial functions are used to construct the left-hand-side matrix \mathcal{B} .

BoundaryConditionsLinear: Construct the boundary condition for linear analysis.

Modal: Calculate the global modes of the linear operator.

Endogeneity: Conduct the endogeneity analysis following the formulations in §A.1.2.

BaseFlowSensitivity: Conduct the base flow sensitivity following the formulations in §A.1.3. To obtain the base flow sensitivity vector, we use the function **derivative** to take the derivative of nonlinear form $\mathcal{L}(\mathbf{q}_0) \phi_0$ with respect to the base flow variables, where ϕ_0 is the least stable eigenmode following the notations in the previous chapter. We then multiply the adjoint vector on the left to get the base flow sensitivity vector.

Resolvent: Conduct the resolvent analysis following the formulations in §A.2.2.

Bibliography

- Åbom, M. and H. Bodén (1988). “Error analysis of two-microphone measurements in ducts with flow”. In: *J. Acoust. Soc. Am.* 83.6, pp. 2429–2438.
- Åkervik, E., L. Brandt, D. S. Henningson, J. Höpffner, O. Marxen, and P. Schlatter (2006). “Steady solutions of the Navier-Stokes equations by selective frequency damping”. In: *Phys. Fluids* 18.6, p. 068102.
- Albayrak, A., D. Bezgin, and W. Polifke (2018). “Response of a swirl flame to inertial waves”. In: *Int. J. Spray Combust. Dyn.* 10.4, pp. 277–286.
- Albayrak, A., M. Juniper, and W. Polifke (2019). “Propagation speed of inertial waves in cylindrical swirling flows”. In: *J. Fluid Mech.* 879, pp. 85–120.
- Alnæs, M., J. Blechta, J. Hake, A. Johansson, B. Kehlet, A. Logg, C. Richardson, J. Ring, M. Rognes, and G. Wells (2015). “The FEniCS project version 1.5”. In: *Archive of Numerical Software* 3.100.
- Alnæs, M., A. Logg, K. Ølgaard, M. Rognes, and G. Wells (2014). “Unified form language: A domain-specific language for weak formulations of partial differential equations”. In: *ACM Trans. Math. Softw.* 40.2, pp. 1–37.
- Avdonin, A., M. Meindl, and W. Polifke (2019). “Thermoacoustic analysis of a laminar premixed flame using a linearized reactive flow solver”. In: *Proc. Combust. Inst.* 37.4, pp. 5307–5314.
- Balasubramanian, M., A. Kushwaha, Y. Guan, J. Feng, P. Liu, V. Gupta, and L. K. B. Li (2021). “Global hydrodynamic instability and blowoff dynamics of a bluff-body stabilized lean-premixed flame”. In: *Phys. Fluids* 33.3, p. 034103.
- Barbagallo, A., G. Dergham, D. Sipp, P. Schmid, and J.-C. Robinet (2012). “Closed-loop control of unsteadiness over a rounded backward-facing step”. In: *J. Fluid Mech.* 703, pp. 326–362.
- Barbagallo, A., D. Sipp, and P. Schmid (2009). “Closed-loop control of an open cavity flow using reduced-order models”. In: *J. Fluid Mech.* 641, pp. 1–50.
- Barkley, D. (2006). “Linear analysis of the cylinder wake mean flow”. In: *EPL* 75.5, p. 750.
- Beneddine, S., D. Sipp, A. Arnault, J. Dandois, and L. Lesshafft (2016). “Conditions for validity of mean flow stability analysis”. In: *J. Fluid Mech.* 798, pp. 485–504.
- Bengana, Y. and L. Tuckerman (2021). “Frequency prediction from exact or self-consistent mean flows”. In: *Phys. Rev. Fluids* 6.6, p. 063901.
- Bill, R. and K. Tarabanis (1986). “The effect of premixed combustion on the recirculation zone of circular cylinders”. In: *Combust. Sci. Technol.* 47.1-2, pp. 39–53.
- Blanchard, M. (2015). “Linear and nonlinear dynamics of laminar premixed flames submitted to flow oscillations”. PhD thesis. Ecole Polytechnique.
- Blanchard, M., P. Schmid, D. Sipp, and T. Schuller (2016). “Pressure wave generation from perturbed premixed flames”. In: *J. Fluid Mech.* 797, pp. 231–246.

- Blanchard, M., T. Schuller, D. Sipp, and P. Schmid (2015). “Response analysis of a laminar premixed M-flame to flow perturbations using a linearized compressible Navier-Stokes solver”. In: *Phys. Fluids* 27.4, p. 043602.
- Bottaro, A., P. Corbett, and P. Luchini (2003). “The effect of base flow variation on flow stability”. In: *J. Fluid Mech.* 476, pp. 293–302.
- Boujo, E., A. Fani, and F. Gallaire (2015). “Second-order sensitivity of parallel shear flows and optimal spanwise-periodic flow modifications”. In: *J. Fluid Mech.* 782, pp. 491–514.
- (2019). “Second-order sensitivity in the cylinder wake: Optimal spanwise-periodic wall actuation and wall deformation”. In: *Phys. Rev. Fluids* 4 (5), p. 053901.
- Brandt, L., C. Cossu, J.-M. Chomaz, P. Huerre, and D. S. Henningson (2003). “On the convectively unstable nature of optimal streaks in boundary layers”. In: *J. Fluid Mech.* 485, pp. 221–242.
- Brandt, L. (2014). “The lift-up effect: the linear mechanism behind transition and turbulence in shear flows”. In: *Eur. J. Mech. B Fluids* 47, pp. 80–96.
- Butler, K. M. and B. F. Farrell (1992). “Three-dimensional optimal perturbations in viscous shear flow”. In: *Phys. Fluids A* 4.8, pp. 1637–1650.
- Candel, S., D. Durox, T. Schuller, J.-F. Bourgouin, and J. P. Moeck (2014). “Dynamics of swirling flames”. In: *Annu. Rev. Fluid Mech.* 46, pp. 147–173.
- Casel, M., K. Oberleithner, F. Zhang, T. Zirwes, H. Bockhorn, D. Trimis, and T. L. Kaiser (2022). “Resolvent-based Modelling of Coherent Structures in a Turbulent Jet Flame Using a Passive Flame Approach”. In: *Combust. Flame* 236, p. 111695.
- Cavalieri, A., P. Jordan, and L. Lesshafft (2019). “Wave-packet models for jet dynamics and sound radiation”. In: *Appl. Mech. Rev.* 71.2.
- CERFACS (2017). *CANTERA User’s Guide*. (<https://www.cerfacs.fr/cantera/mechanisms/meth.php>).
- Chakravarthy, R. V. K., L. Lesshafft, and P. Huerre (2018). “Global stability of buoyant jets and plumes”. In: *J. Fluid Mech.* 835, pp. 654–673.
- Chaudhuri, S., S. Kostka, M. Renfro, and B. Cetegen (2012). “Blowoff mechanism of harmonically forced bluff body stabilized turbulent premixed flames”. In: *Combust. Flame* 159.2, pp. 638–640.
- Chen, R., J. Driscoll, J. Kelly, M. Namazian, and R. Schefer (1990). “A comparison of bluff-body and swirl-stabilized flames”. In: *Combust. Sci. Technol.* 71.4-6, pp. 197–217.
- Cheng, Y., T. Jin, K. Luo, Z. Li, H. Wang, and J. Fan (2021). “Effect of flame holder temperature on the instability modes of laminar premixed flames”. In: *Fuel* 293, p. 119628.
- Cherubini, S., P. De Palma, J.-C. Robinet, and A. Bottaro (2011). “The minimal seed of turbulent transition in the boundary layer”. In: *J. Fluid Mech.* 689, pp. 221–253.
- Cho, J. and T. Lieuwen (2005). “Laminar premixed flame response to equivalence ratio oscillations”. In: *Combust. Flame* 140.1-2, pp. 116–129.
- Choi, H., W.-P. Jeon, and J. Kim (2008). “Control of flow over a bluff body”. In: *Annu. Rev. Fluid Mech.* 40, pp. 113–139.
- Chomaz, J.-M. (2005). “Global instabilities in spatially developing flows: non-normality and nonlinearity”. In: *Annu. Rev. Fluid Mech.* 37, pp. 357–392.
- Chomaz, J.-M., P. Huerre, and L. G. Redekopp (1991). “A frequency selection criterion in spatially developing flows”. In: *Stud. Appl. Math.* 84.2, pp. 119–144.
- Chu, B.-T. (1953). “On the generation of pressure waves at a plane flame front”. In: *Symposium (International) on Combustion* 4.1. Fourth Symposium (International) on Combustion, pp. 603–612.
- (1965). “On the energy transfer to small disturbances in fluid flow (Part I)”. In: *Acta Mech.* 1.3, pp. 215–234.

- Coenen, W., L. Lesshafft, X. Garnaudo, and A. Sevilla (2017). “Global instability of low-density jets”. In: *J. Fluid Mech.* 820, pp. 187–207.
- Colin, O., A. Benkenida, and C. Angelberger (2003). “3D modeling of mixing, ignition and combustion phenomena in highly stratified gasoline engines”. In: *Oil Gas Sci. Technol.* 58.1, pp. 47–62.
- Colin, O. and M. Rudgyard (2000). “Development of high-order Taylor–Galerkin schemes for LES”. In: *J. Comput. Phys.* 162.2, pp. 338–371.
- Courtine, E., L. Selle, and T. Poinso (2015). “DNS of intrinsic thermoacoustic modes in laminar premixed flames”. In: *Combust. Flame* 162.11, pp. 4331–4341.
- Crow, S. C. and F. Champagne (1971). “Orderly structure in jet turbulence”. In: *J. Fluid Mech.* 48.3, pp. 547–591.
- Dally, B., A. Masri, R. Barlow, and G. Fiechtner (1998). “Instantaneous and mean compositional structure of bluff-body stabilized nonpremixed flames”. In: *Combust. Flame* 114.1-2, pp. 119–148.
- Davis, R., E. Moore, and L. Purtell (1984). “A numerical-experimental study of confined flow around rectangular cylinders”. In: *Phys. Fluids* 27.1, pp. 46–59.
- Del Guercio, G., C. Cossu, and G. Pujals (2014). “Stabilizing effect of optimally amplified streaks in parallel wakes”. In: *J. Fluid Mech.* 739, pp. 37–56.
- Douglas, C. M. (2021). “Dynamics of swirling jets and flames”. PhD thesis. Georgia Institute of Technology.
- Douglas, C. M., B. Emerson, S. Hemchandra, and T. Lieuwen (2021). “Forced flow response analysis of a turbulent swirling annular jet flame”. In: *Phys. Fluids* 33.8, p. 085124.
- Dowling, A. P. and Y. Mahmoudi (2015). “Combustion noise”. In: *Proc. Combust. Inst.* 35.1, pp. 65–100.
- Dowling, A. P. and A. S. Morgans (2005). “Feedback control of combustion oscillations”. In: *Annu. Rev. Fluid Mech.* 37, pp. 151–182.
- Dupuy, F., M. Gatti, C. Mirat, L. Gicquel, F. Nicoud, and T. Schuller (2020). “Combining analytical models and LES data to determine the transfer function from swirled premixed flames”. In: *Combust. Flame* 217, pp. 222–236.
- Dyke, W. van (1989). *An album of fluid motion*. Parabolic Press.
- Emerson, B. and T. Lieuwen (2015). “Dynamics of harmonically excited, reacting bluff body wakes near the global hydrodynamic stability boundary”. In: *J. Fluid Mech.* 779, pp. 716–750.
- Emerson, B., T. Lieuwen, and M. Juniper (2016). “Local stability analysis and eigenvalue sensitivity of reacting bluff-body wakes”. In: *J. Fluid Mech.* 788, pp. 549–575.
- Emerson, B., J. O’Connor, M. Juniper, and T. Lieuwen (2012). “Density ratio effects on reacting bluff-body flow field characteristics”. In: *J. Fluid Mech.* 706, pp. 219–250.
- Emmert, T., S. Bomberg, and W. Polifke (2015). “Intrinsic thermoacoustic instability of premixed flames”. In: *Combust. Flame* 162.1, pp. 75–85.
- Erickson, R. and M. Soteriou (2011). “The influence of reactant temperature on the dynamics of bluff body stabilized premixed flames”. In: *Combust. Flame* 158.12, pp. 2441–2457.
- Finney, M. A., J. D. Cohen, J. M. Forthofer, S. S. McAllister, M. J. Gollner, D. J. Gorham, K. Saito, N. K. Akafuah, B. A. Adam, and J. D. English (2015). “Role of buoyant flame dynamics in wildfire spread”. In: *Proc. Natl. Acad. Sci.* 112.32, pp. 9833–9838.
- Flinois, T. L. and A. S. Morgans (2016). “Feedback control of unstable flows: a direct modelling approach using the eigensystem realisation algorithm”. In: *J. Fluid Mech.* 793, pp. 41–78.

- Föller, S. and W. Polifke (2012). “Identification of aero-acoustic scattering matrices from large eddy simulation. Application to a sudden area expansion of a duct”. In: *J. Sound Vib* 331.13, pp. 3096–3113.
- Franzelli, B., E. Riber, L. Y. Gicquel, and T. Poinso (2012). “Large Eddy Simulation of combustion instabilities in a lean partially premixed swirled flame”. In: *Combust. Flame* 159.2, pp. 621–637.
- Garnaud, X., L. Lesshafft, P. Schmid, and P. Huerre (2013a). “Modal and transient dynamics of jet flows”. In: *Phys. Fluids* 25.4, p. 044103.
- (2013b). “The preferred mode of incompressible jets: linear frequency response analysis”. In: *J. Fluid Mech.* 716, pp. 189–202.
- Geikie, M. K., C. J. Rising, A. J. Morales, and K. A. Ahmed (2021). “Turbulent flame-vortex dynamics of bluff-body premixed flames”. In: *Combust. Flame* 223, pp. 28–41.
- Ghani, A., T. Poinso, L. Gicquel, and G. Staffelbach (2015). “LES of longitudinal and transverse self-excited combustion instabilities in a bluff-body stabilized turbulent premixed flame”. In: *Combust. Flame* 162.11, pp. 4075–4083.
- Giannetti, F. and P. Luchini (2007). “Structural sensitivity of the first instability of the cylinder wake”. In: *J. Fluid Mech.* 581, pp. 167–197.
- Gicquel, L. Y., G. Staffelbach, and T. Poinso (2012). “Large eddy simulations of gaseous flames in gas turbine combustion chambers”. In: *Prog. Energy Combust. Sci.* 38.6, pp. 782–817.
- Gourdain, N., F. Sicot, F. Duchaine, and L. Gicquel (2014). “Large eddy simulation of flows in industrial compressors: a path from 2015 to 2035”. In: *Proc. Roy. Soc. A* 372.2022, p. 20130323.
- Guiberti, T. F., D. Durox, P. Scouffaire, and T. Schuller (2015). “Impact of heat loss and hydrogen enrichment on the shape of confined swirling flames”. In: *Proc. Combust. Inst.* 35.2, pp. 1385–1392.
- Hakes, R., W. Coenen, A. Sánchez, M. Gollner, and F. Williams (2021). “Stability of laminar flames on upper and lower inclined fuel surfaces”. In: *Proc. Combust. Inst.* 38.3, pp. 4515–4523.
- Han, X., J. Li, and A. S. Morgans (2015). “Prediction of combustion instability limit cycle oscillations by combining flame describing function simulations with a thermoacoustic network model”. In: *Combust. Flame* 162.10, pp. 3632–3647.
- Hermeth, S., G. Staffelbach, L. Y. Gicquel, V. Anisimov, C. Cirigliano, and T. Poinso (2014). “Bistable swirled flames and influence on flame transfer functions”. In: *Combust. Flame* 161.1, pp. 184–196.
- Hill, D. (1992). “A theoretical approach for analyzing the restabilization of wakes”. In: *30th Aerospace Sciences Meeting and Exhibit*, p. 67.
- (1995). “Adjoint systems and their role in the receptivity problem for boundary layers”. In: *J. Fluid Mech.* 292, pp. 183–204.
- Hoeijmakers, M., V. Kornilov, I. Arteaga, P. de Goey, and H. Nijmeijer (2014). “Intrinsic instability of flame-acoustic coupling”. In: *Combust. Flame* 161.11, pp. 2860–2867.
- (2016). “Flame dominated thermoacoustic instabilities in a system with high acoustic losses”. In: *Combust. Flame* 169, pp. 209–215.
- Huerre, P. and P. Monkewitz (1990). “Local and global instabilities in spatially developing flows”. In: *Annu. Rev. Fluid Mech.* 22.1, pp. 473–537.
- Hwang, Y. (2011). “Large-scale streaks in wall-bounded turbulent flows: amplification, instability, self-sustaining process and control”. PhD thesis. Ecole Polytechnique.
- Hwang, Y. and H. Choi (2006). “Control of absolute instability by basic-flow modification in a parallel wake at low Reynolds number”. In: *J. Fluid Mech.* 560, pp. 465–475.

- Hwang, Y. and C. Cossu (2010a). “Self-sustained process at large scales in turbulent channel flow”. In: *Phys. Rev. Lett.* 105.4, p. 044505.
- Hwang, Y. and C. Cossu (2010b). “Amplification of coherent streaks in the turbulent Couette flow: an input–output analysis at low Reynolds number”. In: *Journal of Fluid Mechanics* 643, pp. 333–348.
- Jiménez, J. (2013). “How linear is wall-bounded turbulence?” In: *Phys. Fluids* 25.11, p. 110814.
- Jiménez-González, J. I. and P. Brancher (2017). “Transient energy growth of optimal streaks in parallel round jets”. In: *Phys. Fluids* 29.11, p. 114101.
- Jin, B., S. J. Illingworth, and R. D. Sandberg (2020). “Feedback control of vortex shedding using a resolvent-based modelling approach”. In: *J. Fluid Mech.* 897.
- Jordan, P. and T. Colonius (2013). “Wave packets and turbulent jet noise”. In: *Annu. Rev. Fluid Mech.* 45, pp. 173–195.
- Juniper, M. and B. Pier (2015). “The structural sensitivity of open shear flows calculated with a local stability analysis”. In: *Eur. J. Mech. B Fluids* 49, pp. 426–437.
- Juniper, M. and R. Sujith (2018). “Sensitivity and nonlinearity of thermoacoustic oscillations”. In: *Annu. Rev. Fluid Mech.* 50, pp. 661–689.
- Kaess, R., W. Polifke, T. Poinso, N. Noiray, D. Durox, T. Schuller, and S. Candel (2008). “Cfd-based mapping of the thermo-acoustic stability of a laminar premix burner”. In: *Proceedings of the summer program*. CTR, p. 289.
- Kaiser, T., L. Lesshafft, and K. Oberleithner (2019a). “Prediction of the Flow Response of a Turbulent Flame to Acoustic Perturbations Based on Mean Flow Resolvent Analysis”. In: *J. Eng. Gas Turb. Power* 141.11.
- Kaiser, T. and K. Oberleithner (2021). “A global linearized framework for modelling shear dispersion and turbulent diffusion of passive scalar fluctuations”. In: *J. Fluid Mech.* 915.
- Kaiser, T., G. Öztarlik, L. Selle, and T. Poinso (2019b). “Impact of symmetry breaking on the Flame Transfer Function of a laminar premixed flame”. In: *Proc. Combust. Inst.* 37.2, pp. 1953–1960.
- Kampen, J. van, J. B. Kok, and T. H. van der Meer (2007). “Efficient retrieval of the thermo-acoustic flame transfer function from a linearized CFD simulation of a turbulent flame”. In: *Int. J. Numer. Methods Fluids* 54.9, pp. 1131–1149.
- Kampen, J. van (2006). “Acoustic pressure oscillations induced by confined turbulent premixed natural gas flames”. PhD thesis. Universiteit Twente.
- Kantharaju, J., R. Courtier, B. Leclaire, and L. Jacquin (2020). “Interactions of large-scale structures in the near field of round jets at high Reynolds numbers”. In: *J. Fluid Mech.* 888.
- Karban, U., B. Bugeat, E. Martini, A. Towne, A. Cavalieri, L. Lesshafft, A. Agarwal, P. Jordan, and T. Colonius (2020). “Ambiguity in mean-flow-based linear analysis”. In: *J. Fluid Mech.* 900.
- Kedia, K. and A. Ghoniem (2014). “The anchoring mechanism of a bluff-body stabilized laminar premixed flame”. In: *Combust. Flame* 161.9, pp. 2327–2339.
- (2015). “The blow-off mechanism of a bluff-body stabilized laminar premixed flame”. In: *Combust. Flame* 162.4, pp. 1304–1315.
- Kerswell, R. (2018). “Nonlinear nonmodal stability theory”. In: *Annu. Rev. Fluid Mech.* 50, pp. 319–345.
- Kiel, B., K. Garwick, J. Gord, J. Miller, A. Lynch, R. Hill, and S. Phillips (2007). “A detailed investigation of bluff body stabilized flames”. In: *45th AIAA Aerospace Sciences Meeting and Exhibit*, p. 168.

- Kim, Y., B. Lee, and H. Im (2019). “Hydrodynamic and chemical scaling for blow-off dynamics of lean premixed flames stabilized on a meso-scale bluff-body”. In: *Proc. Combust. Inst.* 37.2, pp. 1831–1841.
- Kobayashi, H., A. Hayakawa, K. K. A. Somarathne, and E. C. Okafor (2019). “Science and technology of ammonia combustion”. In: *Proc. Combust. Inst.* 37.1, pp. 109–133.
- Lajús, F. C., A. Sinha, A. Cavalieri, C. J. Deschamps, and T. Colonius (2019). “Spatial stability analysis of subsonic corrugated jets”. In: *J. Fluid Mech.* 876, pp. 766–791.
- Landahl, M. T. (1975). “Wave breakdown and turbulence”. In: *SIAM J. Appl. Math.* 28.4, pp. 735–756.
- Lehoucq, R. B., D. C. Sorensen, and C. Yang (1998). “ARPACK users’ guide - solution of large-scale eigenvalue problems with implicitly restarted Arnoldi methods”. In: *Software, environments, tools*.
- Lesshafft, L. (2018). “Artificial eigenmodes in truncated flow domains”. In: *Theor. Comput. Fluid Dyn.* 32.3, pp. 245–262.
- Lesshafft, L. and P. Huerre (2007). “Linear impulse response in hot round jets”. In: *Phys. Fluids* 19.2, p. 024102.
- Lesshafft, L. and O. Marquet (2010). “Optimal velocity and density profiles for the onset of absolute instability in jets”. In: *J. Fluid Mech.* 662, pp. 398–408.
- Lesshafft, L., O. Semeraro, V. Jaunet, A. Cavalieri, and P. Jordan (2019). “Resolvent-based modeling of coherent wave packets in a turbulent jet”. In: *Phys. Rev. Fluids* 4.6, p. 063901.
- Lieuwen, T. (2003). “Modeling premixed combustion-acoustic wave interactions: A review”. In: *J. Propuls. Power* 19.5, pp. 765–781.
- (2021). *Unsteady combustor physics*. Cambridge University Press.
- Logg, A. and G. Wells (2010). “DOLFIN: Automated Finite Element Computing”. In: *ACM Trans. Math. Software* 37.
- Lourier, J.-M., M. Stöhr, B. Noll, S. Werner, and A. Fiolitakis (2017). “Scale Adaptive Simulation of a thermoacoustic instability in a partially premixed lean swirl combustor”. In: *Combust. Flame* 183, pp. 343–357.
- Magri, L. (2019). “Adjoint methods as design tools in thermoacoustics”. In: *Appl. Mech. Rev.* 71.2.
- Manoharan, K. and S. Hemchandra (2015). “Absolute/convective instability transition in a backward facing step combustor: Fundamental mechanism and influence of density gradient”. In: *J. Eng. Gas Turb. Power* 137.2.
- Mantić-Lugo, V., C. Arratia, and F. Gallaire (2014). “Self-consistent mean flow description of the nonlinear saturation of the vortex shedding in the cylinder wake”. In: *Phys. Rev. Lett.* 113.8, p. 084501.
- Marant, M. and C. Cossu (2018). “Influence of optimally amplified streamwise streaks on the Kelvin-Helmholtz instability”. In: *J. Fluid Mech.* 838, pp. 478–500.
- Marquet, O. and L. Lesshafft (2015). “Identifying the active flow regions that drive linear and nonlinear instabilities”. arXiv:1508.07620.
- Marquet, O., D. Sipp, and L. Jacquin (2008). “Sensitivity analysis and passive control of cylinder flow”. In: *J. Fluid Mech.* 615, pp. 221–252.
- Matalon, M. (2007). “Intrinsic flame instabilities in premixed and nonpremixed combustion”. In: *Annu. Rev. Fluid Mech.* 39, pp. 163–191.
- McKeon, B. J. and A. S. Sharma (2010). “A critical-layer framework for turbulent pipe flow”. In: *J. Fluid Mech.* 658, pp. 336–382.
- McMurtry, P., W. Jou, J. Riley, and R. Metcalfe (1986). “Direct numerical simulations of a reacting mixing layer with chemical heat release”. In: *AIAA J.* 24.6, pp. 962–970.

- Mehta, P. and M. Soteriou (2003). “Combustion heat release effects on the dynamics of bluff body stabilized premixed reacting flows”. In: *41st Aerospace Sciences Meeting and Exhibit 2003*.
- Meindl, M., C. Silva, and W. Polifke (2021). “On the spurious entropy generation encountered in hybrid linear thermoacoustic models”. In: *Combust. Flame* 223, pp. 525–540.
- Mejia, D. (2014). “Effets de la température de paroi sur la réponse de la flamme à des oscillations acoustiques”. PhD thesis. Institut National Polytechnique de Toulouse.
- Mejia, D., M. Miguel-Brebion, A. Ghani, T. Kaiser, F. Duchaine, L. Selle, and T. Poinso (2018). “Influence of flame-holder temperature on the acoustic flame transfer functions of a laminar flame”. In: *Combust. Flame* 188, pp. 5–12.
- Mejia, D., L. Selle, R. Bazile, and T. Poinso (2015). “Wall-temperature effects on flame response to acoustic oscillations”. In: *Proc. Combust. Inst.* 35, pp. 3201–3208.
- Merk, M., W. Polifke, R. Gaudron, M. Gatti, C. Mirat, and T. Schuller (2018). “Measurement and simulation of combustion noise and dynamics of a confined swirl flame”. In: *AIAA J.* 56.5, pp. 1930–1942.
- Michaels, D., S. Shanbhogue, and A. Ghoniem (2017). “The impact of reactants composition and temperature on the flow structure in a wake stabilized laminar lean premixed CH₄/H₂/air flames; mechanism and scaling”. In: *Combust. Flame* 176, pp. 151–161.
- Michalke, A. (1971). “Instabilität eines kompressiblen runden Freistrahls unter Berücksichtigung des Einflusses der Strahlgrenzschichtdicke”. In: *Z. Flugwiss* 19, p. 319.
- Miguel-Brebion, M., D. Mejia, P. Xavier, F. Duchaine, B. Bédard, L. Selle, and T. Poinso (2016). “Joint experimental and numerical study of the influence of flame holder temperature on the stabilization of a laminar methane flame on a cylinder”. In: *Combust. Flame* 172, pp. 153–161.
- Miller, C. H., W. Tang, M. A. Finney, S. S. McAllister, J. M. Forthofer, and M. J. Gollner (2017). “An investigation of coherent structures in laminar boundary layer flames”. In: *Combust. Flame* 181, pp. 123–135.
- Miller, C. H., W. Tang, E. Sluder, M. A. Finney, S. S. McAllister, J. M. Forthofer, and M. J. Gollner (2018). “Boundary layer instabilities in mixed convection and diffusion flames with an unheated starting length”. In: *Int. J. Heat Mass Transf.* 118, pp. 1243–1256.
- Monokrousos, A., E. Åkervik, L. Brandt, and D. S. Henningson (2010). “Global three-dimensional optimal disturbances in the Blasius boundary-layer flow using time-steppers”. In: *J. Fluid Mech.* 650, pp. 181–214.
- Moreno-Boza, D., W. Coenen, A. Sevilla, J. Carpio, A. L. Sánchez, and A. Liñán (2016). “Diffusion-flame flickering as a hydrodynamic global mode”. In: *J. Fluid Mech.* 798, pp. 997–1014.
- Morra, P., O. Semeraro, D. S. Henningson, and C. Cossu (2019). “On the relevance of Reynolds stresses in resolvent analyses of turbulent wall-bounded flows”. In: *J. Fluid Mech.* 867, pp. 969–984.
- Müller, J., F. Lückoff, T. Kaiser, C. Paschereit, and K. Oberleithner (2022). “Modal Decomposition and Linear Modeling of Swirl Fluctuations in the Mixing Section of a Model Combustor Based on Particle Image Velocimetry Data”. In: *J. Eng. Gas Turb. Power* 144.1.
- Murugesan, M., B. Singaravelu, A. K. Kushwaha, and S. Mariappan (2018). “Onset of flame-intrinsic thermoacoustic instabilities in partially premixed turbulent combustors”. In: *Int. J. Spray Combust. Dyn.* 10.3, pp. 171–184.
- Nair, S. and T. Lieuwen (2007). “Near-blowoff dynamics of a bluff-body stabilized flame”. In: *J. Eng. Gas Turb. Power* 23.2, pp. 421–427.

- Nastro, G., J. Fontane, and L. Joly (2020). “Optimal perturbations in viscous round jets subject to Kelvin–Helmholtz instability”. In: *J. Fluid Mech.* 900, pp. 1–25.
- Negi, P. S., A. Hanifi, and D. S. Henningson (2020). “On the linear global stability analysis of rigid-body motion fluid–structure-interaction problems”. In: *J. Fluid Mech.* 903.
- Nichols, J. and P. Schmid (2008). “The effect of a lifted flame on the stability of round fuel jets”. In: *J. Fluid Mech.* 609, pp. 275–284.
- Noack, B. R. and H. Eckelmann (1994). “A global stability analysis of the steady and periodic cylinder wake”. In: *J. Fluid Mech.* 270, pp. 297–330.
- Nogueira, P. A. S., A. Cavalieri, P. Jordan, and V. Jaunet (2019). “Large-scale streaky structures in turbulent jets”. In: *J. Fluid Mech.* 873, pp. 211–237.
- Noiray, N., D. Durox, T. Schuller, and S. Candel (2008). “A unified framework for nonlinear combustion instability analysis based on the flame describing function”. In: *J. Fluid Mech.* 615, pp. 139–167.
- Oberleithner, K., S. Schimek, and C. Paschereit (2015a). “Shear flow instabilities in swirl-stabilized combustors and their impact on the amplitude dependent flame response: A linear stability analysis”. In: *Combust. Flame* 162.1, pp. 86–99.
- Oberleithner, K., M. Stöhr, S. Im, C. Arndt, and A. Steinberg (2015b). “Formation and flame-induced suppression of the precessing vortex core in a swirl combustor: experiments and linear stability analysis”. In: *Combust. Flame* 162.8, pp. 3100–3114.
- Orchini, A., C. Silva, G. A. Mensah, and J. P. Moeck (2020). “Thermoacoustic modes of intrinsic and acoustic origin and their interplay with exceptional points”. In: *Combust. Flame* 211, pp. 83–95.
- Paladini, E., O. Marquet, D. Sipp, J.-C. Robinet, and J. Dandois (2019). “Various approaches to determine active regions in an unstable global mode: application to transonic buffet”. In: *J. Fluid Mech.* 881, pp. 617–647.
- Park, J., Y. Hwang, and C. Cossu (2011). “On the stability of large-scale streaks in turbulent Couette and Poiseuille flows”. In: *C. R. Mécanique* 339.1, pp. 1–5.
- Paschereit, C., B. Schuermans, W. Polifke, and O. Mattson (2002). “Measurement of transfer matrices and source terms of premixed flames”. In: *J. Eng. Gas Turbines Power* 124.2, pp. 239–247.
- Pfister, J.-L. and O. Marquet (2020). “Fluid–structure stability analyses and nonlinear dynamics of flexible splitter plates interacting with a circular cylinder flow”. In: *J. Fluid Mech.* 896.
- Pfister, J.-L., N. Fabbiane, and O. Marquet (2021). “Resolvent analysis of boundary-layer flows interacting with finite-extent visco-elastic insert”. In: *ICTAM 2021*. Milan (Virtuel), France.
- Picard, C. and J. Delville (2000). “Pressure velocity coupling in a subsonic round jet”. In: *Int. J. Heat Fluid Flow* 21.3, pp. 359–364.
- Pickering, E., G. Rigas, P. A. S. Nogueira, A. Cavalieri, O. T. Schmidt, and T. Colonius (2020). “Lift-up, Kelvin–Helmholtz and Orr mechanisms in turbulent jets.” In: *J. Fluid Mech.* 896, A2.
- Pier, B. (2002). “On the frequency selection of finite-amplitude vortex shedding in the cylinder wake”. In: *J. Fluid Mech.* 458, pp. 407–417.
- Poinsot, T. and S. Lelef (1992). “Boundary conditions for direct simulations of compressible viscous flows”. In: *J. Comput. Physics* 101.1, pp. 104–129.
- Poinsot, T. (2017). “Prediction and control of combustion instabilities in real engines”. In: *Proc. Combust. Inst.* 36.1, pp. 1–28.
- Poinsot, T. and D. Veynante (2005). *Theoretical and numerical combustion*. RT Edwards, Inc.

- Polifke, W., A. Poncet, C. Paschereit, and K. Döbbeling (2001a). “Reconstruction of acoustic transfer matrices by instationary computational fluid dynamics”. In: *J. Sound Vib.* 245.3, pp. 483–510.
- Polifke, W. (2014). “Black-box system identification for reduced order model construction”. In: *Ann. Nucl. Energy* 67, pp. 109–128.
- Polifke, W., C. Paschereit, and K. Döbbeling (2001b). “Constructive and destructive interference of acoustic and entropy waves in a premixed combustor with a choked exit”. In: *Int. J. Acoust. Vib* 6.3, pp. 135–146.
- Pujals, G., M. Garcia-Villalba, C. Cossu, and S. Depardon (2009). “A note on optimal transient growth in turbulent channel flows”. In: *Phys. Fluids* 21.1, p. 015109.
- Qadri, U., G. J. Chandler, and M. Juniper (2015). “Self-sustained hydrodynamic oscillations in lifted jet diffusion flames: origin and control”. In: *J. Fluid Mech.* 775, pp. 201–222.
- Qadri, U., L. Magri, M. Ihme, and P. Schmid (2021). “Using adjoint-based optimization to enhance ignition in non-premixed jets”. In: *Proc. Roy. Soc. A* 477.2245, p. 20200472.
- Qadri, U. and P. Schmid (2017). “Frequency selection mechanisms in the flow of a laminar boundary layer over a shallow cavity”. In: *Phys. Rev. Fluids* 2.1, p. 013902.
- Ren, X., X. Ju, and M. J. Gollner (2022). “Effect of freestream turbulence on the structure of boundary-layer flames”. In: *Combust. Flame* 236, p. 111750.
- Rigas, G., D. Sipp, and T. Colonius (2021). “Nonlinear input/output analysis: application to boundary layer transition”. In: *J. Fluid Mech.* 911.
- Sánchez, A. L. and F. A. Williams (2014). “Recent advances in understanding of flammability characteristics of hydrogen”. In: *Prog. Energy Combust. Sci* 41, pp. 1–55.
- Sato, J. (1982). “Effects of lewis number on extinction behavior of premixed flames in a stagnation flow”. In: *Symposium (International) on Combustion* 19.1. Nineteenth Symposium (International) on Combustion, pp. 1541–1548.
- Sattelmayer, T. (2003). “Influence of the combustor aerodynamics on combustion instabilities from equivalence ratio fluctuations”. In: *J. Eng. Gas Turbines Power* 125.1, pp. 11–19.
- Sayadi, T. and P. Schmid (2021). “Frequency response analysis of a (non-)reactive jet in crossflow”. In: *J. Fluid Mech.* 922, A15.
- Schmid, P. and D. Henningson (2001). *Stability and transition in shear flows*. Springer.
- Schmidt, O., A. Towne, G. Rigas, T. Colonius, and G. Brès (2018). “Spectral analysis of jet turbulence”. In: *J. Fluid Mech.* 855, pp. 953–982.
- Schonfeld, T. and M. Rudgyard (1999). “Steady and unsteady flow simulations using the hybrid flow solver AVBP”. In: *AIAA J.* 37.11, pp. 1378–1385.
- Schuller, T. (2003). “Mécanismes de couplage dans les interactions acoustiques-combustion”. PhD thesis. Ecole Centrale Paris.
- Schuller, T., D. Durox, and S. Candel (2003a). “A unified model for the prediction of laminar flame transfer functions: comparisons between conical and V-flame dynamics”. In: *Combust. Flame* 134.1-2, pp. 21–34.
- (2003b). “Self-induced combustion oscillations of laminar premixed flames stabilized on annular burners”. In: *Combust. Flame* 135.4, pp. 525–537.
- Semeraro, O., L. Lesshafft, V. Jaunet, and P. Jordan (2016). “Modeling of coherent structures in a turbulent jet as global linear instability wavepackets: Theory and experiment”. In: *Int. J. Heat Fluid Flow* 62, pp. 24–32.
- Shanbhogue, S., S. Husain, and T. Lieuwen (2009a). “Lean blowoff of bluff body stabilized flames: Scaling and dynamics”. In: *Prog. Energy Combust. Sci.* 35.1, pp. 98–120.

- Shanbhogue, S., D. Shin, S. Hemchandra, D. Plaks, and T. Lieuwen (2009b). “Flame-sheet dynamics of bluff-body stabilized flames during longitudinal acoustic forcing”. In: *Proc. Combust. Inst.* 32.2, pp. 1787–1794.
- Shin, D. and T. Lieuwen (2013). “Flame wrinkle destruction processes in harmonically forced, turbulent premixed flames”. In: *J. Fluid Mech.* 721, pp. 484–513.
- Shin, D., D. Plaks, T. Lieuwen, U. Mondragon, C. Brown, and V. McDonell (2011). “Dynamics of a longitudinally forced, bluff body stabilized flame”. In: *J. Propuls. Power* 27.1, pp. 105–116.
- Silva, C. F., M. Merk, T. Komarek, and W. Polifke (2017). “The contribution of intrinsic thermoacoustic feedback to combustion noise and resonances of a confined turbulent premixed flame”. In: *Combust. Flame* 182, pp. 269–278.
- Sipp, D., O. Marquet, P. Meliga, and A. Barbagallo (2010). “Dynamics and control of global instabilities in open-flows: a linearized approach”. In: *Appl. Mech. Rev.* 63.3.
- Skene, C. and P. Schmid (2019). “Adjoint-based parametric sensitivity analysis for swirling M-flames”. In: *J. Fluid Mech.* 859, pp. 516–542.
- Sogaro, F., P. Schmid, and A. Morgans (2019). “Thermoacoustic interplay between intrinsic thermoacoustic and acoustic modes: non-normality and high sensitivities”. In: *J. Fluid Mech.* 878, pp. 190–220.
- Steinbacher, T., A. Albayrak, A. Ghani, and W. Polifke (2019). “Consequences of flame geometry for the acoustic response of premixed flames”. In: *Combust. Flame* 199, pp. 411–428.
- Steinbacher, T., M. Meindl, and W. Polifke (2018). “Modelling the generation of temperature inhomogeneities by a premixed flame”. In: *Int. J. Spray Combust. Dyn.* 10.2, pp. 111–130.
- Stöhr, M., K. Oberleithner, M. Sieber, Z. Yin, and W. Meier (2018). “Experimental study of transient mechanisms of bistable flame shape transitions in a swirl combustor”. In: *J. Eng. Gas Turb. Power* 140.1.
- Suresha, S., R. Sujith, B. Emerson, and T. Lieuwen (2016). “Nonlinear dynamics and intermittency in a turbulent reacting wake with density ratio as bifurcation parameter”. In: *Phys. Rev. E* 94.4, p. 042206.
- Suzuki, H., Y. Inoue, T. Nishimura, K. Fukutani, and K. Suzuki (1993). “Unsteady flow in a channel obstructed by a square rod (crisscross motion of vortex)”. In: *Int. J. Heat Fluid Flow* 14.1, pp. 2–9.
- Taira, K., M. Hemati, S. Brunton, Y. Sun, K. Duraisamy, S. Bagheri, S. Dawson, and C. Yeh (2020). “Modal analysis of fluid flows: Applications and outlook”. In: *AIAA J.* 58.3, pp. 998–1022.
- Tammisola, O., F. Giannetti, V. Citro, and M. P. Juniper (2014). “Second-order perturbation of global modes and implications for spanwise wavy actuation”. In: *J. Fluid Mech.* 755, pp. 314–335.
- Tammisola, O. and M. P. Juniper (2016). “Coherent structures in a swirl injector at $Re=4800$ by nonlinear simulations and linear global modes”. In: *J. Fluid Mech.* 792, pp. 620–657.
- Theofilis, V. (2003). “Advances in global linear instability analysis of nonparallel and three-dimensional flows”. In: *Prog. Aerosp. Sci.* 39.4, pp. 249–315.
- Towne, A., O. Schmidt, and T. Colonius (2018). “Spectral proper orthogonal decomposition and its relationship to dynamic mode decomposition and resolvent analysis”. In: *J. Fluid Mech.* 847, pp. 821–867.
- Turki, S., H. Abbassi, and S. Nasrallah (2003). “Two-dimensional laminar fluid flow and heat transfer in a channel with a built-in heated square cylinder”. In: *Int. J. Therm. Sci.* 42.12, pp. 1105–1113.

- Turton, S., L. Tuckerman, and D. Barkley (2015). “Prediction of frequencies in thermosolutal convection from mean flows”. In: *Phys. Rev. E* 91.4, p. 043009.
- Van Oijen, J., A. Donini, R. Bastiaans, J. ten Thijsse Boonkamp, and L. De Goey (2016). “State-of-the-art in premixed combustion modeling using flamelet generated manifolds”. In: *Prog. Energy Combust. Sci.* 57, pp. 30–74.
- Vance, F., Y. Shoshin, L. de Goey, and J. van Oijen (2021). “An investigation into flashback and blow-off for premixed flames stabilized without a recirculation vortex”. In: *Combust. Flame* 235, p. 111690.
- Waleffe, F. (1997). “On a self-sustaining process in shear flows”. In: *Phys. Fluids* 9.4, pp. 883–900.
- Wang, C., T. Kaiser, M. Meindl, K. Oberleithner, W. Polifke, and L. Lesshafft (2022a). “Linear instability of a premixed slot flame: Flame transfer function and resolvent analysis”. In: *Combust. Flame* 240, p. 112016.
- Wang, C., L. Lesshafft, A. V. Cavalieri, and P. Jordan (2021). “The effect of streaks on the instability of jets”. In: *J. Fluid Mech.* 910.
- Wang, C., L. Lesshafft, and K. Oberleithner (2022b). “Global linear stability analysis of a flame anchored to a cylinder”. In: *arXiv preprint arXiv:2203.02305*.
- Wang, H., C. K. Law, and T. Lieuwen (2009). “Linear response of stretch-affected premixed flames to flow oscillations”. In: *Combust. Flame* 156.4, pp. 889–895.
- Williams, G. C., H. C. Hottel, and A. C. Scurlock (1948). “Flame stabilization and propagation in high velocity gas streams”. In: *Symp. Combust. Flame Explos. Phenom.* 3.1, pp. 21–40.
- Xu, L., J. Zheng, G. Wang, Z. Feng, X. Tian, L. Li, and F. Qi (2021). “Investigation on the intrinsic thermoacoustic instability of a lean-premixed swirl combustor with an acoustic liner”. In: *Proc. Combust. Inst.* 38.4, pp. 6095–6103.
- Yang, D., J. Guzmán-Iñigo, and A. S. Morgans (2020). “Sound generation by entropy perturbations passing through a sudden flow expansion”. In: *J. Fluid Mech.* 905, R2.
- Zhao, D., Z. Lu, H. Zhao, X. Li, B. Wang, and P. Liu (2018). “A review of active control approaches in stabilizing combustion systems in aerospace industry”. In: *Prog. Aerosp. Sci.* 97, pp. 35–60.

Titre : Analyse globale des instabilités linéaires de flammes

Mots clés : instabilité d'écoulement, instabilité de flamme, instabilité linéaire

Résumé : Cette thèse vise à appliquer les développements récents de la méthodologie du domaine de la théorie de l'instabilité linéaire à l'étude de l'instabilité de combustion. L'instabilité de la flamme se réfère ici aux oscillations instables du champ d'écoulement réactif. L'analyse des modes propres pour la description des oscillations auto-entretenues et l'analyse entrée-sortie pour la caractérisation du comportement des amplificateurs sont mises en œuvre dans un cadre global. Les équations décrivant l'écoulement réactif sont linéarisées et résolues dans l'ensemble du domaine de calcul, y compris les schémas de réaction chimique linéarisés. Dans ce cadre, l'interaction entre la dynamique de l'écoulement, la réaction chimique et l'acoustique peut être intrinsèquement prise en compte et étudiée en détail. Dans cette thèse, nous nous concentrons sur la dynamique linéaire des flammes laminaires prémélangées, comprenant principalement une flamme à fente qui agit comme un amplificateur, et une flamme stabilisée à corps bluff qui agit comme

un oscillateur. La réponse au forçage de la flamme à fente avec un schéma de réaction en deux étapes pour la combustion du méthane est étudiée. La fonction de transfert de flamme est calculée à partir du modèle linéaire, en excellent accord avec les calculs non linéaires de référence. L'analyse résolvante est utilisée pour identifier les structures de forçage optimales et leur réponse de flamme associée, conduisant à une discussion des mécanismes dominants pour l'amplification des perturbations d'écoulement, qui déclenchent des oscillations de flamme. La stabilité linéaire globale d'une flamme prémélangée laminaire ancrée sur un corps bluff est étudiée. Les résultats montrent quantitativement que la dynamique globale de la flamme est ici contrôlée par l'instabilité hydrodynamique dans le cisaillement de sillage. L'analyse du champ temporellement moyenné d'une flamme oscillante dans le cycle limite capture avec précision la fréquence de chute. Un projet parallèle de cette thèse étudie l'effet des stries sur l'instabilité des jets non réactifs.

Title : Global linear analysis of flame instability

Keywords : flow instability, flame instability, linear instability

Abstract : The thesis aims to apply recent developments of methodology from the field of linear instability theory to the study of combustion instability. The flame instability here refers to the unsteady oscillations in the reacting flow field. The eigenmode analysis for the description of self-sustained oscillations, and input-output analysis for the characterization of amplifier behaviour is implemented in a global framework. The governing equations of reacting flow are linearized and resolved in the entire computational domain, including the linearized chemical reaction schemes. In this framework, the interplay between flow dynamics, chemical reaction and acoustics can be inherently accounted for and investigated in full detail. In this thesis, we concentrate on the linear dynamics of premixed laminar flames, mainly including a slot flame that acts an amplifier, and a bluff-body stabilised flame that acts as oscillator. The response

to forcing of the slot flame with a two-step reaction scheme for methane combustion is investigated. The flame transfer function is computed from the linear model, in excellent agreement with reference nonlinear calculations. The resolvent analysis is used to identify optimal forcing structures and their associated flame response, leading to a discussion of the dominant mechanisms for the amplification of flow perturbations, which trigger flame oscillations. Global linear stability of a laminar premixed flame anchored on a bluff body is investigated. The results quantitatively show that the global flame dynamics here is controlled by hydrodynamic instability in the wake shear. Mean flow analysis of an oscillating flame in the limit cycle accurately captures the shedding frequency. A side project of this thesis studies the effect of streaks on the instability of non-reacting jets.